ABSTRACT

Title of dissertation: SPECTRAL X-RAY SCATTERING METHOD FOR IN VIVO ESTIMATION OF AMYLOID BURDEN

Eshan Dahal, Doctor of Philosophy, 2020

Dissertation directed by: Dr. Aldo Badano
U.S. Food and Drug Administration
Center for Devices and Radiological Health
Office of Science and Engineering Laboratories
Division of Imaging, Diagnostics, and Software Reliability

Amyloid-β plaque deposition in the brain is one of the hallmark features of Alzheimer's disease (AD). Current estimation methods of amyloid burden depend on post-mortem histological analysis or resource-intensive contrast-enhanced imaging techniques. This dissertation focuses on developing a label-free, fast and non-invasive method based on spectral small-angle x-ray scattering (sSAXS) to estimate brain amyloid burden *in vivo* in small animals. Small-angle x-ray scattering (SAXS) is a well-established technique for identifying molecular structures based on their scattering features. However, SAXS is limited to the study of thin biological samples in the mm scale relying on low-energy monochromatic x rays. I built a prototype sSAXS system to tackle the sample thickness limit of traditional SAXS and explore *in vivo* applications with higher x-ray energies. This was achieved by integrating a polychromatic x-ray source with a 2D spectroscopic detector for simultaneously and efficiently collecting SAXS data in angle- and energy dispersive modes. A method

based on sSAXS was introduced, and its capability was first demonstrated by identifying embedded targets in up to 5-cm-thick phantoms with an x-ray energy range between 30 and 45 keV. Wild-type and 5XFAD mice (AD animal model) were used to demonstrate the ability of the method to estimate amyloid burden in specific areas of the brain without using contrast agents. The mouse head was irradiated at selected locations using a two-pinhole collimated beam of polychromatic x rays for 300 s. The findings correlated well with the histological (gold standard) results. This work presents a promising new method based on sSAXS to estimate amyloid burden in the brain of small animals and possibly in humans.

SPECTRAL X-RAY SCATTERING METHOD FOR IN VIVO ESTIMATION OF AMYLOID BURDEN

by

Eshan Dahal

Dissertation submitted to the Faculty of the Graduate School of the
University of Maryland, College Park in partial fulfillment
of the requirements for the degree of
Doctor of Philosophy
2020

Advisory Committee:
Professor Yu Chen, Chair/Academic Advisor
Dr. Aldo Badano, Co-chair/Research Advisor
Professor J. Carson Smith, Dean's Representative
Professor Giuliano Scarcelli
Professor Ian White

© Copyright by
Eshan Dahal
2020

Dedication

To my family and mentors

Acknowledgments

I would like to express my deepest gratitude and appreciation to Dr. Aldo Badano for his mentorship and unwavering support. I am very fortunate to be his PhD student and work in an extraordinary research environment in DIDSR at FDA. By working with him closely, I have learned a great deal about both research and leadership and feel well-prepared for success beyond PhD. He has instilled in me a growth mindset to continuously learn new skills and tackle challenges above my comfort zone. I cannot thank him enough for patiently guiding me to complete my dissertation work and for providing countless opportunities and advice to make me a more discerning scientist.

I gratefully acknowledge Prof. Yu Chen for his timely academic advising and making sure of my steady PhD progress. He was also instrumental in facilitating me to perform my doctoral work at FDA. Thank you for your invaluable support and advice. I am also extremely grateful to have Dr. Bahaa Ghammraoui (FDA) as a mentor with sharp x-ray physics and experiment skills. Thank you for your guidance and help with x-ray experiments and instrumentation, MC-GPU simulation, and detector data analysis. I would like to thank Randolph Bidinger and his team (FDA) for making phantoms, pinhole collimators, and detector stages. I acknowledge and appreciate their effort to deliver custom parts necessary for the experimental work. I would also like to extend my sincere thanks to...

...Prof. J. Carson Smith for guidance and expertise on AD and small animal study, and help to get AD mice samples.

...Profs. Giuliano Scarcelli, Ian White, and J. Carson Smith for serving on my dissertation committee and for their overall comments and suggestions.

...Dr. Stephanie Bissel and Dr. Bruce Lamb (Indiana University School of Medicine) for providing 5XFAD and WT mice heads and details of the animal procedures and protocols.

...Dr. Meijun Ye (FDA) for her expertise and assistance in histological analysis.

...Dr. Elissa Wong (FDA) for providing adult WT mice head samples.

...Dr. Andreu Badal (FDA) for advice on simulation and phantom work.

...Dr. Mina Choi (Former PhD graduate) for introducing me to SAXS and AD research.

...Sophya Breedlove and Jason Crentsil (Summer REU) for collecting sSAXS data.

...Dr. Wei-Chung Cheng (FDA) for providing resources on optical microscopy.

...Sarah Dudgeon (FDA) for being a good friend and for our daily conversations on graduate life and research.

...everyone in the DIDSR family for their continuous support, care, and encouragement.

Finally, I would like to thank my parents and wife for their unconditional support and encouragement to pursue and complete my PhD. I acknowledge the funding by appointments to the Research Participation Program at the Center for Devices and Radiological Health administered by the Oak Ridge Institute for Science and Education through an interagency agreement between the US Department of Energy and the US Food and Drug Administration (FDA).

Table of Contents

List of Figures vii

List of Abbreviations xiii

1 Background and motivation 1
1.1 Alzheimer's disease . . . 1
1.2 Amyloid plaques in Alzheimer's disease . . . 4
1.2.1 Brain amyloid burden estimation methods . . . 7
1.3 Small-angle x-ray scattering . . . 12
1.3.1 Theory . . . 14
1.3.2 Instrumentation . . . 16
1.4 Spectral SAXS . . . 19
1.5 Thesis scope . . . 24

2 Development and validation of an sSAXS prototype 26
2.1 Introduction . . . 27
2.2 Methods . . . 29
2.2.1 A prototype sSAXS system . . . 29
2.2.2 sSAXS data analysis . . . 32
2.3 Results and discussions . . . 33
2.4 Conclusion . . . 42

3 Amyloid models 45
3.1 Introduction . . . 45
3.2 Methods . . . 47
3.2.1 Amyloid model preparation . . . 47
3.2.2 Congo red absorbance assay . . . 48
3.2.3 SAXS data collection and processing . . . 48
3.2.4 sSAXS measurements . . . 50
3.3 Results and discussions . . . 51
3.3.1 Congo red absorbance assay . . . 52
3.3.2 SAXS characterization . . . 53
3.3.3 Preliminary sSAXS characterization of amyloids in phantoms . 63
3.4 Conclusion . . . 67

4 Characterization of amyloid-like targets in a mouse head with skull 69
4.1 Introduction . . . 70
4.2 Methods . . . 72
4.3 Results and discussions . . . 76
4.4 Conclusion . . . 85

5 Label-free estimation of brain amyloid burden in AD mouse model 88
5.1 Introduction . . . 88
5.2 Methods . . . 90
5.2.1 Animals . . . 91
5.2.2 Experimental prototype . . . 91
5.2.3 Data analysis . . . 93
5.2.4 Histology. . . . 94
5.3 Results and discussions . . . 95
5.4 Conclusion . . . 101

6 Future Directions 102
6.1 Developing a small-animal scanner . . . 105
6.2 Applications in humans . . . 109
6.3 Other applications . . . 111

Bibliography 113

List of Figures

1.1 Lifetime risk for developing dementia due to AD by age and gender using the competing mortality–adjusted cumulative incidence estimates from the Framingham Heart Study (1975–2009) reported by Chêne et al. [1]. 2

1.2 Changing biomarkers with AD progression [2]. Reprinted from Jack et al. Lancet Neurol 2010; 9:119-128, with permission from Elsevier. . 5

1.3 Schematic representation of the 2D x-ray diffraction pattern (a) typical from cross-β structures of amyloid fibrils (b). 0.47 nm is the repeating distance between adjacent β-strands and 1.0 nm is between β-sheets. 7

1.4 Schematic of the scattering process to define scattering or momentum transfer vector $\vec{q}$. 15

1.5 Schematic of a typical SAXS setup to obtain structure sensitive data. Distinct scattering curves from cylindrical and spherical structures are shown as an example. 17

2.1 Schematic of a prototype sSAXS system to collect SAXS data from thick samples simultaneously in angle- and energy-dispersive modes. P1 and P2 are two lead pinhole collimators of 2.5 and 0.5 mm diameters respectively. 30

2.2 Picture of the laboratory prototype sSAXS system. 31

2.3 sSAXS data analysis workflow using caffeine sample as an example in 30–45 keV energy range. (a) Raw 2D detector data showing counts in each pixel per energy bin (left). Corresponding 1D data in terms of q without transmission correction (right). (b) Transmission corrected counts as a function of q per energy bin. (c) Summed q-data (Δq = 1.2 nm^{-1}) from 30 to 45 keV to get the scattering cross-section information, $S(q)$. (d) Background corrected counts per transmitted photon in each pixel (top) and the corresponding S(q) of caffeine with two Bragg peaks (bottom). 34

2.4 Validation of the transmission measurements. (a) Transmitted photons from the PMMA slabs of 1, 3, and 5 cm thickness. (b) Comparison of the transmission factor with the reference values from NIST using the mass attenuation coefficient values of PMMA [3]. 36

2.5 (a) Illustration of the caffeine target identification study in the objects made from PMMA slabs, where F1, M1, and B1 denote the target location. The arrow shows the x-ray beam direction. (b-c) $S(q)$ of the caffeine targets recovered from the 1 cm PMMA and their corresponding area-under-the-peak (AUP) values from 7.24 to 9.64 nm^{-1}. The caffeine target only study without any PMMA slabs was used as a reference. (d-e) $S(q)$ of the caffeine targets recovered from the 3 cm PMMA and their corresponding AUPs. Error bars represent standard deviations from two measurements at each target location. . 38

2.6 (a) Illustration of the study to investigate the effect of object thickness, where the caffeine target is fixed at F1 and the thickness of object made from PMMA slabs are varied from 1 to 5 cm. (b) $S(q)$ of the PMMA slabs with and without a caffeine target at F1. (c) Recovered $S(q)$ of the caffeine target after subtracting the scattering signal contributed by the PMMA slabs. (d) Corresponding AUP values from the recovered signal of the caffeine target in the 1, 3, and 5 cm PMMA slabs in comparison to the target alone study in a syringe. Error bars represent standard deviations from two measurements. . . 41

2.7 (a) Observation of the shifts in the scattering peaks of PMMA when the used SDD distance does not account for the actual location of the PMMA slab. The 1 cm PMMA slab is moved 5 cm in total distance, but the SDD for analyzing the moving PMMA is always 189 mm. (b) Correlating the shifted peak position of PMMA with the SDD. 42

3.1 Schematic of A) a method to prepare an amyloid fibril model with heating from BSA B) SAXS set-up for measurements with illustration of distinct scattering curves, $I(q)$, for rod-like and spherical structures that would be theoretically acquired. Indirect Fourier transformation (IFT) of $I(q)$ would result in structure sensitive pair-distance distribution function, $P(r)$, in real space. 51

3.2 UV-Vis spectra of 5 μM Congo red (CR): A) with freshly prepared BSA monomers and 30-min old BSA fibrils and B) with 30-min and 2-month old BSA fibrils. The spectra of CR and BSA fibrils alone are shown for reference. 53

3.3 SAXS characterization of BSA fibrils for time periods of 30 min to 2 months using the IFT method. (A) SAXS signals, $I(q)$ in absolute scale, with IFT fits of experimental data (open circles). (B) Pair-distance distribution function, $P(r)$, resulting from IFT fits. The offset in $P(r)$ for various times is for visual clarity. 54

3.4 SAXS characterization of the mixture solutions of fibrils and monomers along with the volume fraction estimates. (A) Representative $I(q)$ curves in absolute scale for the solution with 0, 0.3, 0.5, 0.7, and 1.0 volume fractions of fibrils. (B) Corresponding $P(r)$ curves generated from the IFT fits of the experimental data. (C) SAXS estimate of the volume fraction of fibrils relative to the true value. Small error bar represents the standard deviation in the SAXS estimates from the three independent experiments. (D) Low-resolution bead models of BSA fibrils generated by using the ab initio shape determination program [4]. Two different views are shown. 57
3.5 SAXS measurements of amyloid plaque model made from BSA fibrils showing A) 2D scattering pattern typical of AD associated $A\beta$ fibrils and plaque structures [5, 6], B) Radially averaged 1D scattering pattern in inverse space with distinct peaks at 6.4 nm^{-1} and 13.4 nm^{-1} from β-sheet structure, where error bar represents a standard deviation in data from two independently prepared samples, C) 1D scattering pattern in terms of Bragg spacing with q = 2π/d, and D) schematic representation of β-sheet structure of $A\beta$ fibrils based on the SAXS data presented in C). The peak at 0.47 nm is the repeat distance between β-strands and the peak at 0.98 nm is the repeat distance between β-sheets. Each arrow represents a β-strand and the two colors represent β-sheets. Similar structural features are reported to be found in human brain tissue with AD [5]. 60
3.6 SAXS measurements of amyloid plaque model deposited on brain tissues. a) Radially averaged 1D scattering data of brain slice without plaques, with 1x plaques ($\sim$ 0.4 mg/mm^3), and with 2x plaques ($\sim$ 0.8 mg/mm^3) in absolute scale. Error bars are standard deviation in the intensity values of pixels per q bin and are shown every 10 points for clarity. b) Scattering profile of 1x and 2x plaques after subtracting 1D SAXS data of brain slice with plaques from without plaques. . . . 62
3.7 (a) Schematic of amyloid model preparation, heated (left) and unheated (right). (b) Syringe sample of an amyloid model. (c) sSAXS system setup. (d) Dimensions of the cylindrical PMMA phantom. . . 64
3.8 Characterization of the heated and unheated amyloid models in a syringe. (a) Scattering signal of the heated model using 600 and 1800 s data acquisition times. (b) Effect of BSA concentration in the scattering signal of the heated model. Error bar represents standard deviations from n=3 measurements. (c) Scattering signal of the unheated model for 600 and 1800 s from n=2 measurements. (d) Representative 2D detector data of the unheated model in 30 to 45 keV energy range 65

3.9 Characterization of the unheated amyloid model in a cylindrical PMMA phantom. (a–c) 2D detector data before and after background subtraction, (d) Scattering signal from the PMMA phantom with and without the unheated amyloid model. (e) Recovered scattering peaks associated with amyloids after background subtraction. Error bar represents standard deviations from n=3 measurements. 66

4.1 Experimental setup and data from an amyloid model in 30 to 45 keV energy range. (a) Schematic of the sSAXS experimental setup to collect scattered x rays at small angles from thick samples using a polychromatic x-ray source and a 2D spectroscopic detector. P1 and P2 are two pinhole collimators and SDD is sample to detector distance. (b) Processed detector data from an amyloid model, after attenuation and background corrections, showing counts per transmitted photon in each pixel in the energy window of 30 to 45 keV. (c) Corresponding scattering cross-section data, S(q), from an amyloid model for 600 and 1800 s measurement times. Distinct peaks around 6 and 13 nm^{-1} are characteristic of the amyloid fibrils or plaques in AD due to their β-sheet structures [5, 6]. 75

4.2 Simulation study of the scattering contribution as a function of angle by Coherent, Compton, and multiple-scatter using a spherical detector from a 4 cm cubic of water irradiated with 30 keV monoenergetic x-ray beam. 77

4.3 Validation of sSAXS setup and data analysis process using the known Bragg peaks of caffeine at 8.4 and 18.8 nm^{-1}. (a) Processed detector data from caffeine powder, after attenuation and background corrections, showing counts per transmitted photon in each pixel in the energy window of 30 to 45 keV. (b) Scattering cross-section data of the caffeine sample and syringe background with 600 s measurement time. (c) Background corrected scattering cross-section data of the caffeine sample. 78

4.4 Mass fraction study in a syringe. (a) Illustration of a syringe study, in which a syringe with an amyloid target of known mass fraction was scanned at three different positions to report $S(q)$ data as mean $\pm$ standard deviation. (b) $S(q)$ of the amyloid target with mass fraction varying from 0 to 1 in the q-range from 0 to 28 nm^{-1}. (c) $S(q)$ data focusing on the rising peak around 6 nm^{-1}. (d) Linear correlation between the mass fraction of the amyloid-like target and the area-under-the-peak (AUP) from 3.6 to 8.4 nm^{-1}. 80

4.5 Mouse head study with an intact skull. (a) Illustration of a mouse head study ex vivo. A syringe with an amyloid target is placed in the front, center or back of the fixed mouse head with respect to the x-ray beam direction. The measurement was repeated three times at each position to report $S(q)$ as mean ± standard deviation. (b) $S(q)$ of the mouse head with and without an amyloid target on front, center, and back with 600 s measurement time. (c) Recovered $S(q)$ of the front, center, and back amyloid targets after subtracting the scattering signal contributed by the mouse head. (d) Corresponding AUP values from the recovered signal of the front-, center- and back-configuration in a mouse head in comparison to the target alone in a syringe. Front = Ipsilateral, center = medial, and back = contralateral. 82

4.6 (a) Illustration of the scanning study of a wild-type mouse head *ex vivo* without an amyloid target from ear (I) to eye (IV). (b) $S(q)$ of the mouse head at various scanned locations with and without an amyloid target in center. (c) Recovered $S(q)$ of amyloid targets after subtracting the background scattering signal (w/o amyloid) collected from position I to IV. (d) Corresponding AUP values in comparison to the target alone. 86

5.1 AD and WT mouse head samples used in the sSAXS study. 92

5.2 Schematic of the experimental sSAXS setup and data processing steps. (a) The mouse head is irradiated at select locations with a collimated beam of polychromatic x rays of 1 mm diameter. A 2D spectroscopic detector (CdTe) is used to collect SAXS data simultaneously in angle- and energy-dispersive modes for each location. The sample to detector distance (SDD) was 214 mm (b) sSAXS data processing steps in 30 to 45 keV energy range are illustrated using an amyloid model from BSA with two Bragg peaks at 6.04 and 13.24 nm^{-1}. The 2D detector data (left) showing counts in each pixel per energy bin is converted to scattering cross section, $S(q)$, per energy bin (middle) after applying a transmission correction. The $S(q)$ is then summed ($\Delta q = 1.2\ nm^{-1}$) from 30 to 45 keV to combine scattering information in all energy bins and to calculate the area under the peak (AUP) from 3.6 to 8.4 nm^{-1} (right). 96

5.3 Initial AD and WT mouse head scanning results with a 0.5 mm polychromatic x-ray beam. Each mouse head was scanned between eye and ear (S1-S4, sagittal plane, $\Delta x = 2$ mm) at different heights (H1-H3,$\Delta z = 1$ mm) 97

5.4 Amyloid burden estimations in intact heads corresponding to 5XFAD mice and WT controls. (a) Approximate studied locations in the mouse brain in comparison to an anatomic reference image from the Allen Mouse Brain Atlas containing major brain regions in a sagittal plane [7]. (b) Correlation between the ΔAUP calculated from the sSAXS method and the amyloid load estimates derived from histology for three locations (Pearson $r = 0.94$, $P < 0.001$). (c) Corresponding S(q) of AD and WT mice used for ΔAUP calculation after studying their heads with an intact skull in each location for 300 s. Error bars represent ± standard deviation from three measurements for each location. (d) Representative histology images of AD and WT brain slices using Thioflavin S. The zoomed image (top) is focused on the hippocampus of AD brain slice. 99

5.5 S(q) of amyloid model (a) and caffeine (b) using 1 mm vs. 0.5 mm x-ray beam spot size. 101

6.1 Schematic of one potential design of a small-animal scanner prototype that can be commercially developed. 107

List of Abbreviations

sSAXS	Spectral small-angle x-ray scattering
SAXS	Small-angle x-ray scattering
AD	Alzheimer's disease
$A\beta$	Amyloid-β
MCI	Mild cognitive impairment
FTIR	Fourier-transform infrared spectroscopy
XRD	X-ray diffraction
PET	Positron emission tomography
MRI	Magnetic resonance imaging
SUVR	Standardized uptake value ratio
SUV	Standardized uptake value
PiB	Pittsburgh compound B
CL	Centiloid value
CCD	Charged-coupled device
EDSAXS	Energy-dispersive SAXS
CdTe	Cadmium telluride
ASIC	Application-specific integrated circuit
SDD	Sample to detector distance
PMMA	Polymethyl methacrylate
AUP	Area-under-the-peak
FDA	Food and Drug Administration
UMD	University of Maryland
BSA	Bovine serum albumin
PBS	Phosphate buffered saline
IFT	Indirect Fourier Transformation
CR	Congo red
WT	Wild-type
ROI	Regions of interest
IACUC	Institutional Animal Care and Use Committee
CT	Computed tomography
CSF	Cerebrospinal fluid
MC-GPU	Monte Carlo-Graphical Processing Unit

Chapter 1: Background and motivation

This dissertation focuses on developing a label-free method based on spectral small-angle x-ray scattering (sSAXS) to estimate brain amyloid burden *in vivo* in small animals. The accumulation of amyloid plaques in the brain and the corresponding increase in amyloid burden is associated with a wide range of neurodegenerative diseases [8, 9]. We specifically focus on Alzheimer's disease for method demonstration, where plaques are formed by aggregation of amyloid-β peptides. A prototype sSAXS system is designed and built for this purpose to probe thick samples, such as an intact mouse head, within minutes. The system records distinct SAXS signals from amyloid plaques due to its β-sheet structure, and we use that information to quantify amyloid burden.

In this chapter, we provide a general overview of the key topics covered by this thesis, along with the motivation for our work and organization of thesis chapters.

1.1 Alzheimer's disease

Alzheimer's disease (AD) is a progressive neurodegenerative disorder that causes dementia. As of 2020, there is no cure for AD or treatment options to slow down the disease progression. AD is the sixth leading cause of death in the US,

where deaths from AD rose by 146.2% between 2000 and 2018 [10]. It remains the leading cause of dementia in the elderly population, contributing 60 to 80% of all dementia cases. In the US alone, people aged 65 and above with AD are projected to increase from 5.8 million to 13.8 million in the next 30 years [10, 11]. This suggests a significant public health problem with an aging US population and longer life expectancy. The lifetime probability of developing dementia due to AD by age and gender is shown in Fig. 1.1. It shows that women are about twice likely to have

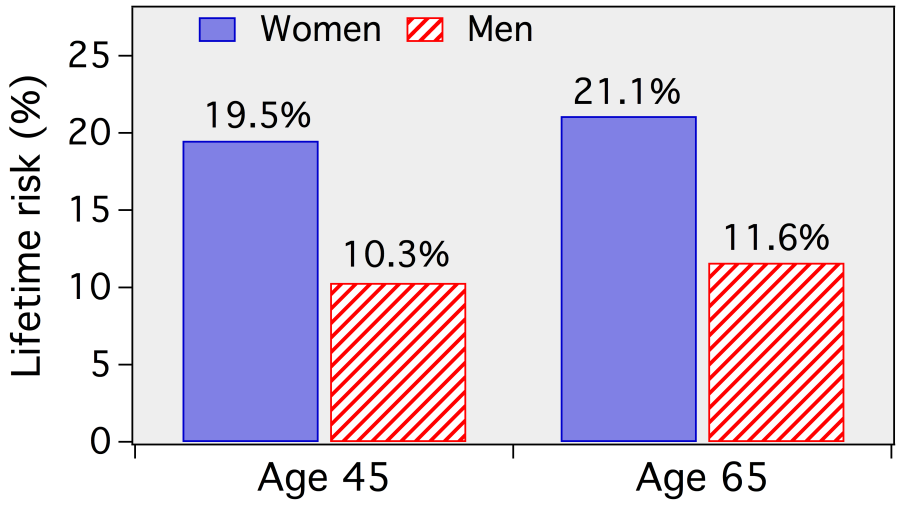


Figure 1.1: Lifetime risk for developing dementia due to AD by age and gender using the competing mortality–adjusted cumulative incidence estimates from the Framingham Heart Study (1975–2009) reported by Chêne et al. [1].

AD than men irrespective of their age (45 or 65 years old). About two-thirds of 5.8 million people with AD in the US are women [10, 11]. In general, there is 1 in 5 to 1 in 10 likelihood of AD affecting people over the age of 65. There is also a genetic risk factor involved in addition to age and gender. The APOE-ε4 gene has been strongly established to increase the risk of AD [12, 13]. Every person inherits two of the three APOE alleles (ε2, ε3, ε4), one from each parent. For those who

inherits two $\varepsilon 4$ alleles, the AD risk at old age is reported to increase by more than 10 folds [12, 14].

AD was originally described by Alois Alzheimer in 1906 based on the histopathological findings of extracellular plaques and intracellular neurofibrillary tangles in the brain [15]. Pathophysiological changes in the AD occur over 20 years or more before the first symptoms of dementia manifest [16, 17]. Detection and characterization of these changes in the longitudinal studies may be the key to develop effective therapeutics and facilitate prevention trials. Clinical diagnosis of AD is possible only at the late stage when cognitive impairment becomes apparent. The average survival time after AD diagnosis decreases with age. People diagnosed with AD in their 60s are reported to live for 7 to 10 years, whereas people in their 90s only survive for 3 years or less [18].

The progression of AD can be described in three phases [19]. First is the preclinical phase that lasts more than two decades. In this phase, individuals have normal cognition, but there are some pathological changes in the brain. An early pathological change is considered to be the accumulation of amyloid-β ($A\beta$) peptides. According to the amyloid hypothesis, it is the production and aggregation of $A\beta$ in the brain that initiates a pathogenic cascade leading to AD dementia [20]. In the cascade, glia activation, synaptic injury, neurofibrillary tangles formation, and widespread neuronal death are considered sequential downstream events ignited by $A\beta$ deposition. The second phase is a mild cognitive impairment (MCI) due to AD. MCI is characterized by the earliest cognitive problems in a pre-dementia phase, such as impairment in episodic memory [21]. MCI symptoms are mild and do not

affect the daily activities of individuals. At this stage, individuals showing biomarker evidence for both $A\beta$ and neuronal injury will likely develop dementia over time. In the final phase, AD dementia advances with increasing severity, where cognitive impairment becomes significant to interfere with daily activities of individuals.

1.2 Amyloid plaques in Alzheimer's disease

The two neuropathological hallmarks of AD are the extracellular aggregation of $A\beta$ peptides in the brain to form amyloid plaques and the aggregation of tau proteins to form neurofibrillary tangles in neurons. $A\beta$ (between 38 and 43 amino acids) is derived from the proteolytic cleavage of amyloid precursor protein by a family of enzymes called β- and γ-secretases. $A\beta 42$ is known to be more amyloidogenic and toxic [22]. With an imbalance between production and clearance of $A\beta$ in the brain, $A\beta$ accumulates with time and aggregates to form higher-order structures from oligomers to fibrils with various level of toxicity to the synapses of neurons [23]. Amyloid plaque mainly constitutes $A\beta$ fibrils deposits. Tau tangle, on the other hand, appears to cause late-stage of neuronal dysfunction. It blocks the transport system of essential molecules and nutrients in neurons. In the course of AD, the accumulation of amyloid plaques in the brain is considered to be an early event compared to tau aggregation. Emerging evidence suggests amyloid plaques to accelerate tau pathology [24, 25]. It is worth looking at amyloid plaques if we want to detect early AD pathology. Fig. 1.2 shows a model by Jack et al. [2] that overall relates disease progression with the relative change in biomarkers. $A\beta$ level

increases early on and nears a plateau by the time tau-mediated neural injury, brain atrophy, and clinical symptoms of AD becomes apparent. However, the role of amyloid plaques in the severity of dementia is highly controversial [26, 27]. There are reports showing neurofibrillary tangles, not amyloid plaques, to predict cognitive decline and severity of AD [27, 28]. Recently, Hanseeuw et al. completed a seven-year longitudinal study to associate amyloid and tau with cognition [24]. Their findings suggest that measuring tau biomarker repetitively helps to track disease progression, whereas measuring amyloid is useful to detect AD pathology at the earliest stage.

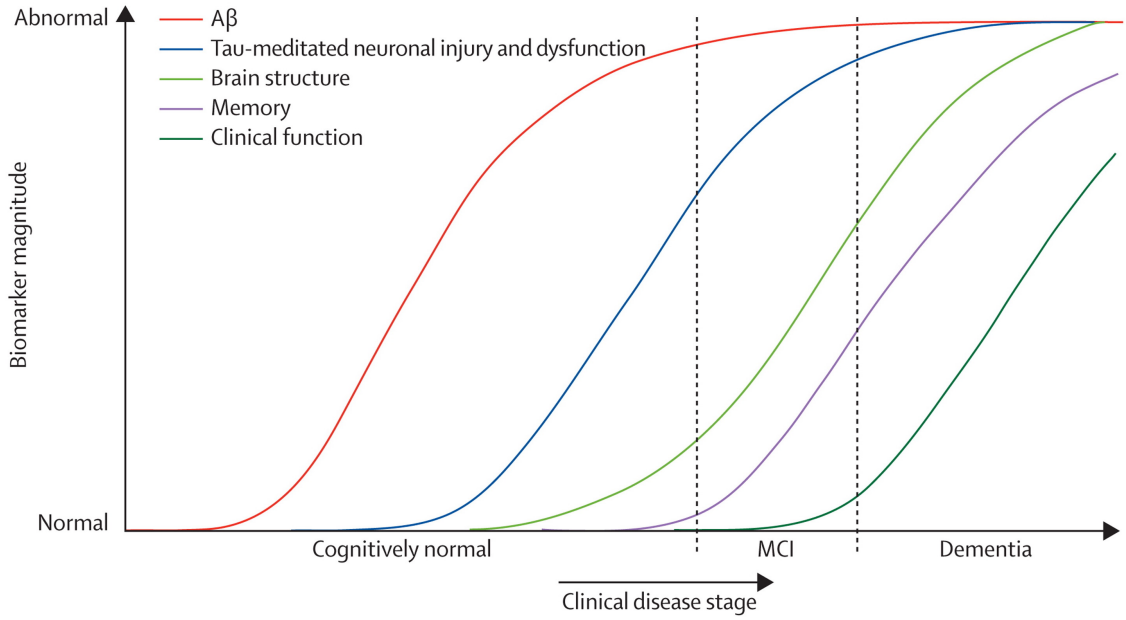


Figure 1.2: Changing biomarkers with AD progression [2]. Reprinted from Jack et al. Lancet Neurol 2010; 9:119-128, with permission from Elsevier.

Amyloid plaques accumulate progressively in different regions of the brain [29, 30]. Plaques are known to appear first in the neocortex. Based on the ABC stages proposed by Braak et al. [29,31], initial deposits of plaques (stage A) are found in the basal portions of neocortex covering frontal, temporal, and occipital lobes. In stage

B, plaque deposition increases towards the neighboring neocortical areas excluding the primary motor and sensory cortex. The hippocampus including subiculum are only mildly covered by plaques. Stage C is the more severe stage of plaque deposition with plaques seen in the entire neocortex. At this stage, plaques are also found in some subcortical structures such as striatum and hypothalamus. The sequence of amyloid deposition in the brain was later described in more detail in five phases by Thal et al. [30]. Irrespective of the staging scheme, early deposition of amyloid plaques start exclusively in the neocortex. Subcortical regions are affected at the later stage.

$A\beta$ fibrils that clump together to form amyloid plaques are highly structured insoluble fibers with cross-β sheets [8, 9]. Therefore, amyloid plaques have high β-sheet content [32]. Cross-β sheets are the repetitive secondary structure, where the β-sheets run parallel to the fibril axis and the constitutive β-strands run perpendicular. This defining feature was originally revealed by x-ray diffraction analysis of fibrils [33, 34] and further confirmed recently by analyzing amyloid plaques in the human and mouse brain tissues [5, 35]. Several Fourier-transform infrared (FTIR) spectroscopy studies have also shown the presence of β-sheet rich structures in fibrils and amyloid plaques [32, 36–38]. However, only x-ray diffraction can directly identify the repeating structure of the cross-β sheets. Schematics of the 2D x-ray diffraction pattern typical of fibrils and the cross-β sheet structure are presented in Fig. 1.3. The cross-β structure gives rise to distinct x-ray diffraction patterns at 4.7 Å and 10 Å corresponding to the β-strand and the β-sheet spacing respectively. This characteristic pattern is the basis for detecting and quantifying amyloid plaques in

our label-free method explored in this thesis. The challenge is to probe amyloid plaques in a brain enclosed by an intact skull.

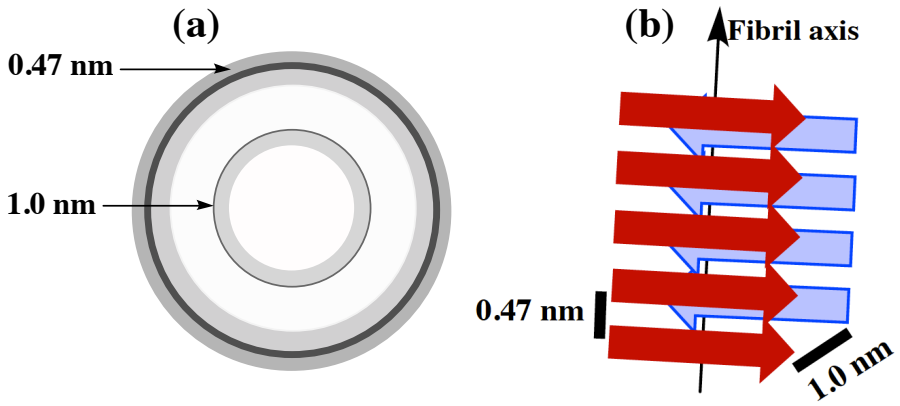


Figure 1.3: Schematic representation of the 2D x-ray diffraction pattern (a) typical from cross-β structures of amyloid fibrils (b). 0.47 nm is the repeating distance between adjacent β-strands and 1.0 nm is between β-sheets.

1.2.1 Brain amyloid burden estimation methods

Currently, positron emission tomography (PET) using amyloid specific radiotracer is the only clinically accepted method to estimate brain amyloid burden in humans *in vivo*. Magnetic resonance imaging (MRI) is often used concurrently with PET to image brain structure and its anatomical features. MRI is well known to provide evidence of brain atrophy in AD. With the help of an amyloid specific radiotracer, PET can perform relative quantification of amyloid burden. Likewise, there is active research in MRI to develop a contrast agent and imaging protocol to estimate amyloid burden. There are several methods to estimate brain amyloid burden *in vivo* or *ex vivo* with their own advantages and drawbacks (Table 1.1). In this section, we cover state-of-the-art methods as well as methods under development to

Modality	Mechanism	Main limitation	Application
Optical	Fluorescent dyes	Superficial targets, invasive	Animals, ex vivo
PET	Amyloid tracer	Off-target binding, expensive	Humans, in vivo
MRI/CT	Contrast agent	Non-specific, off-target binding	Animals, in vivo
Phase contrast	Phase retrieval	Synchrotron, radiation dose	Animals, ex vivo

Table 1.1: Summary of methods to estimate brain amyloid burden.

study small-animals (mouse models of AD) and humans in preclinical and clinical settings.

Optical imaging: The majority of amyloid plaques are in sub-100 μm range with 20 to 100 μm separation distance to nearest neighbor [39, 40]. Optical methods allow direct high-resolution imaging of amyloid plaques, but they are limited to *ex vivo* study of brain slice [41] or superficial imaging of *in vivo* brain after craniotomy [42, 43]. This is due to the high scattering and limited penetration depth of light. Fluorescent dyes such as thioflavin S and methoxy XO4 have been used for multiphoton imaging of amyloid plaques [44, 45]. Recently, tissue clearing method with light-sheet microscopy is proven to be a useful tool to map amyloid plaques in the whole brain *ex vivo* [40]. While it offers more information than histology, it takes anywhere from a few days to months to complete tissue clearing protocols and perform 3D imaging of an intact brain [46].

Post-mortem histological analysis is considered the gold standard to detect amyloid plaques in the brain tissue of small animals and humans. Histology is performed by staining selected brain slices (10 to 50 μm thin) with an amyloid specific dye (e.g., thioflavin S, Congo red) and acquiring images using fluorescent or polarized light microscopy [47]. Amyloid load is commonly defined as the percent area

covered by plaques in the region of interest. AD can only be detected definitely in humans with post-mortem histological analysis. Due to its high accuracy, histology is also the method of choice for preclinical research that uses various mouse models of AD. However, the process is very time-consuming as it requires days to prepare thin brain slices and to stain and image them individually. Moreover, to track disease trajectory, mice must be sacrificed at different stages of development, making longitudinal studies impossible.

Amyloid PET: Currently, amyloid positron emission tomography (amyloid PET) is the only clinically accepted *in vivo* amyloid imaging method with several radiotracers approved by the FDA [48–50]. It is an expensive, resource-intensive method due to the use of amyloid-specific radiotracer and PET scanner for the whole-brain imaging. Amyloid PET in clinical studies has sensitivity and specificity of greater than 80% [51]. Amyloid load/burden is a widely accepted outcome measure in PET for quantifying amyloid plaques. The amyloid load is calculated in terms of the standardized uptake value ratio (SUVR), where SUVR is the ratio of standardized uptake value (SUV) in the region of interest over SUV of a reference region such as the cerebellum. However, non-specific uptake of tracer in the regions of the brain without amyloids is an unavoidable problem. A cut-off SUVR value needs to be carefully determined to avoid false amyloid positive due to non-specific uptake that varies among patients. It is also worth mentioning that amyloid PET does not work as expected in mouse models of AD [52–54]. The amyloid tracer that is validated in humans has a poor performance in mice due to the binding issues of radiotracers in the mouse brain [55], suggesting the need for a label-free method to

overcome this issue. Klunk et al. performed micro-PET studies using Pittsburgh Compound-B tracer (PiB) in transgenic (APP/PS1) mice with low to high level of amyloid plaques in the brain [55]. Compared to the littermate controls (PS1), APP/PS1 mice showed no significant difference in the retention of PiB. This was attributed to poor binding of PiB to amyloid plaques in transgenic mice.

Historically, the development of the PiB tracer allowed researchers to extensively use PET to analyze amyloid load [56, 57] and investigate its correlation with cognitive impairment at various stages of AD [17, 58, 59]. PiB is a carbon-11 derivative of the thioflavin-T amyloid dye that can reach the brain and bind specifically to $A\beta$ fibrils. Despite its popularity, PiB routine clinical use is limited due to its short 20 minutes half-life. Therefore, a ^{18}F amyloid tracer having a radioactive half-life of 110 minutes is now commercially developed for clinical use [60, 61]. The number of available amyloid tracers for PET scans has increased significantly in recent years. Each tracer has slightly different properties, image acquisition protocols, and reference regions for analysis. This has lead to high variability in the outcome measure of amyloid load. Thus, an effort has been made to standardize amyloid PET data by introducing the Centiloid metric in the scale of 0 to 100, where 0 represents amyloid negative brain with high certainty and 100 represents amyloid positive brain with high amount of amyloid plaques typical of mild to moderate AD subject [62]. The standard Centiloid value (CL) is defined as

$$CL = 100\left(\frac{SUVR_i - \overline{SUVR}_{YC-0}}{\overline{SUVR}_{AD-100} - \overline{SUVR}_{YC-0}}\right), \tag{1.1}$$

where $SUVR_i$ is the SUVR value for each individual, $\overline{SUVR}_{YC-0}$ is the mean SUVR of the young control subjects, and $\overline{SUVR}_{AD-100}$ is the mean SUVR of the typical AD patients. Note that the CL scale was originally defined using the PiB tracer.

MRI and X-ray based techniques: Magnetic resonance imaging (MRI) and x-ray absorption based computed tomography (CT) are well known for the structural imaging of brain anatomy. However, neither of this imaging modality alone or combined has a necessary contrast to reliably visualize plaques in the brain. CT has no absorption contrast between plaques and background tissue. There are few positive and negative reports of MRI based label-free detection of amyloid plaques in AD mice *in vivo* and human brain tissue *ex vivo* [63–66]. The intrinsic MRI contrast of plaques depends on iron content, so it may not be a reliable detection mechanism. There are also non-specific dark spots seen in MRI images that are not associated with plaques. As a result, recent efforts have been focused on developing a contrast-enhanced MRI technique, where an exogenous contrast agent such as gadolinium is administered in mice to detect amyloid plaques with the sensitivity threshold of around 30 μm [67].

Phase contrast x-ray tomography is another commonly reported technique for label-free identification of amyloid plaques [68–71]. Phase contrast can visualize the distribution of plaques with high resolution and contrast. It has shown great potential to quantify amyloid burden in the brain tissue [69]. Nevertheless, it is limited to study brain samples *ex vivo*, and most of the studies are done at synchrotron facilities to use high flux, micro-focused x-ray source. So far, amyloid plaques cannot be resolved in the presence of the skull in the phase contrast method, thereby

making the method not suitable for *in vivo* study. It is reported that phase shift information between amyloid plaques and brain tissue cannot be accurately retrieved due to the high phase contrast of the skull along with its strong attenuation [69,72]. High radiation dose would be another issue to consider while using x-ray based techniques.

There is no method that can efficiently and accurately track amyloid burden *in vivo* without using contrast agents to accelerate AD research for disease diagnosis and drug development. Towards this end, we aim to develop a label-free non-invasive method using spectral small-angle x-ray scattering (sSAXS) to estimate brain amyloid burden *in vivo*. This is done by leveraging the penetration power of x rays at higher energies and capturing intrinsic SAXS signal specific to amyloid plaques in angle and energy dispersive modes. We now describe the concepts behind SAXS and sSAXS techniques.

1.3 Small-angle x-ray scattering

We start with some basics of x-ray interaction. X-rays are electromagnetic radiation similar to light, but with much shorter wavelengths in the range of about 0.01 to 10 nm. The wavelength, λ, is related to the photon energy, E, by

$$E = \frac{hc}{\lambda}, \tag{1.2}$$

where h is Plank's constant, 6.626 x 10^{-34} (J.s), c is the speed of light, 2.998 x 10^{8} (m/s), and 1 Joule (J) = 6.242 x 10^{15} keV. When an x-ray beam passes through a

material, x-ray photons are absorbed and scattered in the interaction process. Absorption is based on the photoelectric effect, where an incident photon is completely absorbed by an atom, ejecting an electron from its shell. The decreased number of transmitted photons due to absorption can be expressed as

$$I(E) = I_0(E)e^{-\mu(E)t}, \tag{1.3}$$

where $I_0(E)$ is the incident photon counts, $\mu(E)$ is linear x-ray attenuation coefficient of a material for each energy, and t is the material thickness. $\mu(E)$ decreases with energy [73], so higher energy can be used to minimize absorption and increase penetration depth. An x-ray beam can travel $1/\mu$ distance before its photon counts drops to $1/e$ of its initial value. Therefore, depending on the x-ray energy used, the optimal sample thickness in the scattering study is considered to be

$$t_{opt} = \frac{1}{\mu(E)} \tag{1.4}$$

X-ray scattering can be elastic or inelastic. The elastic scattering process is where photons interact with strongly bound electrons and scatter without losing energy. The state of the electron is unchanged. It is also referred as coherent or Rayleigh scattering. In inelastic scattering, the photon scatters by imparting some energy to recoiling electrons. Photon deflects from its original path with a longer wavelength. The deflection angle is usually wide and increases with energy loss. Inelastic scattering is also called Compton or incoherent scattering. At small scat-

tering angles and lower energies, it is known that the scattering process is dominated by elastic scattering [74–76].

1.3.1 Theory

Small-angle x-ray scattering (SAXS) is a well-established technique that measures elastic scattering at low angles (typically 0.1-10°) and provides nano-scale structural information of sample including shape, size, internal structure, and crystallinity [77–79]. The scattering signature in SAXS is based on the molecular structure of the material and its nanoscale arrangement. The scattering contrast is based on the intrinsic electron density difference of the material and its residing medium. Therefore, SAXS is a label-free characterization technique that is suitable for detecting and studying biological structures in their native environment.

A schematic of the scattering process for a single particle is shown in Fig. 1.4. Let a primary x-ray beam of wave vector $\vec{k_o}$ irradiate an arbitrary particle at point p. A fraction of this beam elastically scatters at 2θ angle with wave vector $\vec{k_1}$. Since the scattering process is elastic, we have $|\vec{k_o}| = |\vec{k_1}| = 2\pi/\lambda$. The scattering or momentum transfer vector is defined as

$$\vec{q} = \vec{k_1} - \vec{k_o}, \tag{1.5}$$

where $q = |\vec{q}| = 2(\frac{2\pi}{\lambda})sin\theta$, as such

$$q = \frac{4\pi \sin\theta}{\lambda} \tag{1.6}$$

All SAXS data are analyzed in terms of q (nm^{-1}). Since q is in reciprocal space, the scattering from a large structure appears at a lower q and vice versa.

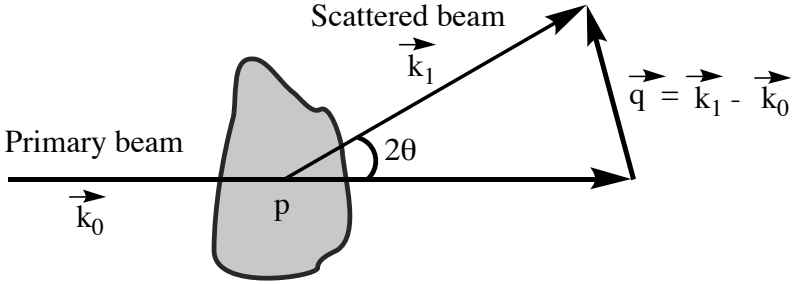


Figure 1.4: Schematic of the scattering process to define scattering or momentum transfer vector $\vec{q}$.

Mathematically, the scattering amplitude $f(q)$ is the Fourier transform of $\Delta\rho(r)$ given by

$$f(q) = \int_V \Delta\rho(r) exp(-iq.r) dr, \tag{1.7}$$

where $\Delta\rho(r)$ is the electron density difference of a particle with respect to its residing medium at position r and q is the momentum transfer vector in the elastic scattering process. It is necessary to have inhomogeneities in electron density inside the sample to see the scattering signal. The scattering intensity $I(q)$ that we measure is the square modulus of $f(q)$ given by $I(q) = |f(q)|^2$. For an ensemble of identical particles, $I(q) = \langle |f(q)|^2 \rangle$ represents scattering from a single particle averaged over all orientations. To account for inter-particle interference, the scattering intensity for spherical particles can written as

$$I(q)_s = \langle |f(q)|^2 \rangle S(q), \tag{1.8}$$

where S(q) is the interference term called structure factor describing interactions

between neighbouring particles [77, 78].

1.3.2 Instrumentation

Schematic of a typical SAXS setup with sample scattering curves acquired from cylindrical and spherical structures are shown in Fig. 1.5. The setup has a monochromatic x-ray beam that is collimated to irradiate a thin sample and a detector with a primary beam stop to collect scattered x-rays at small angles (Fig. 1.5). The entire beam path is vacuumed below 3 mbar to avoid scattering from the air. A common source of the monochromatic x-ray beam in a laboratory setting is either copper K-alpha (8.05 keV, $\lambda = 1.54$ Å) or molybdenum K-alpha (17.45 keV, $\lambda = 0.71$ Å). So the emitted spectrum from an x-ray tube (with copper or molybdenum anode) needs to be filtered to get monochromatic x-rays. The monochromatic x-ray beam is collimated to get a focused beam with small divergence. We are limited to study a few millimeters thick samples due to the low energy of monochromatic x-rays. For instance, the optimal sample thickness using copper K-alpha is 1 mm or less.

A collimation system is usually based on slits, blocks, or pinholes. Slits or blocks are used for line collimation, and pinholes are used for point collimation. Line collimation forms a line beam (typically 10 mm wide) with high x-ray flux and large sample illumination volume. This reduces the measurement time but adds slit smearing that significantly broadens and smears the scattering signal. Therefore, it is necessary to measure the beam profile and perform desmearing of the acquired

data in the post-processing steps to reduce the smearing effect [80]. Moreover, line collimation cannot be used if we aim to record anisotropic scattering. Using a pinhole collimation system, on the other hand, produces a pencil beam with beam spot size in the range of 100 to 300 μm. Point collimation allows a high-resolution SAXS measurement without the need to de-smear the data. The trade-off is long measurement times (hours to days) due to the significant reduction in the x-ray flux and the small sample illumination volume.

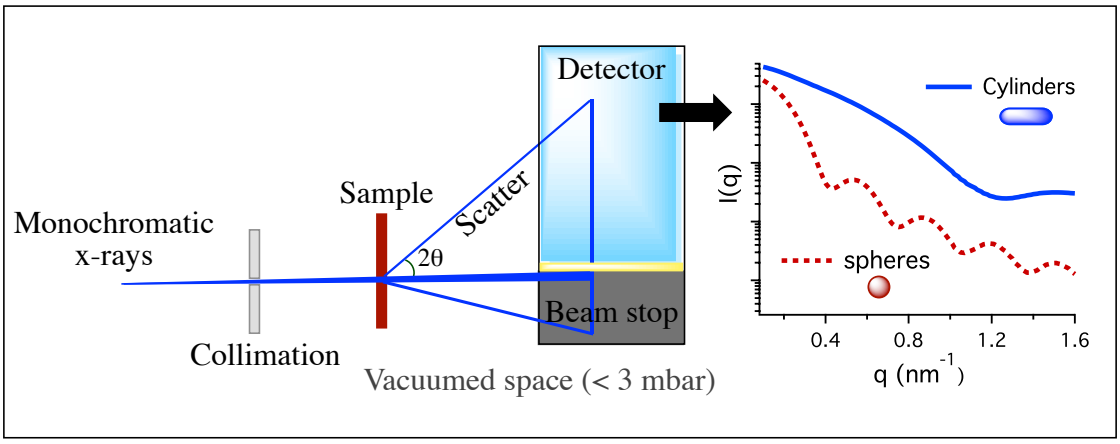


Figure 1.5: Schematic of a typical SAXS setup to obtain structure sensitive data. Distinct scattering curves from cylindrical and spherical structures are shown as an example.

A charged-coupled device (CCD) detector is widely used as an integrating detector in the SAXS instrument, although the current trend is shifting towards using a photon-counting detector [81–83]. The CCD detector works by first converting x-rays to visible light for indirect detection usually via a large phosphor screen. The phosphor screen is fiber-optically coupled to the CCD chip to guide the light. The CCD needs to be cooled around -40 °C to reduce dark current. Photoelectrons are produced at each pixel location impinged by light. The produced electrons are col-

lected in each pixel over an integration time before the readout to map the intensity pattern. Each pixel (p_n) can be assigned a scattering angle based on the system geometry by using

$$2\theta = arctan(\frac{p_n p_x}{d}), \tag{1.9}$$

where 2θ is the scattering angle, p_x is the pixel pitch, and d is the sample to detector distance. 2θ is related to q by Eq. 1.6, where $q = \frac{4\pi \sin\theta}{\lambda}$.

We can obtain a 1D scattering curve, $I(q)$, by radial averaging of the 2D detector data. This data reduction approach is used by assuming isotropic scattering. To obtain the scattering pattern from the structures alone, we can perform background subtraction as

$$I(q) = I_s(q) - T_f I_b(q), \tag{1.10}$$

where $I_s(q)$ and $I_b(q)$ are the scattering intensity of the sample and background respectively, and T_f is the scaling factor based on the transmission of the sample and background. Dark current should be removed from $I_s(q)$ and $I_b(q)$ before background correction. $I_b(q)$ is obtained from the buffer or matrix alone in which structures are present. Further data reduction to absolute scale can be done using water [84] or glassy carbon [85].

SAXS has been applied to 2D and 3D *ex vivo* imaging of brain, bone, and other tissue structures without any contrast agents [86–89]. High-resolution SAXS studies are mostly done at synchrotron facilities using a micropencil beam of high flux monochromatic x-rays. In the past, our group has used a commercially available laboratory SAXS setup to demonstrate a structure-sensitive method to characterize

biomolecular interactions [90], to characterize the scattering cross-section of solid and liquid imaging materials [91], and to demonstrate 2D imaging of phantoms and brain tissues [92]. Monte Carlo x-ray transport simulation tools are also well-developed to explore SAXS instrument design choices [93–96]. Choi et al. have initially studied the feasibility of using SAXS for the detection of amyloid plaques in AD [97, 98]. The reported work experimentally studied the 1 mm mouse brain slices and found higher scattering intensities from amyloid plaques at q below 0.8 nm^{-1}. It took 60.5 hours to scan each slice in this particular study. In addition, the high intensity low-q data can be acquired from any protein aggregates. Thus, it may be challenging to differentiate amyloid and non-amyloid protein aggregates in the thin brain slice using this approach. Monte Carlo simulation studies have, nevertheless, supported the feasibility of detecting amyloid plaques *in vivo* in the mouse and human heads using higher energy x-rays [98]. To enable the practical application of SAXS towards *in vivo* study, we propose a spectral SAXS method for experimentally identifying amyloid plaques in an intact brain with skull.

1.4 Spectral SAXS

The concept behind spectral SAXS (sSAXS) is to collect scattered x ray photons simultaneously in angle- and energy-dispersive modes. Angle-resolved SAXS data is measured without filtering the energy spectrum. This allows full utilization of available x-ray flux and scattering information to reduce measurement time in a laboratory setting. We can choose the energy range of interest to probe thick

samples. Ideally, we want to probe 1 to 20 cm thick samples within minutes to open the possibility of quickly and non-invasively study the intact head of both mice and humans.

As shown in Eq. 1.6, we can vary q by either changing λ or θ. Traditional SAXS collects q-data in angle-dispersive mode, where the scattering signal is measured as a function of scattering angle at fixed energy using monochromatic x-rays. Energy-dispersive SAXS (EDSAXS) measures the scattering signal as a function of energy for a fixed angle. EDSAXS employs a polychromatic x-ray source to irradiate the sample. An energy-sensitive detector is placed at a constant scattering angle to record scattered x-ray energy. While angle-dispersive SAXS has a high angular resolution, EDSAXS offers a faster data acquisition time to access the same q-range. Schultz and Long [99] and Bordas and Munro [100] have done pioneering work on EDSAXS in the 1970s. Bordas and Munro obtained the energy-dispersive scattering pattern from rat-tail collagen in 200 seconds using the synchrotron radiation [100]. The angular acceptance of the detector was defined by placing a lead collimator in front of the detector. Various experimental approaches to EDSAXS and its application has been reported since then [101–104]. The major drawback of EDSAXS is low q-resolution. With low q-resolution, we may not be able to resolve sharp peaks at well-defined q-values.

With recent advancements in semiconductor-based pixellated, energy resolving x-ray detector [105–107], it is possible to measure scattered photons simultaneously in angle- and energy-dispersive modes. X-ray diffraction (XRD) studies have used a similar approach in the past to detect explosives or illicit drugs, where a 2D

spectroscopic detector was used to collect full energy spectrum and scattering angle information in each pixel [108, 109]. We can capture the angular distribution and energy information of scattered photons across pixels without moving the detector or using collimators. Moss et al. have recently utilized angle- and energy-dispersive XRD to record scattering patterns from breast tissue samples (up to 5 mm thick) and use them to discriminate between normal and tumorous tissue types [110]. Conceptually, when studying samples with periodic structure, there is no difference between sSAXS and angle- and energy-dispersive XRD, except the q-range we are accessing while probing thick samples in the cm scale. Therefore, the innovation of our work is in designing and building a prototype sSAXS system tailored towards identifying amyloid plaques *in vivo*. We aim to do this by efficiently integrating a laboratory x-ray source and a 2D spectroscopic detector to cover the q-range of interest. We will provide a general introduction to the spectroscopic detector before delving into the sSAXS prototype in the second chapter.

Conventional energy-integrating detectors measure the energy-integrated signals of x-ray events over a fixed acquisition time. The electrical signal is proportional to the total deposited energy in the detector, thereby losing energy information of an individual photon. In contrast, photon-counting detectors with energy-resolving capabilities can record the energy of each photon interacting with the detector sensor material. For direct detection of x rays, semiconductor-based sensor materials are used. Energy is deposited by each photon and directly converted to electron–hole pairs. The basic principle of a semiconductor-based photon-counting detector is to detect charges generated by each photon interaction and process them to output

voltage signal (mV) with its amplitude or height directly proportional to the deposited energy (keV). We get the energy spectrum by measuring the peak amplitude of voltage pulse for thousands of such interactions and plotting a histogram showing number of counts with energy (peak amplitude) information. The raw data is energy calibrated by using a radioactive isotope such as Americium-241 or Cobalt-57 with known energy peaks in the keV range [109, 111].

Cadmium telluride (CdTe) is a commonly used semiconductor material for x-ray detection [112]. It has a high density (6.20 g/cm^3) and wide band-gap (1.44 eV) to efficiently absorb high energy x-rays and operate at room temperature. A 2D spectroscopic detector consists of a single CdTe crystal with electrodes and an application-specific integrated circuit (ASIC) [113, 114]. The typical size of CdTe crystal in a commercially available detector is 20 x 20 x 1 mm^3. X-rays enter through a planar cathode to interact with CdTe. An anode is uniformly divided into pixels and connected to ASIC via bump bonds for pixel readout. The pixellated anode is commonly fabricated using aluminum [115].

When an x-ray photon of energy E interacts with CdTe and deposits its energy, it generates $N_e = E/w$ number of electron-hole pairs, where w is the pair creation energy [116]. w for 1 mm thick CdTe is 4.43 eV. Since the generated charge is proportional to the x-ray energy, it is necessary to measure and process the total charge per interaction to recover the energy information of the incident photon. A bias voltage is applied across the electrodes to create an electric field and move electrons and holes towards the anode and cathode respectively. The movement of electrons and holes create a transient current that is then processed by the ASIC.

Shockley–Ramo theorem describes the signal generation process on the electrode from the moving charge [117]. The pixel electronics of ASIC consists of a charge sensitive preamplifier, a shaping amplifier, and a peak hold circuit [118, 119]. The charge sensitive preamplifier integrates the transient current and generates a voltage signal proportional to the collected charge. This voltage signal is shaped by a shaping amplifier and a low pass filter for the readout of peak amplitude. The peak hold circuit maintains the voltage corresponding to peak amplitude until the multiplex readout of pixels. A rolling row readout scheme has been used to read a full frame of 80 by 80 pixels at a rate of 9 kHz [107].

The performance of 2D photon-counting detectors is not perfect. There are various phenomena when detecting x-ray photons that cause degradation of measured photon counts and energy spectra [120, 121]. These include pulse pileup, charge sharing, K-escape x-rays, Compton scattering, charge trapping, and polarization. We briefly discuss pulse pileup and charge sharing phenomena, as they are major problems of the photon-counting detector. The detector generates a voltage pulse for each incident photon with its amplitude proportional to the deposited energy. When several overlapping pulses are generated by quasi-coincident photons, especially with high x-ray flux, they may pile up and be detected as one pulse. Due to this pulse pileup phenomenon, the detector records a singe count for multiple photons with incorrect energy. Pulse pileup can be reduced by lowering the x-ray flux and using detectors with short dead-times. Charge sharing is another important phenomenon that causes spectral distortions [122]. The electron charge cloud created by an absorbed photon in the semiconductor drifts towards the pixellated

anode of the detector under the electric field. For an interaction near a pixel boundary, the charge cloud may be divided and detected by neighboring pixels, thereby recording lower than the original photon energy. The distribution of energy with charge sharing among multiple pixels causes distorted energy spectra. In addition, the probability of double counting the same photon increases if a low energy threshold is used. Charge sharing is significant in detectors using small pixel geometries. One option to correct for charge-sharing is by inspecting the nearest neighboring pixels for each frame to remove shared events [123, 124]. There are also detector models to predict charge sharing events [122, 125].

1.5 Thesis scope

In this chapter, we have provided a general overview of relevant topics covered in this thesis from Alzheimer's disease to small-angle x-ray scattering, along with the motivation for our work.

In chapter 2, we present the development and validation of sSAXS prototype system. The data analysis method is described in detail. We use spectral SAXS (sSAXS) in the 30–45 keV energy range to identify embedded materials in up to 5-cm thick objects. This work shows that we can probe targets embedded in thick objects in the cm scale.

In chapter 3, we describe the preparation methods of amyloid models for phantom studies. Amyloid model mimicking amyloid plaques in the brain allows us to readily test the feasibility of using a label-free x-ray method for estimating brain

amyloid load without using mice models of AD.

In chapter 4, we characterize target made from amyloid models in a wild type mouse head using spectral SAXS. We show results for estimating the amyloid load in a fixed mouse head with skull by recovering the characteristic scattering signal from the amyloid target situated at various locations.

In chapter 5, we present a label-free estimation of brain amyloid burden using a mouse model of AD. Using 5XFAD mice, we demonstrate an sSAXS method to estimate amyloid burden within minutes with no contrast agents. This work opens new possibilities of conducting more efficient longitudinal mice studies tracking amyloid burden.

In chapter 6, we summarize the overall contribution of this thesis and provide future directions to study small-animals and humans.

Chapter 2: Development and validation of an sSAXS prototype

In this chapter, I describe and validate a prototype sSAXS system built from a polychromatic x-ray source and a 2D spectroscopic detector. The use of sSAXS in the 30–45 keV energy range was investigated to identify embedded materials in up to 5-cm thick objects. The elastically scattered x rays at deflection angles smaller than 10° were measured without collimating the scattered rays or filtering the energy spectrum. The prototype was validated in a general setting using easy to detect caffeine target with sharp Bragg peaks before studying amyloids. Peaks of caffeine and amyloids are in the same q-range [5, 108]. Therefore, our first validation study, along with the refinement of the data analysis method, was done just using caffeine. Using caffeine as a target material in 1 to 5 cm polymethyl methacrylate (PMMA) slabs, we demonstrate the capability of sSAXS technique to identify caffeine targets within 600 seconds. Furthermore, we show the effect of PMMA thickness and target location to estimate the caffeine amount from the recovered signal using area-under-the-peak (AUP) analysis.

2.1 Introduction

When an x-ray beam irradiates a material, the primary x-ray photons that are not transmitted through are either absorbed or scattered in the interaction process. Some photons may elastically scatter without losing energy, while others may incoherently scatter by imparting some energy to secondary electrons. Small-angle x-ray scattering (SAXS) is a well-established technique that measures elastically scattered x rays at angles below 10° and provides molecular level structural information [76]. Incoherent scattering events are negligible at small angles. In a traditional SAXS setup, a sample is irradiated by a focused beam of monochromatic x rays in transmission mode to acquire a scattering pattern as a function of momentum transfer q. The scattering pattern in reciprocal space (q-space) is determined by the molecular structure of the sample. Therefore, SAXS is known to identify materials based on their scattering features [92]. However, it has been so far limited to study thin samples in the mm scale [98, 126, 127]. This is due to the use of low-energy monochromatic ($<$ 20 keV) x rays in both laboratory and synchrotron facilities to collect high resolution angle-resolved SAXS data. Object size can be a limiting factor while exploring novel *in vivo* applications, such as identifying amyloid plaques in the brain [5].

Due to recent advancements in semiconductor 2D photon-counting detectors, it may be possible not only to use high energy x rays to study thick samples in the cm scale, but also to fully utilize the available x-ray flux in the energy range of choice without filtration of the incident beam. Recently, a cadmium telluride (CdTe) pixelated detector (HEXITEC) has shown promising results in angular and energy

dispersive x-ray diffraction studies for detecting explosives and drugs in 3 to 5 mm thick samples [108,128]. Its application specific integrated circuit processes the pixel charge collected in each photon interaction within the CdTe sensor. As a result, the energy spectrum of scattered photons in each pixel is captured in addition to the angular distribution information across pixels. Charge-sharing and energy dependencies may degrade the performance of the detector in the SAXS study. Likewise, the task of identifying embedded targets in thick objects is usually challenging because of the strong energy-dependent absorption, high background scattering, low angular resolution, and spurious signal from multiple scattering. Choi et al. reported detail Monte Carlo simulations of the SAXS setup in 5–95 keV energy range to study gold nanoparticles in aqueous solution samples with thickness varying from 1 mm to 10 cm [93]. The x-ray source was simulated as a monochromatic pencil beam and its energy was varied in steps of 1 keV. Most importantly, all the scattering contributions from coherent (elastic), Compton, and multiple-scattering were taken into account to conclude that the energy range between 31 to 49 keV would produce the most elastic scattering per deposited energy at small angles for this particular case. Multiple scattering remains a degrading factor for samples with high scattering power or transmission below 90% [129].

We experimentally investigated the use of spectral SAXS (sSAXS) in the 30-45 keV energy range to identify embedded targets in up to 5 cm thick objects. A prototype sSAXS system was built by integrating a high energy polychromatic x-ray source and a HEXITEC detector in a two-pinhole collimation setup. To obtain scattering information in the q range of interest, the scattered x-ray photons at

deflection angles smaller than 10° were measured by the detector without collimating the scattered x rays or filtering the energy spectrum. Caffeine powder was used as a target embedded in objects made from 1 to 5 cm polymethyl methacrylate (PMMA) slabs. We also studied the effect of PMMA thickness and target location in estimating the caffeine amount from the recovered signal using area-under-the-peak analysis.

2.2 Methods

2.2.1 A prototype sSAXS system

A prototype sSAXS system was built by integrating a high energy polychromatic x-ray source (tungsten anode, MXR-160/22, COMET) and a 2D spectroscopic detector made from CdTe (HEXITEC, Quantum Detectors Ltd, Oxfordshire, UK) in a two pinhole collimation setup. The air between source-to-detector was not vacuumed. The schematic of the setup is shown in Fig. 2.1. A picture of the laboratory prototype is shown in Fig. 2.2. Polychromatic x rays, generated using a tube voltage of 50 kVp and a current of 1 mA, were focused onto the sample using two lead pinhole collimators, P1 and P2, of 2.5 and 0.5 mm diameters respectively. P2 was 160 mm far from P1, and the detector was placed 220 mm from P2 to collect scattered photons between 6 and 50 keV using -400 V bias voltage, 5 keV energy threshold, 1 keV energy binning, and 600 s acquisition time. The CdTe detector with 1 mm thickness has 80×80 pixels and 250 μm pixel size. Each pixel can measure energy spectrum. A charge-sharing correction was applied using the charge sharing dis-

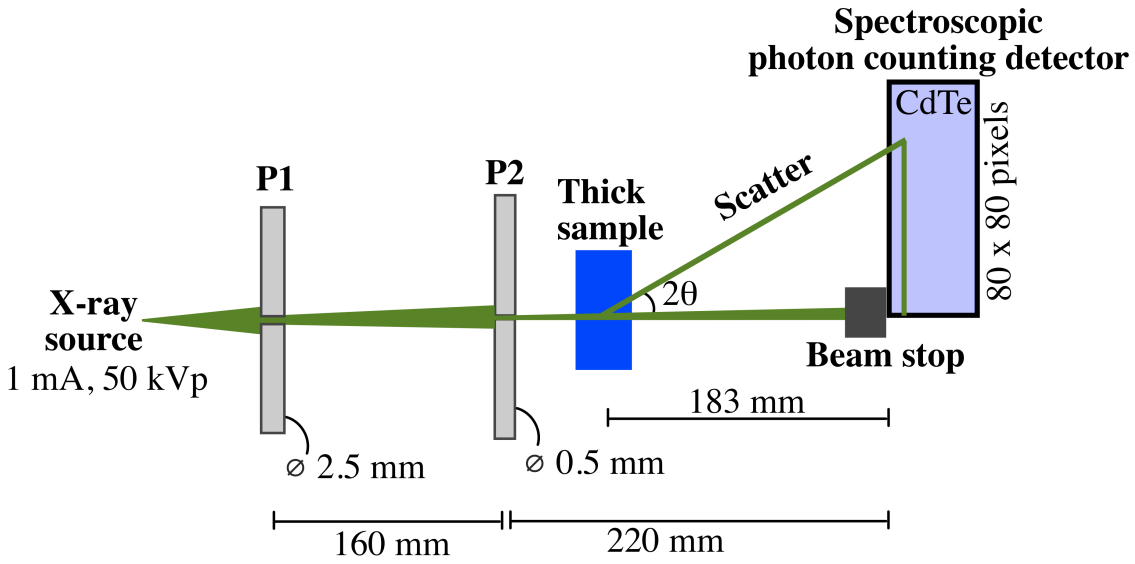


Figure 2.1: Schematic of a prototype sSAXS system to collect SAXS data from thick samples simultaneously in angle- and energy-dispersive modes. P1 and P2 are two lead pinhole collimators of 2.5 and 0.5 mm diameters respectively.

crimination algorithm, where the nearest neighboring pixels (3 x 3) were inspected to remove shared events [123].

With reference to the target location, the commonly used sample to detector distance (SDD) was 183 mm, unless otherwise noted. While collecting the scattering data, the beam stop was placed in front of the detector to block the primary beam to avoid spectral degradation from pulse pile-up. Gafchromic XR-M2 film was used to measure the beam spot size. The size of the beam reaching the sample after passing through P2 was around 0.5 mm. We want to note that an additional guard pinhole was not required in our setup because the parasitic scatter from pinholes was found to be negligible in comparison to the scatter signal from caffeine or PMMA. In addition, the transmitted photons of the incident beam from the samples were measured to perform energy-dependent corrections of the detector data. The transmission measurement was done on the same setup, but without the beam stop using 0.2 mA

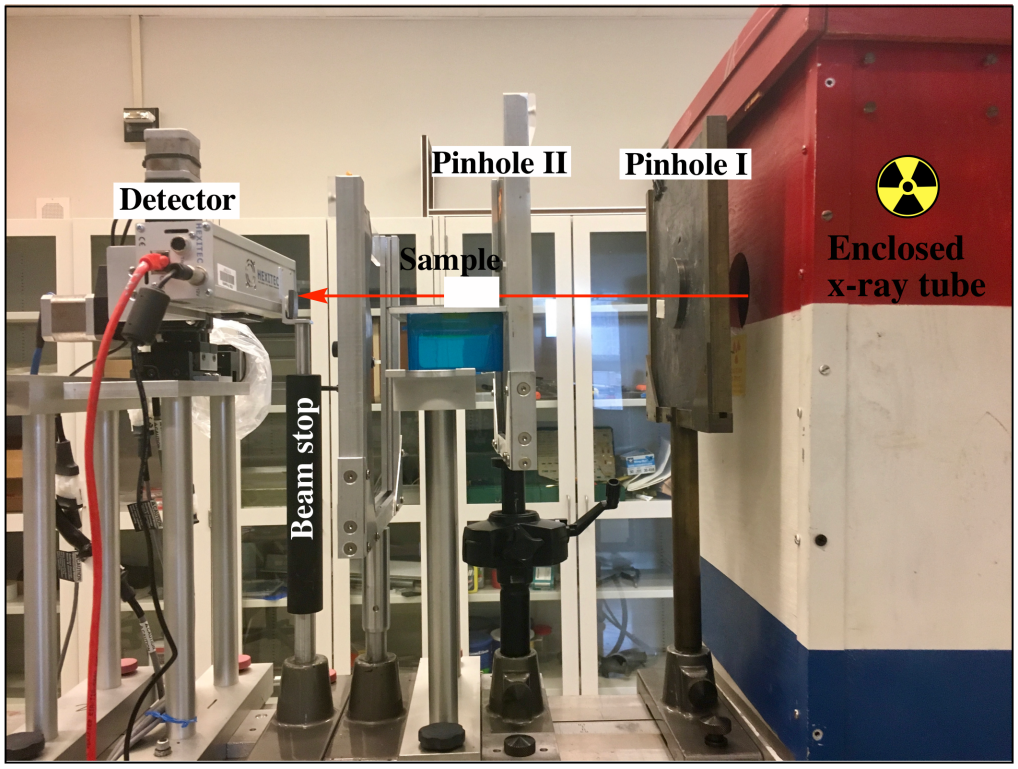


Figure 2.2: Picture of the laboratory prototype sSAXS system.

tube current, 300 s acquisition time, and 27 keV energy threshold. Total counts per energy bin in 8 by 8 pixels that covered the location of the transmitted beam were used to estimate the number of transmitted photons in 30–45 keV energy range. The accuracy of measuring the transmitted photons using this approach was evaluated using PMMA slabs of 1 to 5 cm thickness. The transmission factors of PMMA slabs of known thickness were compared with the reference values calculated using the x-ray mass attenuation coefficient data of PMMA from the National Institute of Standards and Technology (NIST) Standard Reference Database [3].

2.2.2 sSAXS data analysis

Based on the geometry of the system (Fig. 2.1), the scattered photons recorded in each pixel have a known scattering angle defined by 2θ. The momentum transfer q, energy E, and scattering angle are related by

$$q = \frac{4\pi E \sin\theta}{hc}, \tag{2.1}$$

where $hc = 1.24$ keV nm. Our sSAXS setup covered the q-range of interest from 1.3 to 28 nm^{-1} with E from 30 to 45 keV. Using 30–45 keV E also avoids the contamination of the scattering profile with fluorescence peaks of Cd and Te.

The 2D spectroscopic detector records counts and energy information of scattered photons in each pixel. Let $N_s(i, j, E)$ be the number of scattered photons reaching the detector, where (i, j) denotes the location of the pixel in 80 by 80 pixel array. If T is the sample thickness along the x-ray path, $N_s(i, j, E)$ is then given by

$$N_s(i, j, E) = N_t(i, j, E) \int_0^T S(x, \theta_{ij}, E)dx, \tag{2.2}$$

where $N_t(i, j, E)$ is the number of transmitted photons of incident beam and $S(x, \theta_{ij}, E)$ is the scattering cross-section distribution. Dividing $N_s(i, j, E)$ by $N_t(i, j, E)$ corrects for the energy-dependent attenuation of the sample. We assume the attenuation of incident and scattered photons for small angles can be combined and represented by the transmitted beam [130,131]. Using the transmitted spectrum for

correction also accounts for any energy-dependent detector response and quantum efficiency due to polychromatic x rays [132]. Both the raw counts and the scattering cross-section data were represented as a function of q per energy bin by using equation 2.1. The transmission corrected q-data were then summed for all energy bins from 30 to 45 keV. The background scattering was removed from the summed q-data to get the final $S(q)$. Subtracting the background directly from the raw data also gave the same result. We collected sSAXS data from the caffeine powder in a plastic syringe (6.4 mm diameter) to describe and validate the data analysis process using its known Bragg peaks. Background S(q) was acquired with an empty syringe by following the same data collection and processing steps as used for the caffeine sample.

2.3 Results and discussions

Fig. 2.3 presents the sSAXS data analysis workflow using caffeine data as an example. The analysis starts with taking the raw detector data of caffeine (SDD = 214 mm) in 30 to 45 keV and performing the transmission correction and q-conversion to get S(q) per energy bin. The transmission corrected q-data are then summed together (Δq = 1.2 nm^{-1}) for all energy bins. This approach allows to combine all the scattering information present at each E from a single measurement (Fig. 2.3b-c). Lastly, the background scattering from the summed q-data is removed to get only the known Bragg peaks of caffeine at 8.44 and 18.64 nm^{-1} (Fig. 2.3d). The 8.44 nm^{-1} and 18.64 nm^{-1} peaks respectively correspond to the 7.53–7.40 Å and

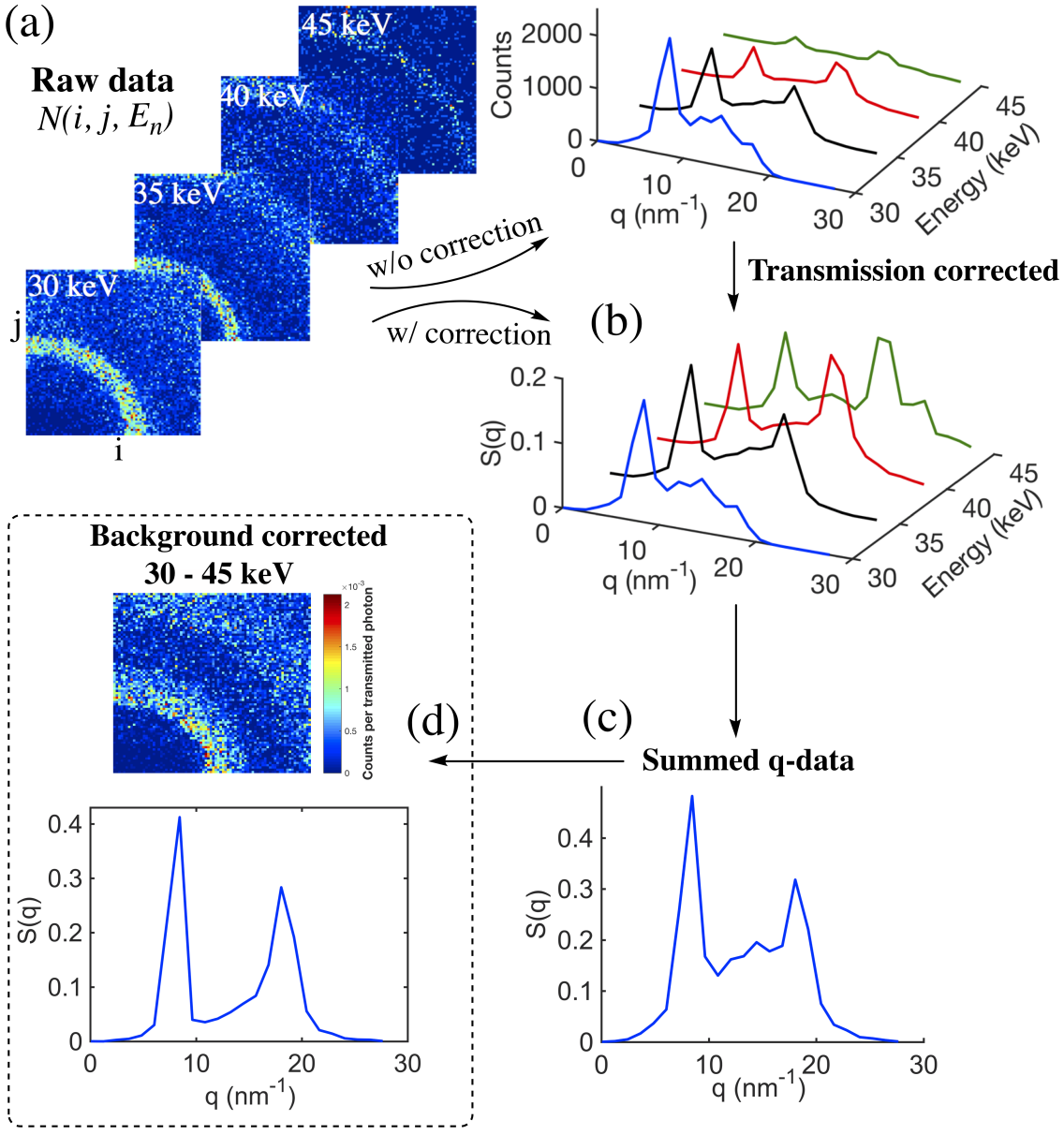


Figure 2.3: sSAXS data analysis workflow using caffeine sample as an example in 30–45 keV energy range. (a) Raw 2D detector data showing counts in each pixel per energy bin (left). Corresponding 1D data in terms of q without transmission correction (right). (b) Transmission corrected counts as a function of q per energy bin. (c) Summed q-data (Δq = 1.2 nm^{-1}) from 30 to 45 keV to get the scattering cross-section information, $S(q)$. (d) Background corrected counts per transmitted photon in each pixel (top) and the corresponding S(q) of caffeine with two Bragg peaks (bottom).

3.37–3.30 Å atomic spacings of caffeine [128]. While this validates the sSAXS setup to accurately capture the scattering information, it is also essential to separately assess the accuracy of measuring the transmitted intensity.

The transmission correction, which accounts for the attenuation of the incident and scattered photons inside the sample, depends on the spectroscopic measurement of the transmitted photons (30–45 keV). For this purpose, as shown in Fig. 2.4, we measured the transmitted photons through the PMMA slabs of 1, 3, and 5 cm thickness and found that their transmission factors agreed well with the reference values in 30–45 keV energy range. The accuracy was within 10%. The beam measurements with and without PMMA slabs were also stable in terms of the recorded counts as supported by the small error bars in Fig. 2.4a. Error bars represent standard deviations from three measurements.

After this validation study, we first investigated the use of sSAXS technique to identify the caffeine targets in 1 and 3 cm objects made from the PMMA slabs with target locations varying from F1 to B1 (Fig. 2.5a). F1, M1, and B1 represent the front, middle, and back target position respectively. For instance, when the caffeine target is embedded at M1, the x-ray beam consecutively encounters the first slab of PMMA, the caffeine target, and the second slab of PMMA. It should be noted that our caffeine target was a 6.4 mm plastic syringe filled with caffeine power and it was placed 183 mm from the detector to accommodate the PMMA slabs. The PMMA slabs were added or moved around the target to change the object size or vary the target location with respect to the object. All our sSAXS data in 30–45 keV energy range were processed and corrected by following the data analysis workflow

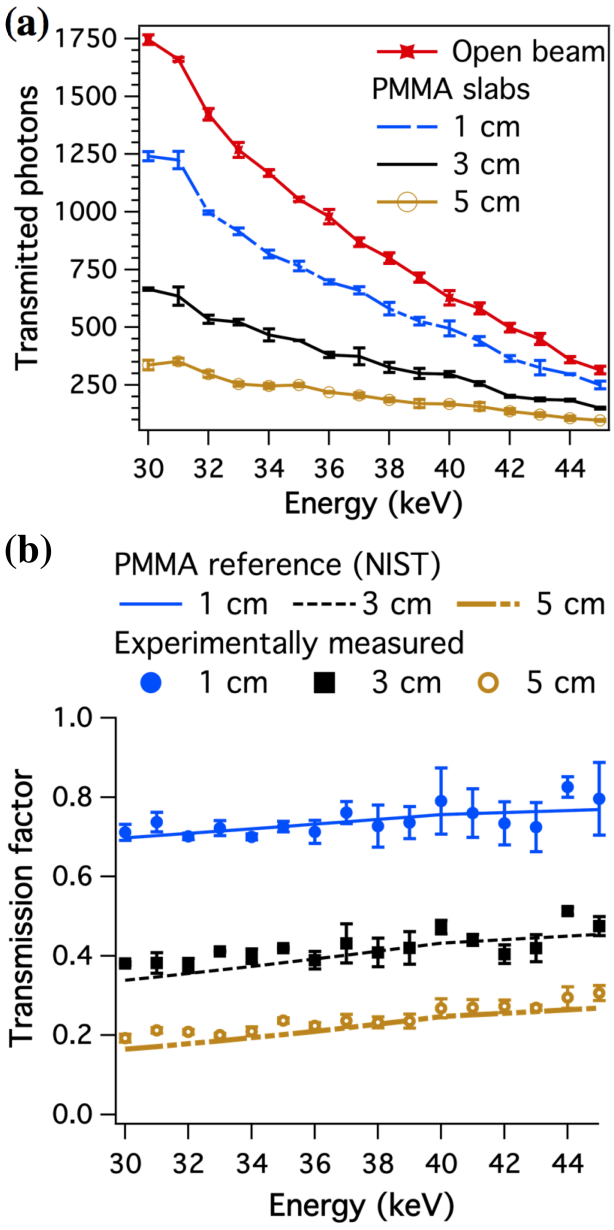


Figure 2.4: Validation of the transmission measurements. (a) Transmitted photons from the PMMA slabs of 1, 3, and 5 cm thickness. (b) Comparison of the transmission factor with the reference values from NIST using the mass attenuation coefficient values of PMMA [3].

presented in Fig. 2.3.

Fig. 2.5b shows that in the 1 cm PMMA, the Bragg peaks of caffeine at 8.44 and 18.64 nm^{-1} ($\Delta q = 0.6$ nm^{-1}) are recovered for all target positions from F1 to B1 after attenuation and background corrections. As a reference for comparison, we used a caffeine target study without any PMMA slabs. The corresponding area-under-the-peak (AUP) values from 7.24 to 9.64 nm^{-1} are presented in Fig. 2.5c to estimate the caffeine amount from the recovered signals. AUP is proportional to the caffeine amount. Since its the same caffeine target that was moved around the PMMA slabs, in principle, AUP should stay constant. However, we see that the mean AUP value is overestimated by about 7% when the caffeine target is at F1 in comparison to B1. F1 also has the highest coefficient of variation (CV $\approx$ 10%). The overall trend is similar for the caffeine targets in the 3 cm PMMA slabs, but we observe an increase in the background scattering and noise levels in the S(q) data (Fig. 2.5d), and the mean AUP at F1 is overestimated by about 11% (Fig. 2.5e).

Our results in Fig. 2.5 first demonstrate the capability of sSAXS technique to identify the caffeine target in the 1 and 3 cm PMMA slabs with varying target locations. The Bragg peaks associated with caffeine are clearly identified. The rise in noise or background scattering levels in the 3 cm PMMA study is likely due to the drop in transmission factor below 42% (on average) and the increase in multiple scattering events. Although we performed the transmission correction, we did not account for multiple scattering [129, 133]. Second, AUPs representing the caffeine amount are shown to be slightly overestimated depending on the target location and slab thickness, where F1 is affected more than B1. The signal recorded is more

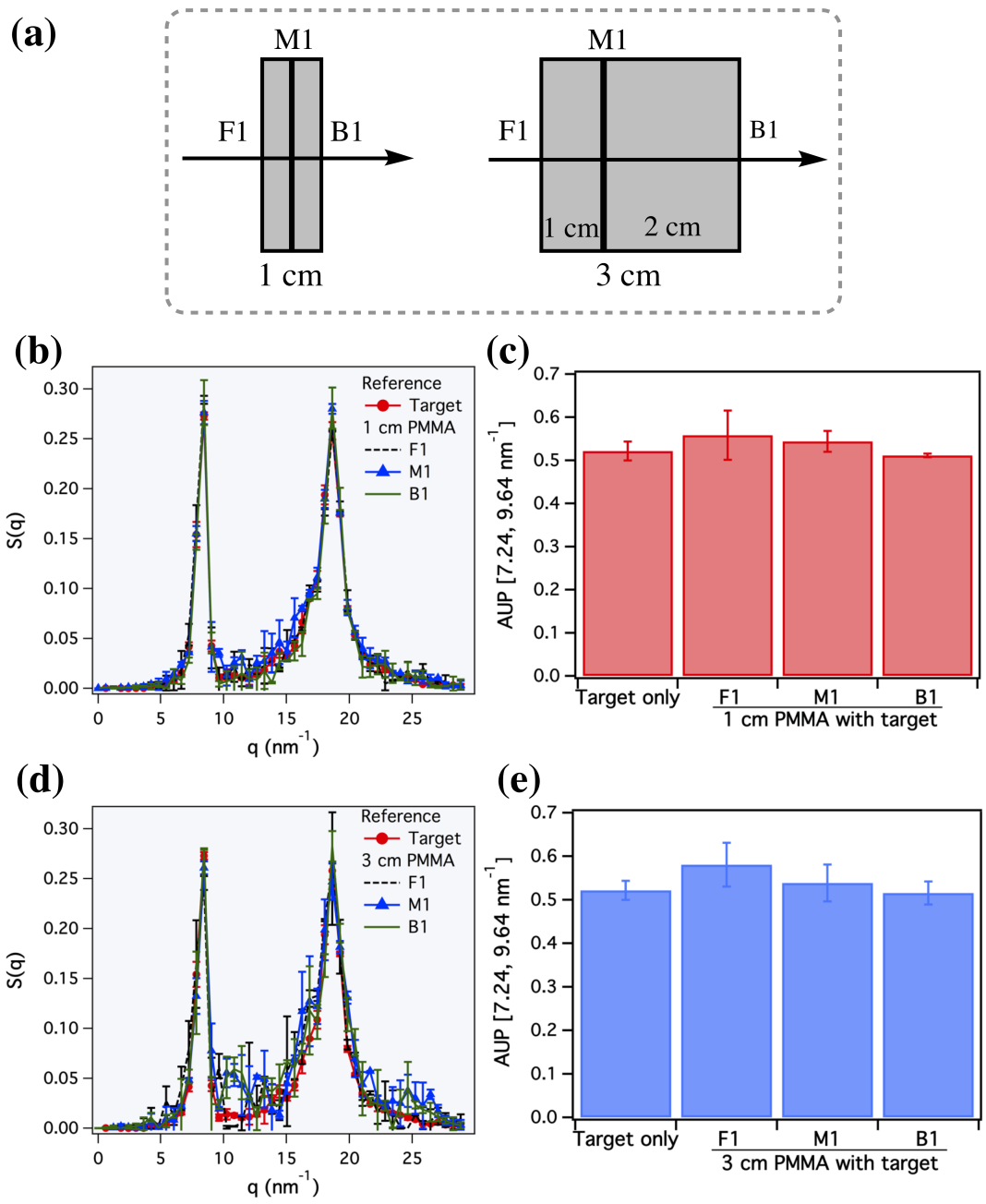


Figure 2.5: (a) Illustration of the caffeine target identification study in the objects made from PMMA slabs, where F1, M1, and B1 denote the target location. The arrow shows the x-ray beam direction. (b-c) $S(q)$ of the caffeine targets recovered from the 1 cm PMMA and their corresponding area-under-the-peak (AUP) values from 7.24 to 9.64 nm^{-1}. The caffeine target only study without any PMMA slabs was used as a reference. (d-e) $S(q)$ of the caffeine targets recovered from the 3 cm PMMA and their corresponding AUPs. Error bars represent standard deviations from two measurements at each target location.

contaminated when scattered photons need to pass through thicker PMMA slabs.

To further investigate the effect of object thickness, we analyzed the caffeine target fixed at F1 in the PMMA slabs of thickness varying from 1 to 5 cm (Fig. 2.6a). In this case, the scattered photons from caffeine need to transverse through all the PMMA slabs that are placed in front of the caffeine target before reaching the detector. Fig. 2.6b shows the scattering patterns of the 1, 3, and 5 cm PMMA with and without a caffeine target at F1. The SDD was assumed to be 183 mm for all cases based on the location of the fixed target. PMMA material is reported to have a strong scattering signal with two main peaks around 9.68 and 20.73 nm^{-1} [134]. We see similar peaks at 9.64 and 19.24 nm^{-1} for the 1 cm PMMA without a caffeine target. These peaks rise and get shifted towards the lower q region with the increase in PMMA thickness. The peak shift is due to the use of constant scattering angle across the beam in our data analysis. Despite the strong scattering from PMMA slabs with the closely matching peaks with caffeine, we notice the difference in the scattering signal between the PMMA slabs with and without a target. The scattering peaks contributed by caffeine are fixed in q-location, as indicated by the dotted line in Fig. 2.6b, but, in addition, there is a visible peak broadening effect with the increase in PMMA thickness. We can still recover the characteristic Bragg peaks of caffeine by subtracting the scattering signal contributed by the PMMA slabs alone (Fig. 2.6c). Notably, in the 5 cm PMMA study with an average transmission of 24%, the recovered scattering signal of caffeine appears noisier, along with the appearance of the secondary peaks at the background level. The results in terms of AUP are also significantly higher for the 5 cm PMMA in comparison to the 1 or 3 cm PMMA

(Fig. 2.6d). The mean AUP in the 5 cm PMMA is overestimated by about 34% as opposed to 7% and 11% in the 1 and 3 cm PMMA slabs, respectively.

The shift in the peaks of PMMA with thickness (Fig. 2.6b) is due to the use of a fixed SDD of 183 mm with reference to the target location. The shifted peaks of PMMA while identifying a target can be removed with background correction. However, its worth noting that the background correction is not always perfect, especially when the shifted peaks of PMMA start to overlap with the caffeine peaks in terms of q-location. This peak overlap is almost 100% in the 5 cm PMMA study (Fig. 2.6b). As a result, the recovered caffeine signal can be significantly contaminated by the elastic scattering from PMMA, thereby contributing to the overestimation of AUP by 34%. The peak broadening effect with PMMA thickness also exacerbates the accuracy level of AUPs. Likewise, with an imperfect background correction, the incoherent multiple scattering events from PMMA can affect the measurement, in addition to the multiple scattered photons from the caffeine. They both contribute to the rise in background scattering level with thickness.

In practice, the location of a target inside an object will most likely be unknown. One strategy to spatially locate a target inside an object (i.e., find the correct SDD) is to correlate peak position with SDD. To briefly highlight this strategy, we studied a 1 cm PMMA slab that was moved 5 cm in distance without accounting for the actual location of the PMMA. Fig. 2.7a shows the shifts in the scattering peaks of PMMA when a fixed SDD of 189 mm is used to analyze the moving PMMA slab. We observed the shift again because of our assumption of constant scattering angle across the beam for all cases in our data analysis. A simple correlation between

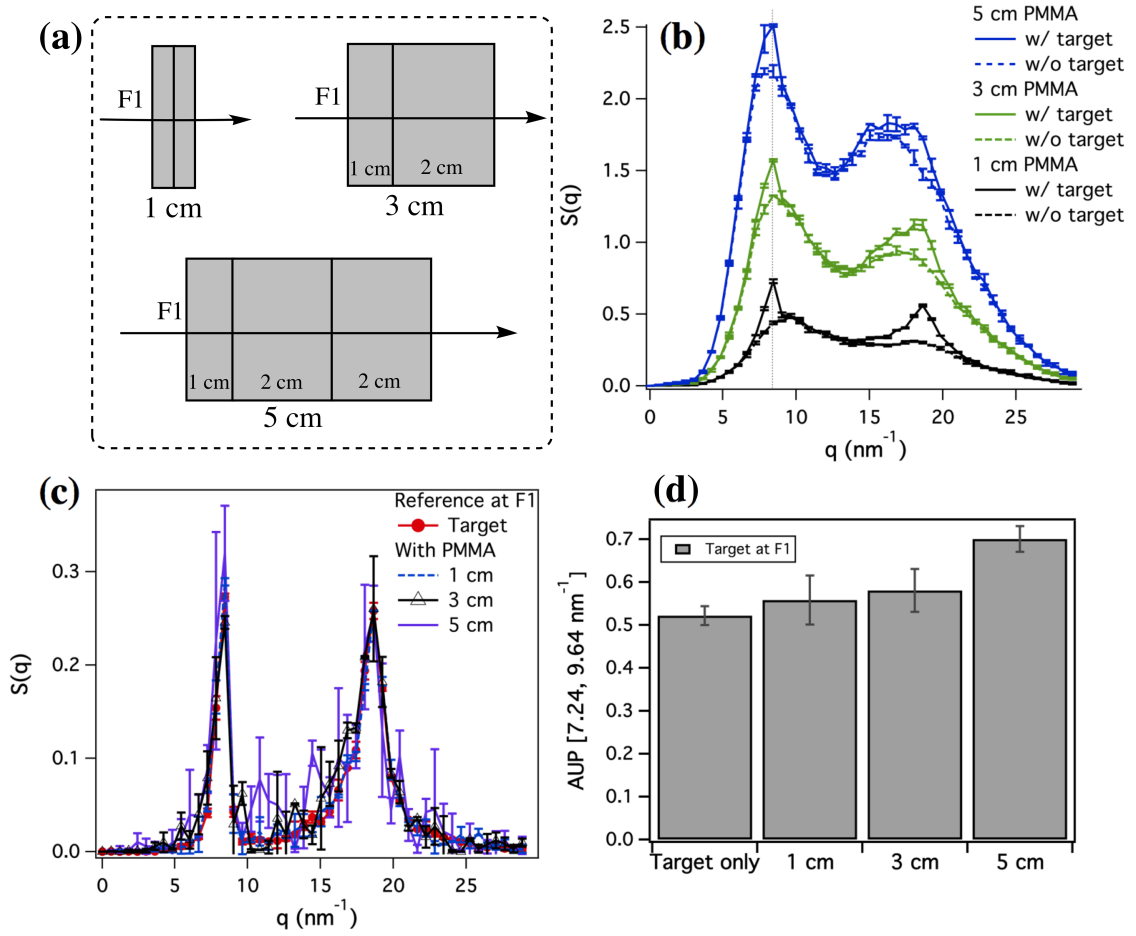


Figure 2.6: (a) Illustration of the study to investigate the effect of object thickness, where the caffeine target is fixed at F1 and the thickness of object made from PMMA slabs are varied from 1 to 5 cm. (b) $S(q)$ of the PMMA slabs with and without a caffeine target at F1. (c) Recovered $S(q)$ of the caffeine target after subtracting the scattering signal contributed by the PMMA slabs. (d) Corresponding AUP values from the recovered signal of the caffeine target in the 1, 3, and 5 cm PMMA slabs in comparison to the target alone study in a syringe. Error bars represent standard deviations from two measurements.

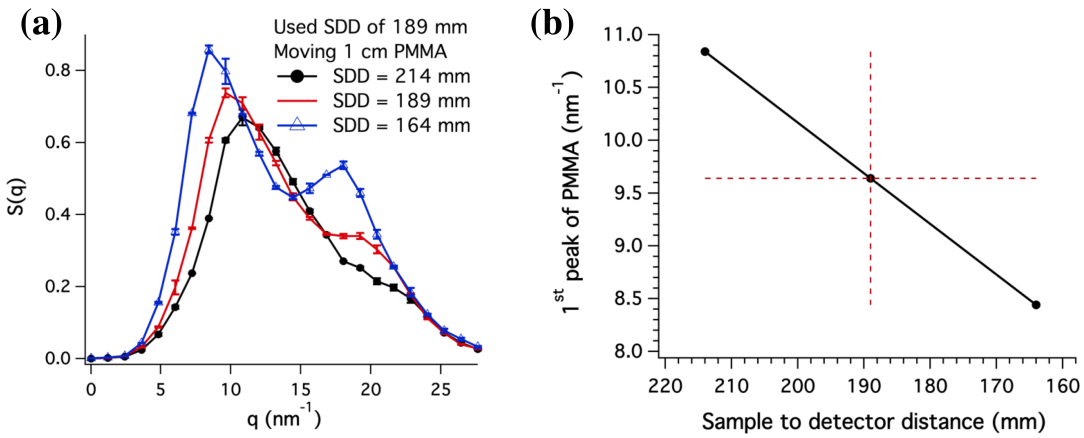


Figure 2.7: (a) Observation of the shifts in the scattering peaks of PMMA when the used SDD distance does not account for the actual location of the PMMA slab. The 1 cm PMMA slab is moved 5 cm in total distance, but the SDD for analyzing the moving PMMA is always 189 mm. (b) Correlating the shifted peak position of PMMA with the SDD.

the shifted peak position and the SDD can be established to find an unknown SDD based on the peak position information (Fig. 2.7b).

To identify a material, we need to capture its distinct scattering feature in the accessible q-range. As in our case, this scattering feature is usually the Bragg peaks. Therefore, in terms of sample requirement, the material needs to have some degree of crystallinity or repeating molecular structure in the nanometer scale. We used polycrystalline caffeine samples and solid PMMA slabs for this purpose with known d-spacing information. The peak position is related to d-space by $2\pi/d$.

2.4 Conclusion

A prototype sSAXS system was successfully built by integrating a polychromatic x-ray source and a 2D spectroscopic detector in a two-pinhole collimation setup. The system was validated by studying caffeine target in thick phantoms.

In particular, we studied caffeine as a target material in 1 to 5 cm PMMA slabs to demonstrate the capability of sSAXS technique to identify caffeine targets in all cases with 600 s measurement times. In a laboratory setup, the elastically scattered x rays at small angles were measured in 30 to 45 keV energy range, allowing to probe targets embedded in thick objects in a cm scale. The distinct Bragg peaks associated with caffeine were recovered even in the 5 cm thick PMMA with an average transmission factor of 24%. Furthermore, we found that AUPs representing the caffeine amount were slightly overestimated ($< 11\%$) due to signal contamination when the scattered photons of caffeine need to pass through 1 to 3 cm PMMA slabs. This issue was more pronounced in the 5 cm thick PMMA, where the AUP was overestimated approximately by 34%.

The measurement time can be reduced in future studies by optimizing the system collimation and the incident photons counts in 30-45 keV energy range. A laboratory-based polychromatic x-ray source with tunable voltage and current is sufficient for this purpose because of the use of a spectroscopic detector. The generated x-ray flux can be fully utilized in the energy range of interest without pre-filtering the energy spectrum. In this case, the main interest is to quickly acquire low-resolution q-data in a laboratory setup to identify embedded materials in thick objects. Alternatively, polychromatic synchrotron radiation can be utilized to reduce the measurement time and possibly do a high-resolution experiment. However, the synchrotron option is resource-intensive, and not all researchers have access to it. The sSAXS technique will be more useful in a laboratory setting.

Acknowledgments

The content of this chapter has been published in the following journal article: Dahal, E., Ghammraoui, B., and Badano, A. (2020). Characterization of materials embedded in thick objects using spectral small-angle x-ray scattering. Journal of Physics D: Applied Physics, 53(24), 245302. B.Ghammraoui helped with sSAXS instrumentation and data corrections for the spectroscopic detector.

Chapter 3: Amyloid models

The accumulation of $A\beta$ fibrils leads to the formation of β-sheet rich amyloid plaques in AD. We prepared two synthetic amyloid models with and without heating from a readily available and cheap plasma protein called bovine serum albumin. We characterized these amyloid models using a traditional SAXS as well as a prototype sSAXS system with samples in solution, brain tissue, and phantom. We found distinct scattering peaks around 6 and 13 nm^{-1} from both models that are characteristic of amyloid plaque due to its β-sheet structure. The amyloid model without heating, in particular, can be quickly prepared at scalable quantities for phantom studies to test the feasibility of using SAXS systems for amyloid detection in thick samples.

3.1 Introduction

Protein aggregation is a complex process that involves a variety of structures. The aggregation of $A\beta$ peptides into higher-order fibril structures and their accumulation in the extracellular space of the brain lead to the formation of amyloid plaques in AD. $A\beta$ fibrils are structured aggregates of thread-like shape with β-sheet conformation [135, 136]. Thus, amyloid plaques in the brain are naturally rich

in β-sheets. However, mice brain with amyloid plaques are not readily available even for an *ex vivo* study, and it is quite expensive (> \$300 per mg) to buy and use $A\beta$ peptides *in vitro* for a day to day experiment, since few mg of sample is required every time for a study. We propose to prepare and use an amyloid fibril model from bovine serum albumin (BSA) that is readily available and inexpensive (\$0.011 per mg). An amyloid model from BSA needs to mimic the known scattering pattern of amyloid plaques in AD [5, 6].

BSA is the most abundant plasma protein that can aggregate to form β-rich amyloid-like fibrils under laboratory conditions, making it an ideal amyloid model. The mechanism by which BSA monomers, despite being α-helical proteins, form β-rich amyloid-like fibrils is well understood [137–139]. Based on spectroscopic studies, BSA starts to fibrillate at elevated temperatures starting from around 60 °C, but the irreversible intermolecular β-sheets are likely to form only above 70 °C [137,140]. pH and ionic strength of the solution can be fine-tuned to control the fibrillation rate at a particular temperature [139]. Thus, under a carefully designed heat-induced aggregation condition, an amyloid model from BSA can be prepared to have stable fibrils with a reproducible structure and high β-sheet content . β-sheet content in BSA is reported to increase up to 40% upon heating [141]. Both amorphous and fibrillar aggregates of BSA have sufficient β-sheet structures similar to amyloid plaques to be used as an amyloid model.

We prepare two synthetic amyloid models with and without heating from BSA to mimic the structural characteristic of the amyloid plaques associated with AD. We used a traditional SAXS and a prototype sSAXS system with samples in

solution, brain tissue, and phantom to characterize these amyloid models. We also performed the Congo red absorbance assay for the heated solution sample to confirm the existence of fibrils with amyloid-like behavior.

3.2 Methods

3.2.1 Amyloid model preparation

Two separate amyloid models were formulated using BSA powder (Sigma Aldrich A7030-100 G), one with heating and the other without heating. The lyophilized BSA powder was crushed into a fine-grained powder to prepare the unheated model and either packed into a plastic syringe or a cylindrical phantom. The syringe was 6.4 mm thick with an inner diameter of 4.7 mm, and the cylindrical phantom was made from polymethyl methacrylate (PMMA) with a 1 cm internal diameter and 2.5 cm height.

An amyloid fibril model was prepared from BSA fibrils with heating. We also refer to as a heated model. To make BSA fibrils, pure BSA (Sigma Aldrich) was dissolved in a physiologically relevant saline buffer (10 mM phosphate, 150 mM NaCl, pH 7.4) to achieve a concentration of 5 mg/ml. After preparation, the BSA solution, referred as BSA monomers, was heated in a water bath for 1 h at 80 °C and then immediately placed into an IMC18 benchtop incubator (Thermo Scientific) set to a temperature of 23 °C. The cooled BSA solution was kept at this temperature for various periods ranging from 30 minutes to 2 months. It is important to note that new samples were independently prepared and subjected to the same heating

and cooling process for each time period at 23 °C.

3.2.2 Congo red absorbance assay

The existence of BSA fibrils with amyloid-like behavior was confirmed using a Congo red (CR) absorbance assay. 50-μl of monomeric BSA and fibrils solutions was individually added to 2-ml of buffer solution (10 mM phosphate, 150 mM NaCl, pH 7.4) with 5 μM of congo red (CR, Sigma Aldrich). Absorption spectra of CR were recorded before and after addition of the individual BSA monomer and BSA fibril samples using a Shimadzu UV-3101PC spectrophotometer. The incubation time of CR with each sample was 30 min in the dark at room temperature.

3.2.3 SAXS data collection and processing

Traditional SAXS measurements were performed using a SAXSpace instrument (Anton Paar, Ashland, VA). The instrument was configured in line collimation mode to focus a monochromatic X-ray beam of Cu K_α radiation (λ=0.154 nm). The scattered X-ray intensity, I(q), was measured as a function of the momentum transfer vector, q, where $q = 4\pi \sin\theta/\lambda$ with 2θ being the scattering angle and λ being the X-ray wavelength. We initially focused on a q range from 0.1 to 1.66 nm^{-1} and later increased our q_{max} to 16.5 nm^{-1}. The scattering pattern was recorded by a CCD camera with a pixel pitch of 24 μm in an array of 2084 x 2084 pixels. 32 μl sample was loaded in a 1-mm-diameter quartz microcapillary and placed in the temperature-controlled sample holder (TCStage 150, Anton Paar) at a distance of

305.3 mm from the CCD. All measurements were made in an air-evacuated space at a pressure below 1.6 mbar and at a constant sample temperature of 23 °C. For each measurement, 200 frames were collected at 5 s exposures and averaged to get raw SAXS 1D scattering intensities, $I(q)_{raw}$. $I(q)_{raw}$ data were corrected for background scattering and dark current. An Indirect Fourier Transformation (IFT) method was used to de-smear the data as well as to obtain the pair-distance distribution function, $P(r)$ [80].

The scattering intensity of the sample after correction, $I(q)_{sample}$, was calibrated to absolute scale using the cross section of water as in Eq. 3.1 [142],

$$I(q) = \frac{I(q)_{sample}}{I(0)_{water}} \frac{d\sum}{d\Omega_{water}}, \tag{3.1}$$

where $I(0)_{water}$ is the scattering intensity of water at $q = 0$ and $d\sum/d\Omega_{water} = 0.01632$ cm^{-1} is the constant differential scattering cross section of water at 293 K.

When experimental $I(q)$ represents particle form factor, $P(r)$ is theoretically the IFT of $I(q)$ as shown by Eq.3.2. $P(r)$ curve contains the shape and dimension information of the scattering particle present in a solution.

$$P(r) = \frac{r}{2\pi^2} \int_0^\infty q^2 I(q) \frac{\sin(qr)}{qr} dq \tag{3.2}$$

Since experimental $I(q)$ only covers the small q range, $P(r)$ can be indirectly calculated based on the IFT method introduced by Glatter [80] as implemented in the GIFT (Generalized Indirect Fourier Transformation) program. The $P(r)$ function

was approximated by a set of N cubic B-splines, $\phi_v(r)$, in a linear combination with pre-factors c_v, given by $P(r) = \sum_{v=1}^{N} c_v \phi_v(r)$. At least 20 or D_{max} number of splines was used to get the $P(r)$ using this IFT method. D_{max} is the a priori estimate of the maximum dimension of the particle. For each data set, D_{max} was adjusted until the $P(r)$ did not strongly oscillate, become negative or descend sharply. Furthermore, the low-resolution bead models of BSA fibrils were generated using the *ab initio* shape determination program called DAMMIF [4] from the ATSAS software package [143]. 10 models were generated from DAMMIF. They were all averaged and filtered using DAMAVER leading to the final model. No symmetry restriction was imposed.

3.2.4 sSAXS measurements

Preliminary sSAXS measurements were acquired using the validated prototype system, as presented in Fig. 2.1. Data from this particular section was published by Breedlove et al. [144]. Two lead pinholes of 2.5 and 0.5 mm diameter were used to collimate a polychromatic x-ray beam from a tungsten source (50 kVp and 1 mA). A HEXITEC detector (Quantum Detectors Ltd) of 80 x 80 pixels made from 1 mm thick cadmium telluride crystal was used to measure the position and energy of the scattered photons in each pixel. The sample to detector distance (SDD) was 214 mm. Data were collected for 600 and 1800 s for the syringe study and 1200 s for the phantom study and analyzed in terms of the momentum transfer q. The accessible q-range was from 1.3 to 28 nm^{-1}. Q-data from 30 to 45 keV was summed

for all energy bins to obtain counts as a function of q, $C(q)$. The binning step was 1.2 nm^{-1}. The background correction was done on the summed q-data to remove background scattering.

3.3 Results and discussions

An amyloid fibril model was prepared from a BSA solution using a heat-induced aggregation process. The preparation method is illustrated in Fig 3.1A. Heating BSA above 70 °C in a buffer, high in salt concentration, followed by cooling over several hours at fixed temperature is a viable approach to irreversibly produce BSA fibrils [137, 140]. For each time period at 23 °C, SAXS measurements were performed using a line-collimated setup (Fig 3.1B). In this set-up, the scattering

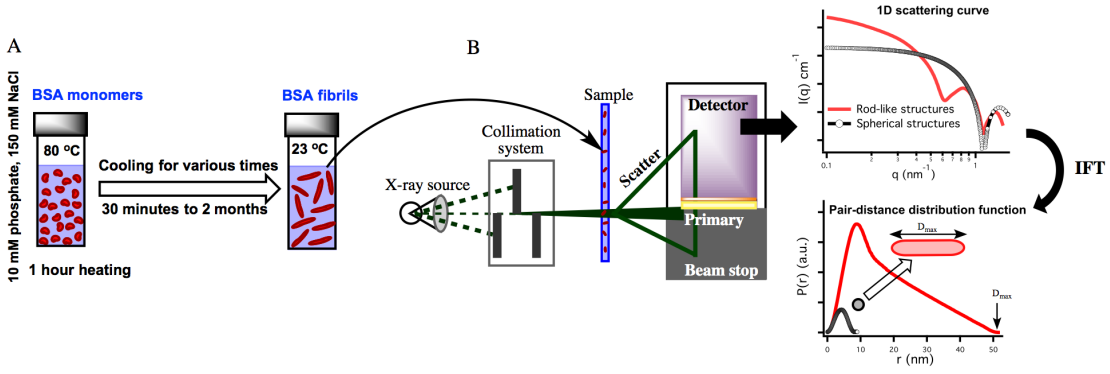


Figure 3.1: Schematic of A) a method to prepare an amyloid fibril model with heating from BSA B) SAXS set-up for measurements with illustration of distinct scattering curves, $I(q)$, for rod-like and spherical structures that would be theoretically acquired. Indirect Fourier transformation (IFT) of $I(q)$ would result in structure sensitive pair-distance distribution function, $P(r)$, in real space.

curves $I(q)$ were acquired followed by the IFT of $I(q)$ to get the pair-distance distribution function, $P(r)$ in real space. Simulated results are shown in Fig 3.1B.

to illustrate this approach. Knowledge of particle geometry is not required beside guessing its maximum dimension (D_{max}) to extract the structural information by the IFT method [76, 90]. The structural evaluation of BSA fibrils (an amyloid fibril model) in solution is based on the use of this technique.

3.3.1 Congo red absorbance assay

While concurrently doing SAXS study, the existence of fibrils with amyloid-like behavior in our model system was confirmed using a Congo red (CR) absorbance assay. CR is a commonly used amyloid-specific dye for amyloid detection [145–147]. Its specificity is due to high-affinity binding to the β-sheets of amyloids fibrils [148]. Upon binding, the absorbance of CR increases with a characteristic red shift from about 490 nm to 540 nm [147, 149]. Absorbance spectra of CR were recorded before and after separately adding the BSA monomers and fibrils.

As shown in Fig. 3.2A, there is an increase in the absorbance of CR with BSA fibrils (30-min old) accompanied by a red shift in the spectrum when compared to the spectra of CR or CR with BSA monomers. The absorbance of the BSA fibrils alone does not contribute to the spectral changes. The observed red shift is consistent with the behavior of traditional $A\beta$ as well as BSA fibrils [138, 150]. Moreover, the spectra of CR do not change further whether CR is incubated with BSA fibrils freshly prepared (30 min cooling time) or left to mature for 2 months (Fig. 3.2B), suggesting that BSA fibrils have similar amyloid-like behavior irrespective of time. This result suggests no significant increase in β-structure of BSA fibrils after cooling at room

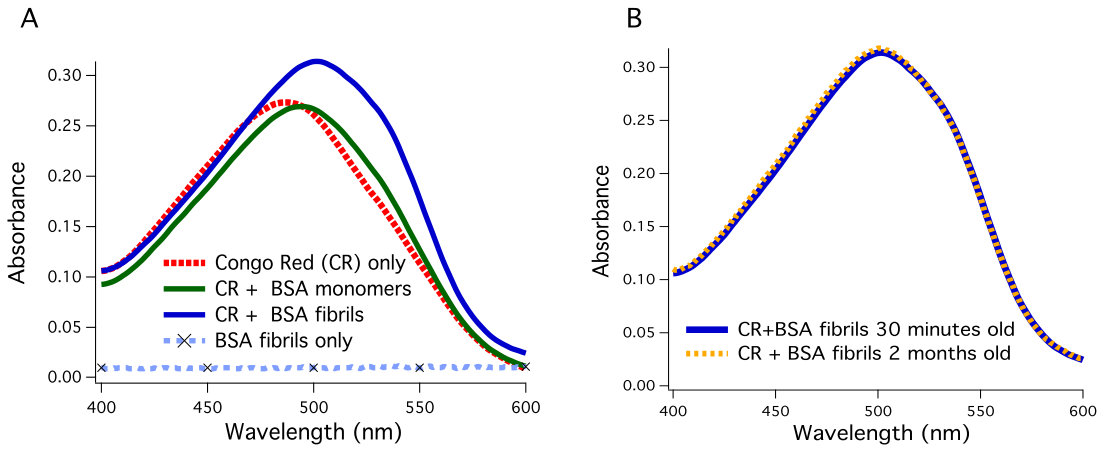


Figure 3.2: UV-Vis spectra of 5 μM Congo red (CR): A) with freshly prepared BSA monomers and 30-min old BSA fibrils and B) with 30-min and 2-month old BSA fibrils. The spectra of CR and BSA fibrils alone are shown for reference.

temperature from 30 minutes to 2 month. Most of the changes in the secondary structure likely occur immediately after heating.

3.3.2 SAXS characterization

Solution SAXS of an amyloid fibril model: In this study, our q-range was from 0.1 to 1.66 nm^{-1}. Fig. 3.3 shows BSA fibrils prepared from 5 mg/ml of BSA monomers characterized using SAXS for various time periods from 30 min to 2 months. 32 μl sample was taken from the stock solution each time for analysis in order to capture the change in fibril structures with time. Since a dilute protein solution was used, the experimentally acquired $I(q)$ strongly represented the form factor of protein structures present in solution [151, 152]. Fig. 3.3A shows the $I(q)$ curves on the log-log scale where the experimental scattering data (open circles) are fitted with theoretical curves using the IFT method. The results show strong q dependence. In comparison to BSA monomers, the scattering intensity at the low q

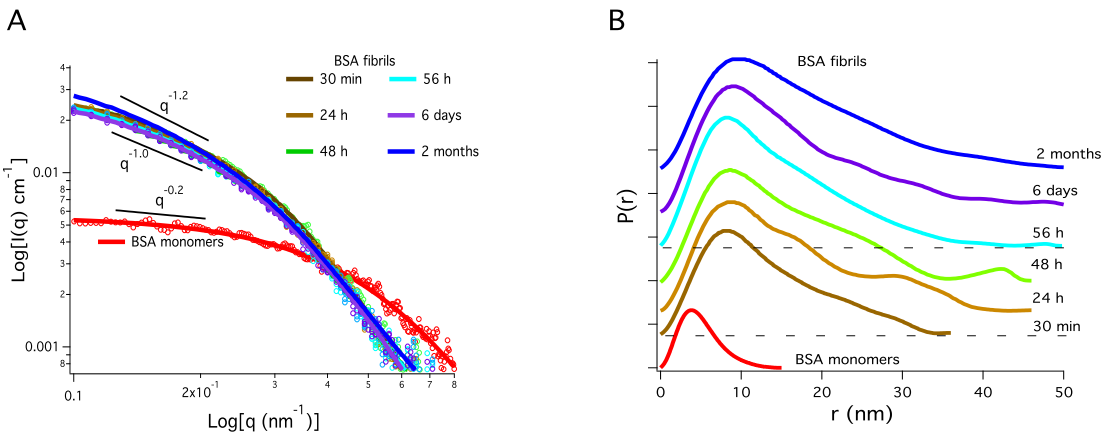


Figure 3.3: SAXS characterization of BSA fibrils for time periods of 30 min to 2 months using the IFT method. (A) SAXS signals, $I(q)$ in absolute scale, with IFT fits of experimental data (open circles). (B) Pair-distance distribution function, $P(r)$, resulting from IFT fits. The offset in $P(r)$ for various times is for visual clarity.

values (< 0.2 nm^{-1}) increases with the formation of fibrils at all time periods suggesting larger aggregates of higher molecular weight. At high q values (> 0.5 nm^{-1}), noise increases for fibrils due to significant consumption of small-sized monomers in the fibrillation process. Nevertheless, the experimental SAXS signals for all fibrils have distinct features in the low-q region showing consistency with the predicted results shown in Fig. 3.1B. However, minima are not detectable in the high q region of the experimental $I(q)$ due to the low signal to noise ratio at high q values.

The change in the slope of $I(q)$ for fibrils in the low-q region is clear in the double logarithmic plot shown in Fig. 3.3A. The slope represents the exponent, α, from a power law approximation to $I(q)$ as directly proportional to $\mathrm{q}^{-\alpha}$. Monomers approximately show a q^0 scattering behavior typical of spherical-like geometries [77] consistent with reports describing BSA by the form factor of an in SAXS experiments [142] or the heart-shaped structure in crystallography data [153]. Meanwhile,

the fibrils obtained from 30 min to 6 days consistently follow a q^{-1} trend. Such a scattering behavior is the signature of a rod-like structure [154]. Interestingly, even for fibrils as old as 2 months, they exhibit approximately the same trend, thereby suggesting that BSA fibrils in solution maintain a rod-like elongated structure for an extended period of 2 months time.

The above observation is supported by the model-free analysis of $P(r)$ curves obtained from the IFT method. Fig. 3.3B shows the $P(r)$ curves of fibrils corresponding to the IFT fits of the experimental data presented in figure Fig. 3.3A. BSA monomers represent spherical-like particles. However, because of their ellipsoidal shape, monomers do not show a bell-shaped $P(r)$ curve as shown in the simulated results for spherical particles (Fig. 3.1B). All fibril samples, on the other hand, have $P(r)$ curves with pronounced extended tails that are characteristic of elongated rod-like particles. The trends in the $P(r)$ curves are similar to what is theoretically predicted for rod-like structures in Fig. 3.1B. The broad $P(r)$ peaks are due to the larger cross-sectional diameters of fibrils. Our results clearly show that fibrils are formed within 30 minutes of cooling, where the D_{max} increases at least by 2.5-fold relative to that of BSA monomers. The propensity of heated BSA to form fibrils within a cooling time as short as 30 min has been inferred, primarily through fluorescence measurements [138–140].

Furthermore, when compared to monomers, we observe a steady shift of the peak corresponding to BSA fibrils and an increase in D_{max} with time. This suggests that the length of the fibrils grows significantly with time but not their cross-sectional diameters when cooled to room temperature. The secondary peaks around

30 and 43 nm of the 24 and 48 h $P(r)$ curves respectively (Fig. 3.3B) can be attributed to the presence of larger aggregates at very low concentrations. Since these larger aggregates are not the dominant species in the solution, there is no abrupt rise in their scattering intensities at q=0. After 56 h, the larger aggregates disappear by coalescing with fibrils and forming stable structures with an estimated D_{max} of approximately 50 nm. The $P(r)$ curves also indicate that the fibrils maintain their rod-like structure during the course of the 2-month experimental study.

A detailed characterization of BSA fibrils serving as an amyloid model with heating has been performed using SAXS. Apart from evaluating the structures of fibrils, SAXS characterization becomes important for detecting fibrils under disease conditions. As proof-of-concept, we now show the use of the distinct BSA fibril SAXS signals to recover their volume fractions in the mixture solutions of monomers and fibrils. Ideally, any SAXS signals from mature BSA fibrils (>56 h) can be used for this purpose because they consistently show q^{-1} scattering behavior and have P(r) curves characteristic of stable rod-like structures (see figure Fig. 3.3). SAXS signals of 2-month old fibrils were used to estimate the volume fraction of fibrils. 2-months-old fibrils were used to prepare samples consisting of volume fractions of fibrils ranging from 0 (monomers only) to 1 (fibrils only). SAXS signals were acquired for each sample.

As shown in Fig. 3.4A, the scattering intensity at low q increases as volume fractions of fibrils goes to 1 indicating presence of larger aggregates as fibrils are added. The corresponding model-free $P(r)$ curves clearly show the presence of two types of structures in the solution. It is indicated in Fig. 3.4B by the presence

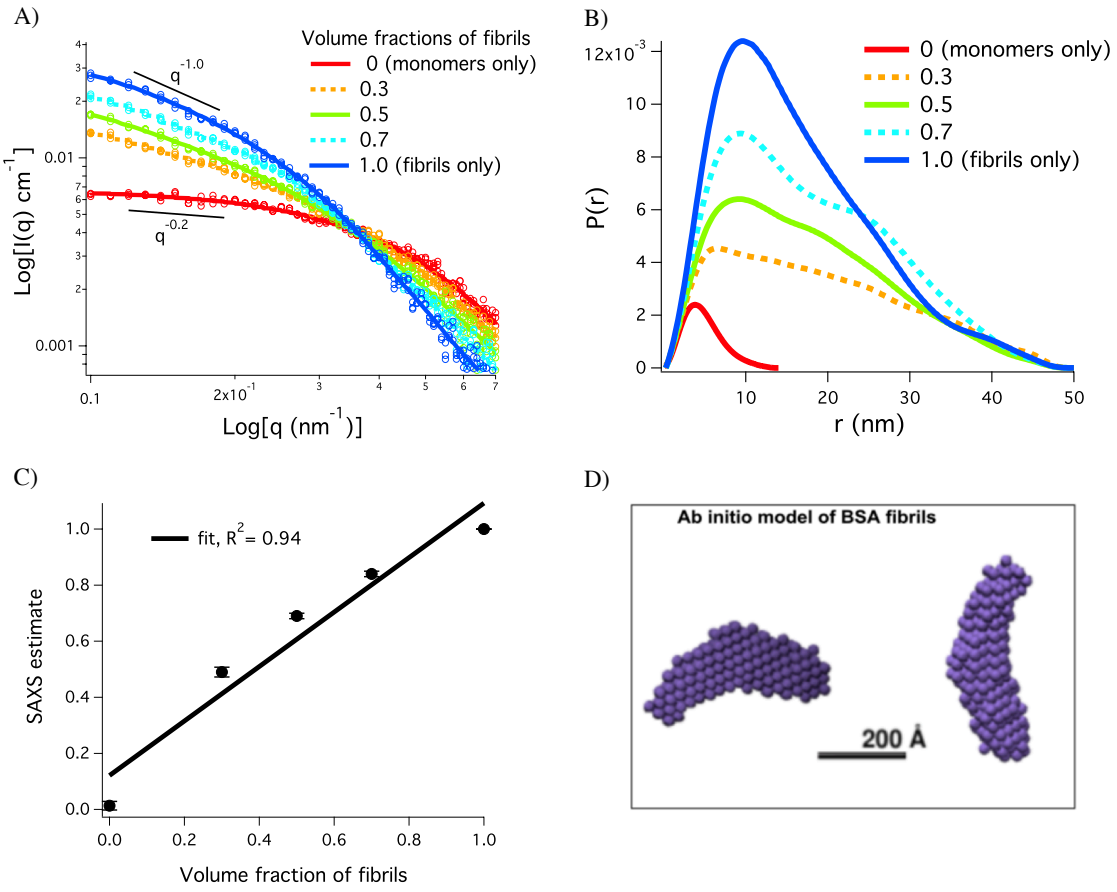


Figure 3.4: SAXS characterization of the mixture solutions of fibrils and monomers along with the volume fraction estimates. (A) Representative $I(q)$ curves in absolute scale for the solution with 0, 0.3, 0.5, 0.7, and 1.0 volume fractions of fibrils. (B) Corresponding $P(r)$ curves generated from the IFT fits of the experimental data. (C) SAXS estimate of the volume fraction of fibrils relative to the true value. Small error bar represents the standard deviation in the SAXS estimates from the three independent experiments. (D) Low-resolution bead models of BSA fibrils generated by using the ab initio shape determination program [4]. Two different views are shown.

of shoulder or bump on the ride hand side of the $P(r)$ curves in reference to the major peak around 9 nm. This shoulder or bump becomes more pronounced with increase in the volume fraction of fibrils. However, these observable changes in $P(r)$ are not necessarily due to the presence of monomers and fibrils as two separate non-interacting structures in the solution. At this point, we know that the fibrils and monomers do not interact significantly to form a single aggregated complex. However, it is not certain up to what extent fibrils and monomers interact with each other in solution. The interaction is not kinetically inhibited because monomers are the building block of fibrils and "stable" fibrils can always grow slightly by consuming the excess monomer with time. Therefore, stable fibrils that we used in this study tend to be metastable.

Despite the possible interaction effect, the distinct SAXS signals of fibrils were exploited to quantify their volume fractions in the mixture solutions of monomers and fibrils. The overall scattering intensity, $I(q)_{total}$, of the two-species system is the sum of the individual intensities $I(q)_1$ and $I(q)_2$, weighted by their volume fractions. Therefore, the volume fractions of fibrils were obtained by fitting the experimental data with the pre-determined SAXS signals of BSA fibrils, $I(q)_1$, and monomers, $I(q)_2$ alone. Fig. 3.4C depicts a strong linear correlation between the volume fractions estimated by SAXS and the actual fibrils volume fractions. The small deviation in the estimated SAXS volume fractions can be explained considering the interaction effects mentioned above. Overall, the volume fractions of the fibrils have been correctly determined in the mixture solutions of two species by leveraging the distinct SAXS signal from the structurally stable fibrils. BSA fibrils are easily

detectable. This approach can be extended towards the in vitro detection of amyloid fibrils as long as the SAXS signals of amyloid fibrils are well characterized and distinct.

To know more about the detail shape representative of fibrils, the ab initio shape determination program called DAMMIF [4] was used to produce the low-resolution bead model as shown in Fig. 3.4D. Ab initio results show that BSA fibrils still have elongated structures with slightly bent curvature. It should be noted that the theoretical scattering curve of each bead models, that is used to generate a final model, fits well with the experiment data of BSA fibrils in both low and high-q regions. 10 models were generated from DAMMIF with the mean NSD of 0.828 $\pm$ 0.041. They were all averaged leading to the final model.

SAXS of a solid amyloid plaque model: In this study, our q-range was from 1.5 to 16.5 nm^{-1}. A heated solution of BSA fibrils (> 2-months old) was centrifuged and the semi-solid fibrils pellet (approx. 5 mg) thus obtained was deposited on a solid sample holder window enclosed by scotch tape for SAXS measurements. The resulting pellet dried in vacuum represents a solid amyloid plaque only model made from BSA fibrils. The SAXS instrument was configured in point collimation mode with beam spot size of 250 μm. For each measurement, 30 frames were collected at 300 s exposures with sample to detector distance (SDD) of 110.2 mm. As shown in Fig. 3.5a, SAXS measurements of amyloid plaque model show 2D scattering pattern typical of $A\beta$ fibrils and plaques in AD [5,6]. The scattering with peaks at q = 6.4 and q = 13.4 nm^{-1} is due to the β-sheet structure of fibrils (Fig. 3.5b). The peak at 13.4 nm^{-1} is not fully resolved with the flat signal beyond 13.4 nm^{-1}. This is

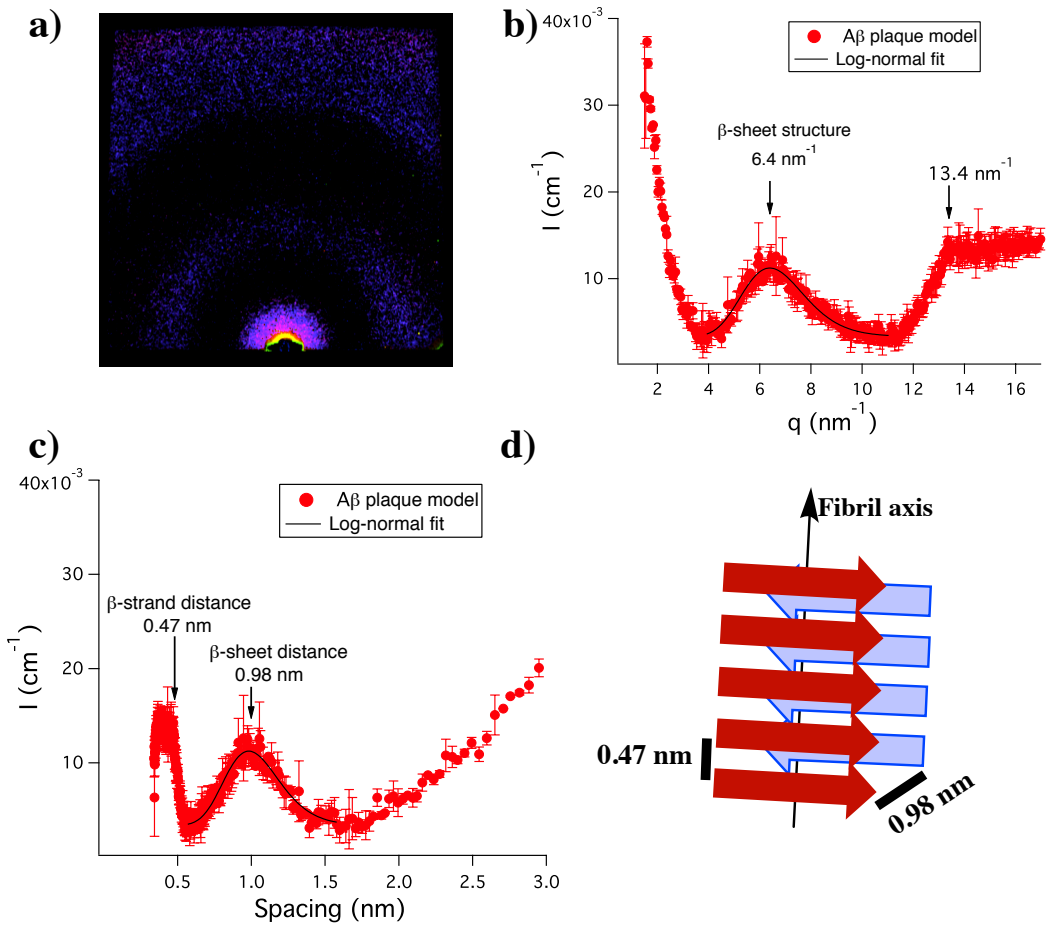


Figure 3.5: SAXS measurements of amyloid plaque model made from BSA fibrils showing A) 2D scattering pattern typical of AD associated $A\beta$ fibrils and plaque structures [5, 6], B) Radially averaged 1D scattering pattern in inverse space with distinct peaks at 6.4 nm^{-1} and 13.4 nm^{-1} from β-sheet structure, where error bar represents a standard deviation in data from two independently prepared samples, C) 1D scattering pattern in terms of Bragg spacing with $q = 2\pi/d$, and D) schematic representation of β-sheet structure of $A\beta$ fibrils based on the SAXS data presented in C). The peak at 0.47 nm is the repeat distance between β-strands and the peak at 0.98 nm is the repeat distance between β-sheets. Each arrow represents a β-strand and the two colors represent β-sheets. Similar structural features are reported to be found in human brain tissue with AD [5].

.

because the scattering events above 13.4 nm^{-1} with SDD of 110.2 mm are recorded at the edge of the detector due to its limited size. There is usually a broad peak in the region above 13.4 nm^{-1} due to the presence of water and lipids [126]. The ability to use a larger detector or decrease sample to detector distance further to cover the q range between 2 to 25 nm^{-1} would resolve this issue. Nevertheless, based on the β-sheet structure of fibril, the peak at q = 6.4 nm^{-1} corresponds to the repeating β-sheet distance of 0.98 nm and the peak around q= 13.4 nm^{-1} corresponds to the repeating inter-strand distance of 0.47 nm (Fig. 3.5c and d). Log-normal fit was done from 3.9 to 11.1 nm^{-1} to extract the peak value representing beta-sheet distance. All these exact structural features are recently reported to be found in the human brain tissue with AD [5]. The results show that SAXS is capable of detecting pure $A\beta$ plaques without any contrast agent due to its scattering peaks from β-sheet structure. It also suggests that we can use this amyloid plaque model as a substitute for real AD associated plaques to explore the SAXS application of amyloid imaging in the instrument development phase.

SAXS of brain tissue with and without amyloid plaque model: The semi-solid BSA fibrils pellet were deposited on a 1-mm thick mouse brain slice and slowly dried in vacuum to artificially obtain brain with solid plaque sample. 1x plaques sample were prepared by depositing 1.6 mg of fibrils (dried weight) in roughly 2 mm x 2 mm area of the 1-mm thick brain slice, thereby approximately yielding 0.4 mg/mm^3 of plaque density. Similarly, the plaque density in the brain slice with 2x plaques was approximately 0.8 mg/mm^3. 2x plaques were achieved by adding 1.6 mg of fibril pellet on the brain slice with 1x plaques after collecting the SAXS data. SAXS

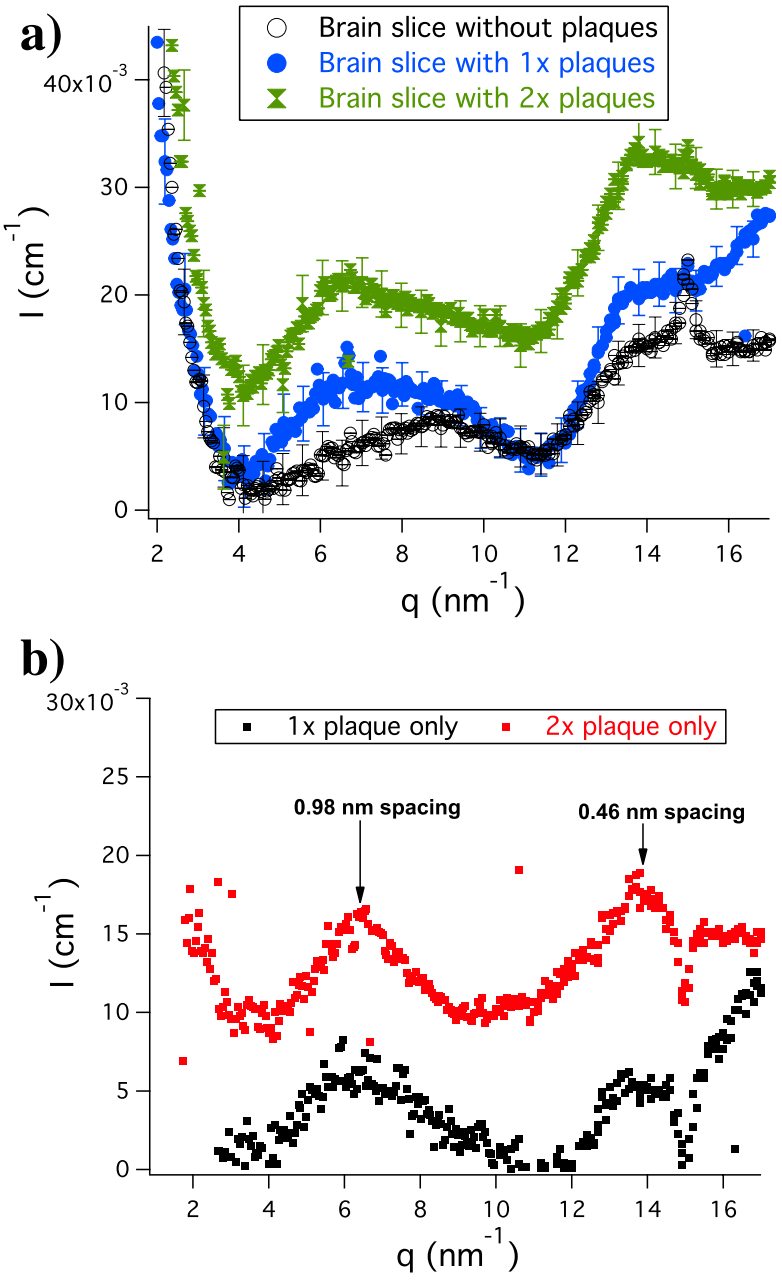


Figure 3.6: SAXS measurements of amyloid plaque model deposited on brain tissues. a) Radially averaged 1D scattering data of brain slice without plaques, with 1x plaques ($\sim$ 0.4 mg/mm^3), and with 2x plaques ($\sim$ 0.8 mg/mm^3) in absolute scale. Error bars are standard deviation in the intensity values of pixels per q bin and are shown every 10 points for clarity. b) Scattering profile of 1x and 2x plaques after subtracting 1D SAXS data of brain slice with plaques from without plaques.

measurement settings used for the amyloid plaque model deposited on brain tissues were same as the amyloid plaque only model, where 30 frames were collected at 300 s exposures and SDD of 110.2 mm for each measurement.

For the brain slices with 1x and 2x plaques, SAXS data presented in Fig. 3.6a shows proportionally increasing peaks in terms of absolute intensity values at q = 6.4 and q = 13.4 nm^{-1}. It is consistent with the features of pure plaque model data presented in Fig. 3.5 with additional background scattering from the brain tissue. The scattering peaks from the β-sheet structure of plaques are still distinct in the presence of scattering from the brain tissue. This has also been reported in the x-ray diffraction studies of the human brain tissue with and without AD [5]. Additionally, the scattering from the brain tissue can be subtracted from the plaque data to recover scattering peaks only due to 0.98 and 0.46 nm spacing in the β-sheet structure (Fig. 3.6b).

3.3.3 Preliminary sSAXS characterization of amyloids in phantoms

As illustrated in Fig. 3.7a, we prepared two different amyloid models from BSA powder, one with heating and another without heating. In this sSAXS study, we focused on studying solid sample on thick phantoms and detecting characteristic amyloid signal. The solution sample did not provide a strong signal. The dried samples were crushed into powder to fill syringes (6.4 mm thick) for sSAXS measurements (Fig. 3.7b). The sSAXS setup is presented in Fig. 3.7c. The packing density of the BSA powder was around 677 mg/cm^3. The cylindrical PMMA phantom was

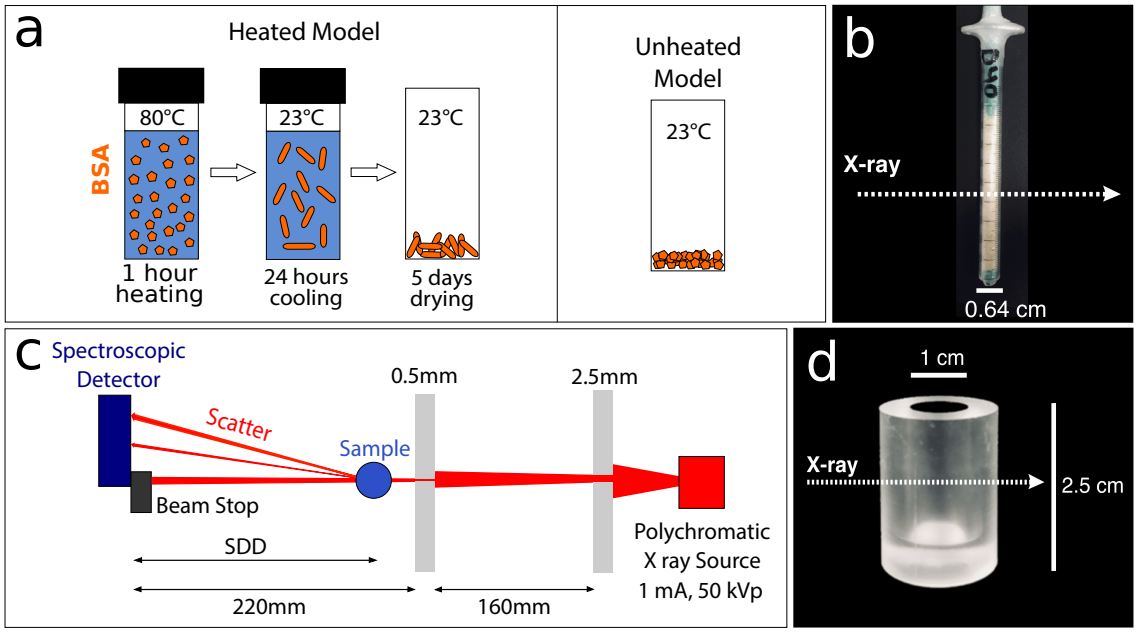


Figure 3.7: (a) Schematic of amyloid model preparation, heated (left) and unheated (right). (b) Syringe sample of an amyloid model. (c) sSAXS system setup. (d) Dimensions of the cylindrical PMMA phantom.

2 mm thick with a 1 cm internal diameter and 2.5 cm height (Fig. 3.7d).

Syringe samples: Results of the syringe study for both the heated and unheated amyloid models show easily distinguishable scattering peaks around 6 and 13 nm^{-1} (Fig. 3.8), corresponding to the characteristic peaks of Aβ plaques or fibrils resulting from their cross-β structure [5, 6]. The peak around 6 nm^{-1} corresponds to the β-sheet spacing and the peak around 13 nm^{-1} corresponds to the β-strand spacing. 600 s data acquisition time was sufficient to identify these peaks in both models. In the heated amyloid model, the initial BSA solution concentration can be changed to increase or decrease the strength of the scattering peaks from β-sheets (Fig. 3.8b). However, there is high uncertainty in measuring those peaks for the 20 mg/ml sample. The unheated amyloid model showed slightly sharper peaks around 6 and 13 nm^{-1} (Fig. 3.8c). Its background-corrected 2D scattering pattern is shown

in Fig. 3.8d.

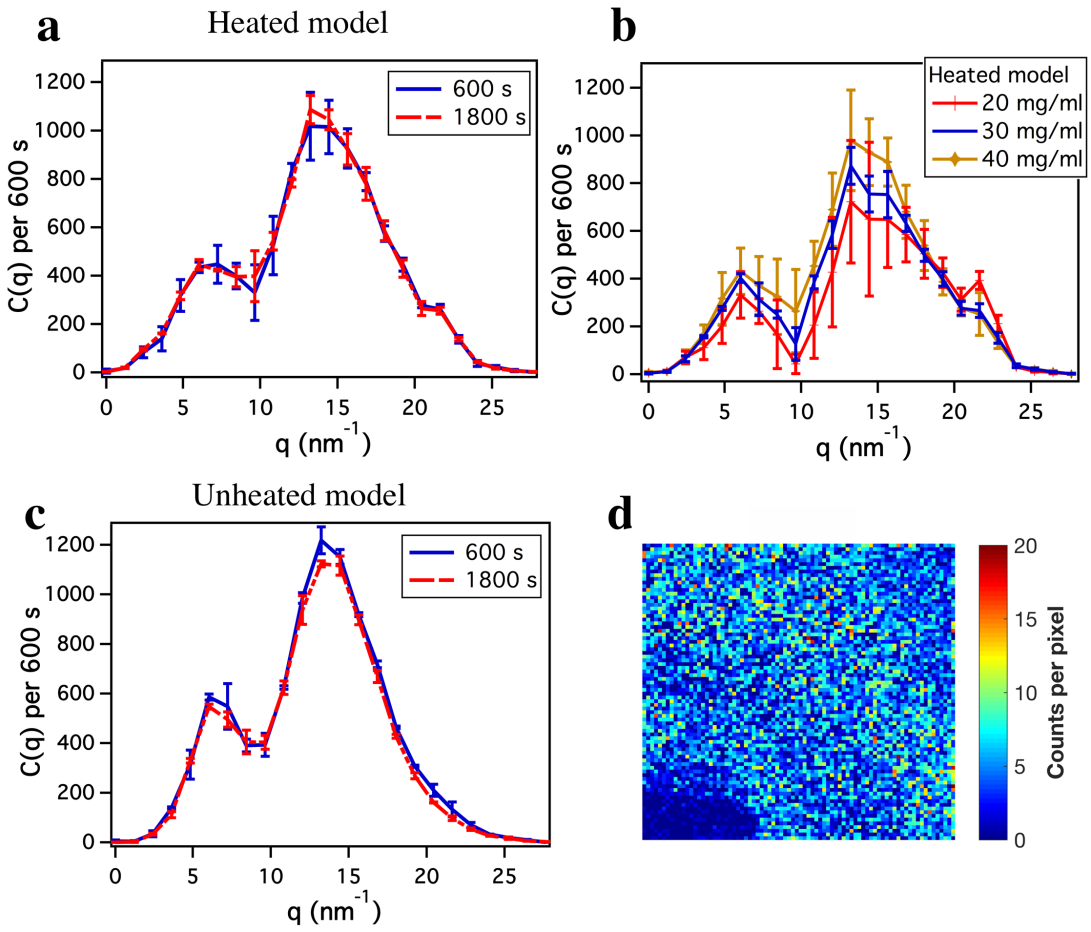


Figure 3.8: Characterization of the heated and unheated amyloid models in a syringe. (a) Scattering signal of the heated model using 600 and 1800 s data acquisition times. (b) Effect of BSA concentration in the scattering signal of the heated model. Error bar represents standard deviations from n=3 measurements. (c) Scattering signal of the unheated model for 600 and 1800 s from n=2 measurements. (d) Representative 2D detector data of the unheated model in 30 to 45 keV energy range

Phantom sample: We then used sSAXS to characterize our amyloid models in the 2 cm thick PMMA phantom. This is relevant for the purpose of evaluating the performance of the detection technique through thick samples. We found that the heated model did not provide sufficient β-sheet signal to be reliably used in the phantom study. Therefore, Fig. 3.9 shows the results only for the phantom with an

unheated amyloid model. The unheated model provided sufficient scattering signal after background correction (Fig. 3.9c), and peaks were identifiable around 6 and 14 nm^{-1} (Fig. 3.9e). The beta-sheet content in the lyophilized BSA is approximately 25% [155]. It should be noted that the peaks were recovered without accounting for the attenuation effect. Also, as reported before [91], PMMA alone has a strong scattering peak around 9.64 nm^{-1} (Fig. 3.9d).

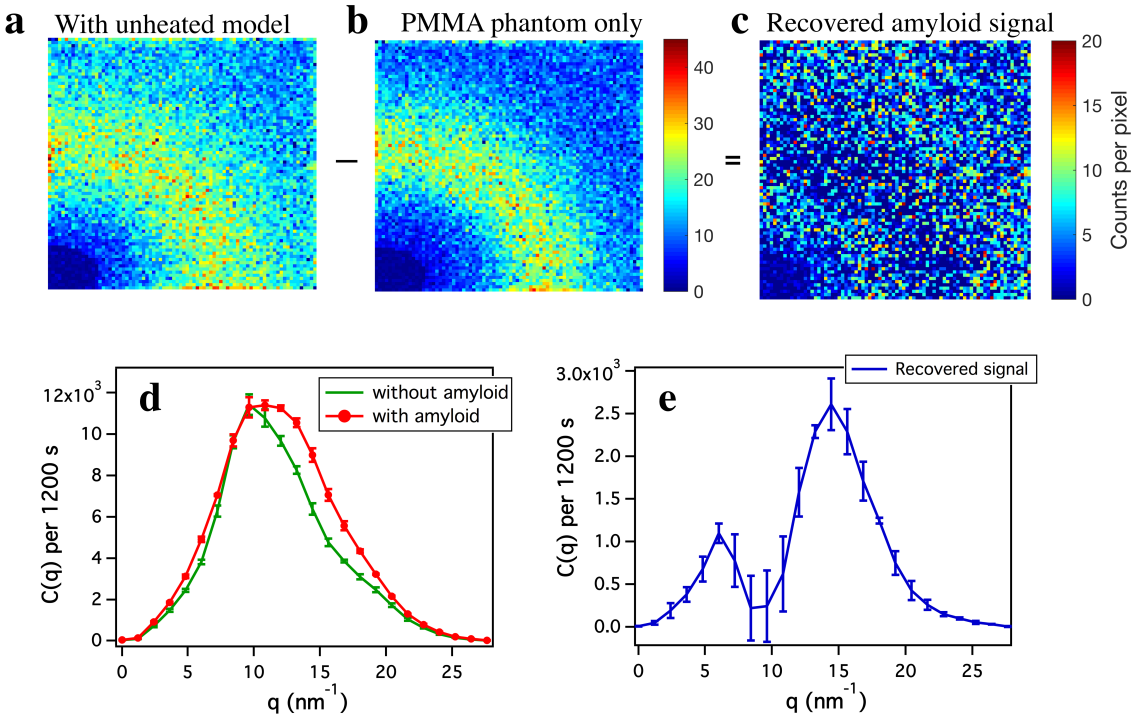


Figure 3.9: Characterization of the unheated amyloid model in a cylindrical PMMA phantom. (a–c) 2D detector data before and after background subtraction, (d) Scattering signal from the PMMA phantom with and without the unheated amyloid model. (e) Recovered scattering peaks associated with amyloids after background subtraction. Error bar represents standard deviations from n=3 measurements.

3.4 Conclusion

Both the heated and unheated amyloid models mimic the cross-β structure of amyloid plaques in AD. The heated amyloid model is primarily useful in estimation tasks in thin (< 1 cm) tissue-mimicking phantoms. High concentration of BSA ($>$ 20 mg/ml) was required to prepare the heated amyloid model in order to decrease the uncertainty in measuring the characteristic β-sheet peaks. The heated BSA solution at high concentration forms β-sheet rich structures in the gel state. The unheated amyloid model, on the other hand, is useful for evaluating and calibrating an x-ray scattering prototype when detecting β-sheet structure through thick phantoms beyond 1 cm. The unheated model is less time consuming to prepare and represents amorphous aggregates of BSA and has sharper and more detectable β-sheet scattering signal through thick phantoms.

Acknowledgments

The content of this chapter has been published in the following journal articles: SAXS section was adapted from Dahal, E., Choi, M., Alam, N., Bhirde, A. A., Beaucage, S. L., & Badano, A. (2017). Structural evaluation of an amyloid fibril model using small-angle x-ray scattering. Physical biology, 14(4), 046001. All work in this chapter related to SAXS and amyloid model was done by E. Dahal.

sSAXS section was adapted from Breedlove, S., Crentsil, J., Dahal, E., & Badano, A. (2020). Small-angle X-ray scattering characterization of a β-amyloid

model in phantoms. BMC Research Notes, 13(1), 1-5. S. Breedlove and J. Crentsil performed sSAXS measurements and data analysis as part of the summer REU program. Fig. 3.7 was made by S. Breedlove with E. Dahal input and editing.

Chapter 4: Characterization of amyloid-like targets in a mouse head with skull

As reported in the previous chapter, we initially spent some time developing an amyloid model having similar scattering patterns as amyloid plaques in AD. In this chapter, we use that validated amyloid model (unheated) to make amyloid-like targets and study the feasibility of developing a label-free method to estimate brain amyloid loads in mice using spectral small-angle x-ray scattering (sSAXS). We present results for estimating amyloid load in a fixed mouse head with skull by recovering the characteristic scattering signal from the amyloid target situated at various locations. The method records and analyzes the x rays elastically scattered from the β-sheets of amyloid plaques in a mouse head at angles smaller than 10° and energies between 30 and 45 keV. The method is demonstrated at a proof-of-concept level by acquiring the sSAXS data of an amyloid model with an excised head of wild-type mouse for 600 s. This work supports the feasibility of a label-free method based on sSAXS to potentially estimate brain amyloid in small animals.

4.1 Introduction

Increased levels of amyloid plaques in the brain are associated with a wide range of neurodegenerative diseases including Alzheimer's and Parkinson's [35,156]. In Alzheimer's disease (AD), amyloid plaque is characterized by fibrillar aggregates of amyloid-β peptides that are rich in β-sheet structures. Several x-ray diffraction experiments have confirmed amyloid plaque in the brain tissue to give rise to two distinct Bragg peaks due to its cross β-sheet structure [5,35,157]. This characteristic signal is the basis for our x-ray scattering method and holds promise for identifying and characterizing amyloid plaques without the need for laborious sample preparation or administration of contrast agents. The challenge addressed by our proposed method is to probe amyloid plaques in a brain enclosed by an intact skull leveraging the penetration power of x rays. Currently, positron emission tomography (PET) using amyloid specific radioactive tracers is a clinically accepted imaging modality for estimating amyloid load in the *in vivo* brain. However, the regional estimation of brain amyloid load with PET is highly dependent on the uptake and binding behavior of the injected radiotracer [158]. Amyloid PET studies in small animals have provided inconsistent results despite using transgenic mouse models of AD with high amyloid load [55,159]. As an alternative method, contrast-enhanced magnetic resonance imaging (MRI) has been successfully used to quantify amyloid load *in vivo* in various mouse models of AD [67,160]. Since the intrinsic contrast of plaques, which is dependent on iron content, is not a reliable biomarker in MRI, it is necessary to inject a contrast agent, such as gadolinium, in the mouse to detect amyloid plaques.

Here, we introduce a label-free method based on an x-ray scattering technique that has the potential to estimate amyloid load *in vivo*. Our method is based on recording and analyzing the elastically scattered x rays from amyloid plaques in a mouse head at deflection angles smaller than 10° and for incoming x-ray energies greater than 30 keV.

Traditionally, small-angle x-ray scattering (SAXS) techniques irradiate a sample with a focused monochromatic x-ray beam in pencil geometry and measure the elastically scattered x rays in a transmission mode at angles below 10°. The SAXS data analyzed in terms of momentum transfer q can be used to determine the nanometer-scale structure of the material, provided the scattering signal from the structure is above the background level with enough electron density contrast. SAXS is known to discriminate materials based on their scattering features [92]. SAXS has been used to study structures in brain [89, 126], bone [87, 127], breast [161], cardiac tissues [162], dentins [163], and tendons [164]. Most of these studies are done at synchrotron facilities because of the need for a high flux, micro-focused monochromatic x-ray source. Furthermore, with the use of low energy monochromatic x rays, SAXS techniques have so far been limited to the study of thin biological samples. A high energy x-ray source is required for the study of thick samples beyond the mm scale, such as a mouse head. A spectroscopic detector enables full utilization of the available x-ray flux in the energy range of interest, without the need to monochromatize x rays. Exposure times and radiation dose levels can be decreased accordingly to collect the SAXS data in a laboratory (pre-clinical) setting.

4.2 Methods

For demonstrating the method, we assembled a high energy polychromatic x-ray source and a 2D spectroscopic detector in a two-pinhole collimation setup (Fig. 4.1(a)) and simultaneously collected the information for scattered x-ray photons in angle- and energy-dispersive modes, resulting in efficient x-ray quanta utilization [165]. We refer to this approach as spectral SAXS (sSAXS). We have previously demonstrated the sSAXS method for the identification of embedded targets made from caffeine and amyloid synthetic models in up to 5-cm thick objects [144, 165].

Polychromatic x rays (50 kVp, 1 mA, tungsten source) were focused onto the sample using two lead pinholes, P1 and P2, of diameters 2.5 and 0.5 mm respectively. The distance between P1 and P2 was 160 mm. We used a spectroscopic detector made from cadmium telluride (HEXITEC, Quantum Detectors Ltd, Harwell, Oxfordshire, UK) and placed it 220 mm from P2 to record scattered photons between 6 and 50 keV. The energy spectrum at each pixel was recorded with 1 keV bins binning. The detector has 80×80 pixels with a pixel size of 250 μm. The beam stop was placed in front of the detector to block the primary beam while allowing the collection of scattering. The measured beam size on the beam stop was around 0.7 mm due to the divergence of the 0.5-mm x-ray beam (primary) once it reaches the detector. The sample was placed between P2 and the detector with a known sample to detector distance (SDD). Based on the system geometry illustrated in Fig. 4.1(a), scattered photons captured at each pixel have a known scattering angle defined by

2θ. The momentum transfer q is then related to energy (E) and scattering angle by

$$q = \frac{4\pi E \sin\theta}{hc}, \tag{4.1}$$

where h is Planck's constant, c is the speed of light, and $hc = 1.24$ keV nm. Our sSAXS system was configured to cover the q-range from 1.3 to 28 nm^{-1} with E from 30 to 45 keV to study amyloid plaques in a mouse head. All the scattering features of interest are covered in this q-range. Recent Monte Carlo simulation study of the SAXS-CT system has also suggested 30 keV energy range to be an optimal choice in terms of detecting amyloid plaques in a mouse head [98]. It should be noted that at small angles in this energy range, the scattering events are still dominated by elastic scattering. Detail Monte Carlo simulation results for a range of sample thickness and x-ray energies is reported in [93]. The recorded counts in energy bins from 30 to 45 keV were first corrected for attenuation of incident and scattered photons by the sample. If T is the sample thickness along the x-ray path, the total number of scattered photons reaching the detector with negligible multiple scattering can be approximated as

$$N_s(E) = N_t(E) \int_0^T S(x, \theta, E) dx, \tag{4.2}$$

where $N_t(E)$ is the number of transmitted photons of incident beam reaching the detector without beam stop and $S(x, \theta, E)$ is the scattering cross-section distribution. For small scattering angles, the attenuation of incident and scattered photons can be combined [130, 131] and represented by $N_t(E)$. We therefore minimized the

attenuation effect inside the sample by correcting $N_s(E)$ with $N_t(E)$. $N_t(E)$ was experimentally measured by using 0.2 mA tube current, 300 s exposure time, and 27 keV detector threshold. Total pixel counts for an 8 by 8 pixel array covering the location of the transmitted beam was used to estimate $N_t(E)$ for 30 to 45 keV energy bins. The accuracy of the measured transmission factor was found to be within 10% when compared with reference values in the 30–45 keV energy range. Next, we converted the data to get the scattering cross-section as a function of q, $S(q)$, along the beam path by using Eq. (4.1). This conversion is achieved in a two-step process. The first step calculates the attenuation-corrected counts as a function of q per energy bin and the second step sums q-data (Δq = 1.2 nm^{-1}) for all energy bins from 30 to 45 keV (ΔE = 1 keV).

An amyloid model was prepared using bovine serum albumin (BSA) powder (Sigma-Aldrich, St. Louis, MO) without heating. Amorphous and fibrillar aggregates of BSA have β-sheet structures similar to amyloid plaques and can be used as amyloid models [166]. We filled the fine BSA powder in a plastic syringe with an outer diameter of 6.4 mm and an inner diameter of 4.7 mm. The packing density was estimated to be 758 $\pm$ 54 mg/cm^3 by measuring the mass of BSA and the volume of the syringe. The β-sheet content in the lyophilized BSA is less than 25% [155]. In our sSAXS setup, a 0.5-mm x-ray beam traverses through the mouse head to generate the scattering signal. Since the irradiated tissue volume per measurement is small (approximately 1.57 mm^3), our method is more suitable for regions-of-interest (ROI) analysis. A low-resolution scanning experiment to map amyloid load in the whole brain would take several hours. ROI locations can be selected based on the

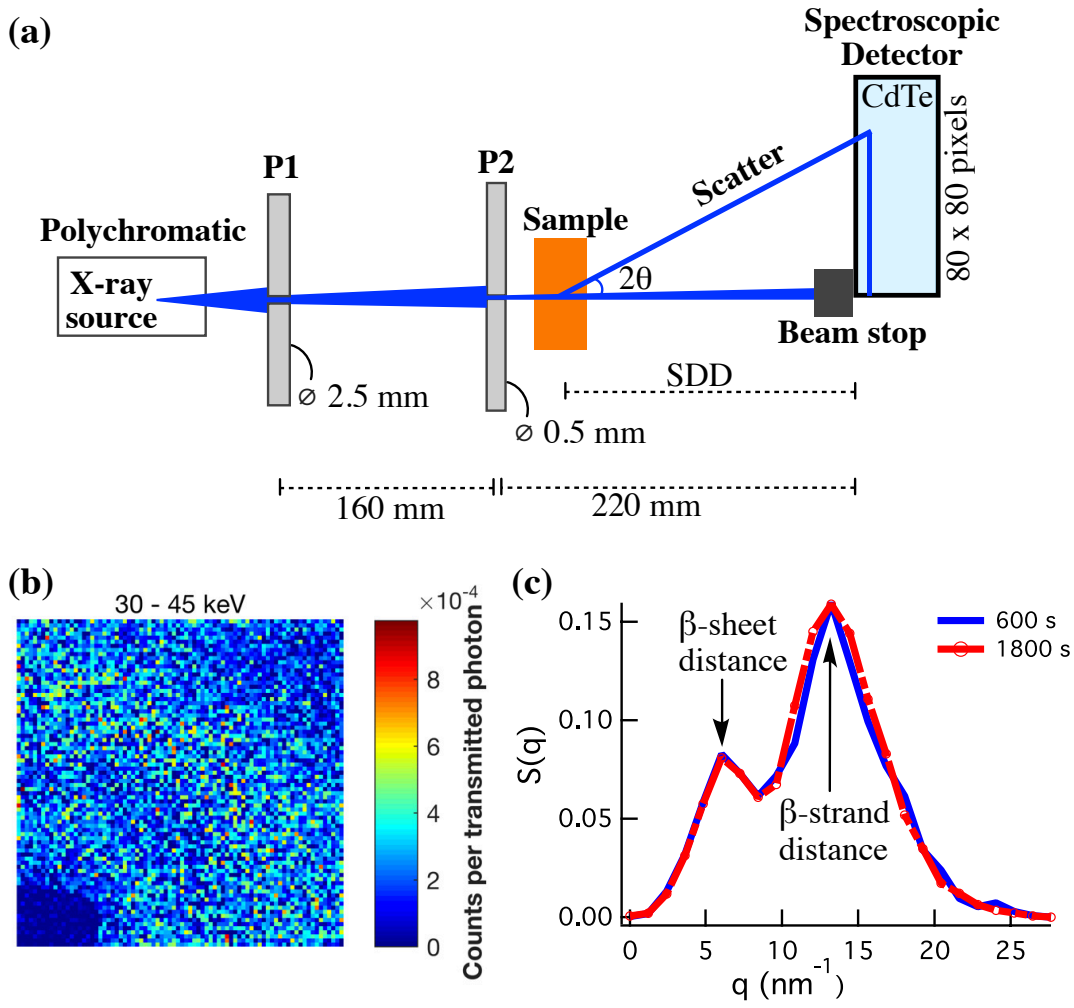


Figure 4.1: Experimental setup and data from an amyloid model in 30 to 45 keV energy range. (a) Schematic of the sSAXS experimental setup to collect scattered x rays at small angles from thick samples using a polychromatic x-ray source and a 2D spectroscopic detector. P1 and P2 are two pinhole collimators and SDD is sample to detector distance. (b) Processed detector data from an amyloid model, after attenuation and background corrections, showing counts per transmitted photon in each pixel in the energy window of 30 to 45 keV. (c) Corresponding scattering cross-section data, S(q), from an amyloid model for 600 and 1800 s measurement times. Distinct peaks around 6 and 13 nm^{-1} are characteristic of the amyloid fibrils or plaques in AD due to their β-sheet structures [5, 6].

spatiotemporal map of amyloid plaque deposition in mice [167]. X-ray beam size can be increased to probe larger tissue volume. The drawback of using a larger beam size, however, is poor q-resolution and possible loss of scattering information due to smearing effects [168, 169].

4.3 Results and discussions

Fig. 4.1(b) shows detector data from an amyloid model after attenuation and background corrections. In this representation, total counts per transmitted photon are shown in each pixel in the energy window of 30 to 45 keV. Background correction was done by subtracting the signal from the empty syringe after performing attenuation correction. Fig. 4.1(c) shows the corresponding scattering pattern from an amyloid model for 600 and 1800 s acquisition times. We see two distinct peaks at approximately 6 and 13 nm^{-1} that are characteristic of the amyloid in AD due to their β-sheet structures [5, 6]. The peak around 6 nm^{-1} corresponds to the 10 Å distance between the β-sheets, and the peak around 13 nm^{-1} corresponds to the 4.8 Å distance between the adjacent β-strands. Overall, 600 s was sufficient to detect these peaks with our sSAXS setup for the concentration of our sample. Thus, the rest of the proof-of-concept study was done with a 600 s acquisition time and used BSA as an amyloid target in a syringe. We also note that the scattering contribution from Compton was found to be less than 9% of the total scatter based on our simulation study of a 4 cm thick water cube (Fig. 4.2). The known Bragg peaks from caffeine powder were also used to validate the sSAXS setup and the data analysis

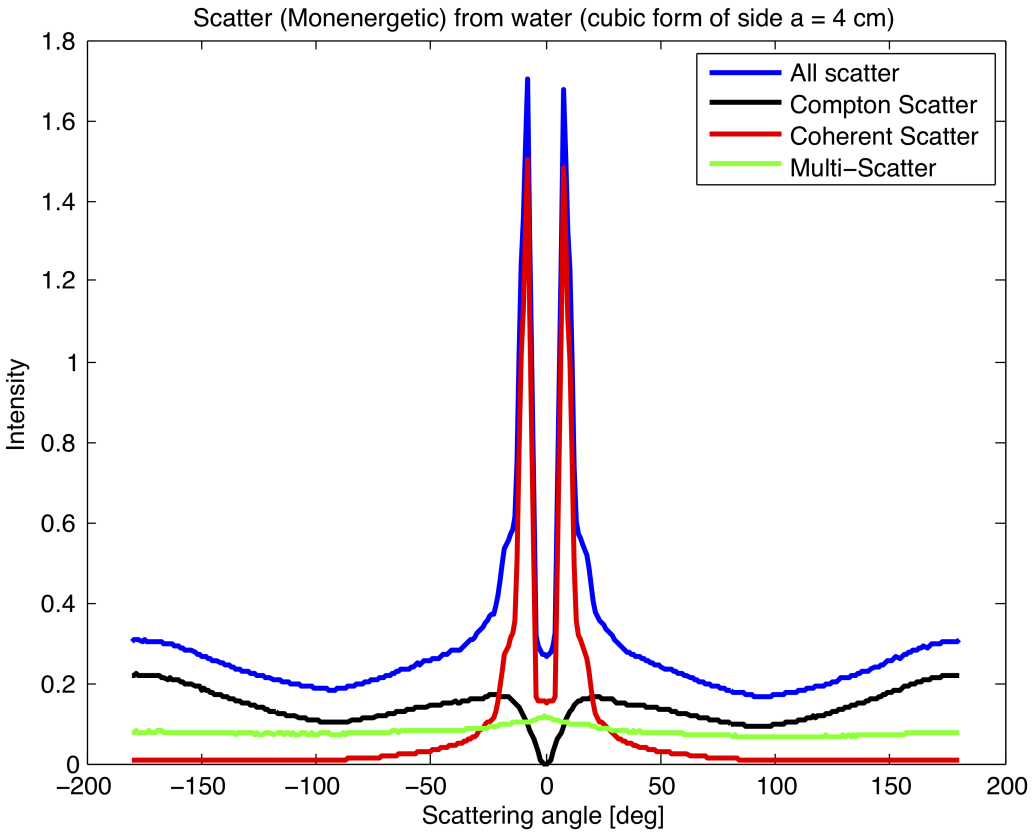


Figure 4.2: Simulation study of the scattering contribution as a function of angle by Coherent, Compton, and multiple-scatter using a spherical detector from a 4 cm cubic of water irradiated with 30 keV monoenergetic x-ray beam.

process (Fig. 4.3).

To estimate amyloid load based on this scattering feature, we prepared six different syringe samples with the mass fraction of amyloid target varying from 0 to 1, and investigated their background subtracted cross-section data by scanning each syringe at three different positions (Fig. 4.4(a)). The mass fraction of BSA was varied by adding gelatin powder as a tissue-mimicking filler [170]. As the mass fraction goes from 0 (gelatin only) to 1 (BSA only), in Fig. 4.4(b), we saw the corresponding increase in the scattering peak around 6 nm^{-1}. In principle, the 13-

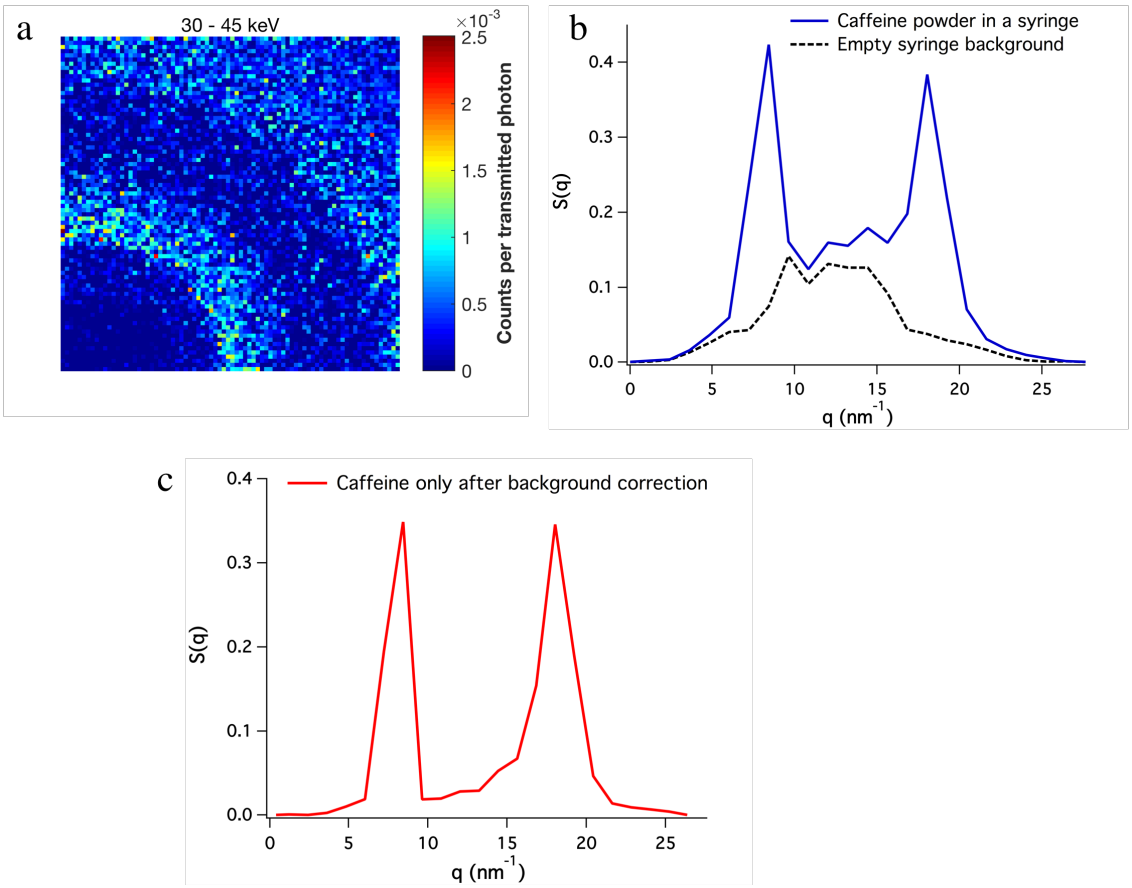


Figure 4.3: Validation of sSAXS setup and data analysis process using the known Bragg peaks of caffeine at 8.4 and 18.8 nm^{-1}. (a) Processed detector data from caffeine powder, after attenuation and background corrections, showing counts per transmitted photon in each pixel in the energy window of 30 to 45 keV. (b) Scattering cross-section data of the caffeine sample and syringe background with 600 s measurement time. (c) Background corrected scattering cross-section data of the caffeine sample.

nm^{-1} peak should also increase proportionally. However, we did not see a significant change in the 13-nm^{-1} signal because of the strong overlapping signal from gelatin at 13 nm^{-1}. Since the mass fraction of gelatin is changing for each syringe, the scattering contribution from gelatin and amyloid target at q=13 nm^{-1} cannot be easily discriminated with background subtraction. In the brain study, the scattering peak around 13 nm^{-1} is affected by varying levels of lipids and aqueous components in different sections of the brain [126]. Therefore, we believe that the technique is more robust if we only consider the peak around 6 nm^{-1} (Fig. 4.4(c)) to estimate amyloid load by calculating the area-under-the-peak (AUP) estimates from 3.6 to 8.4 nm^{-1}.

As shown in Fig. 4.4(d), a linear correlation exists between the mass fraction of the amyloid target and the AUP from 3.6 to 8.4 nm^{-1}. The AUP value for mass fraction 0 can be interpreted as a background level for AUP values. The major source of variability in the estimates of AUP values is likely due to our inability to uniformly mix and pack the amyloid target and gelatin powder in a syringe. As a result, the scattering signal varied somewhat among the three scan locations for the syringe. Additional minor sources of variability in our measurements include small changes in x-ray flux from the x-ray tube and accuracy of measuring transmitted photons.

Finally, we studied a mouse head *ex vivo* with an intact skull to investigate the feasibility of estimating the amyloid load by recovering the characteristic scattering signal from an amyloid target at various locations in the head. Our mouse head study is illustrated in Fig. 4.5(a). All animal handling and sacrificing procedures were

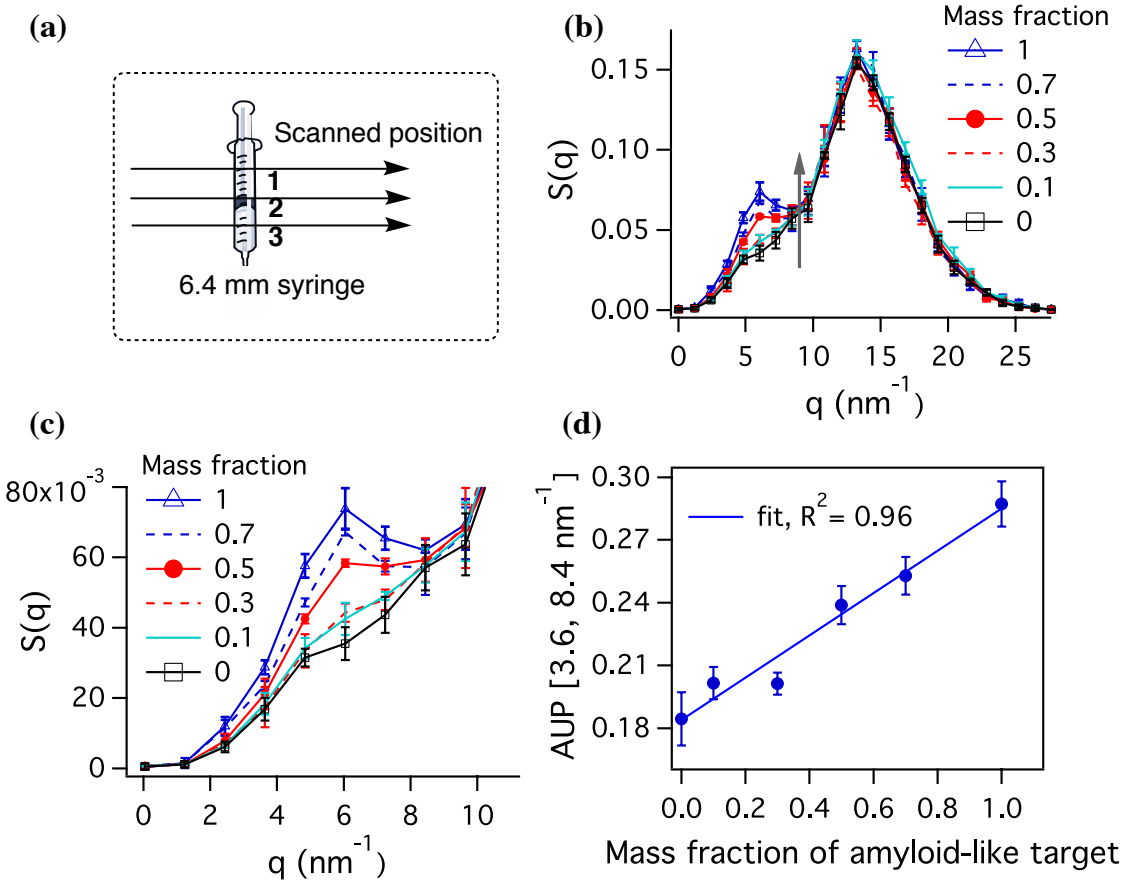


Figure 4.4: Mass fraction study in a syringe. (a) Illustration of a syringe study, in which a syringe with an amyloid target of known mass fraction was scanned at three different positions to report $S(q)$ data as mean $\pm$ standard deviation. (b) $S(q)$ of the amyloid target with mass fraction varying from 0 to 1 in the q-range from 0 to 28 nm^{-1}. (c) $S(q)$ data focusing on the rising peak around 6 nm^{-1}. (d) Linear correlation between the mass fraction of the amyloid-like target and the area-under-the-peak (AUP) from 3.6 to 8.4 nm^{-1}.

approved by the Food and Drug Administration White Oak Institutional Animal Care and Use Committee and were performed in accordance with National Institute of Health animal use guidelines and regulations. An adult wild-type FVB mouse was transcardially perfused with 1X PBS and formaldehyde. The head was removed with the brain remaining in the exposed skull and fixed in formaldehyde. We placed a syringe with an amyloid target (mass fraction of 1) in the front, center, or back of the head with respect to the direction of the primary beam. When an amyloid target is placed in the front, the x-ray beam first encounters the amyloid target followed by the mouse head, and vice versa for the target in the back. The head was split in half using a sharp blade to insert an amyloid target in the center of the head. The x-ray beam consecutively encounters the first half of the head, the enclosed target, and the second half of the head. Data were acquired three times at the same position for 600 s.

Fig. 4.5(b) shows the scattering patterns of the mouse head with and without an amyloid target in the front, center, and back position. In this study, the center target is of main interest as plaques are embedded in the brain. The front and back target measurements were performed to understand the signal change in extreme cases for validation. The SDD for the back target was adjusted from 214 mm to 201.8 mm to accommodate the mouse head. The SDD for the center target was 207.9 mm. We recovered the characteristic scattering peaks from the amyloid target around 6 and 13 nm^{-1} by subtracting the scattering signal contributed by the head with no amyloid target (Fig. 4.5(c)). Unlike our mass fraction study using gelatin, the 13 nm^{-1} peak appears to be correlated with the 6 nm^{-1} peak. This correlation

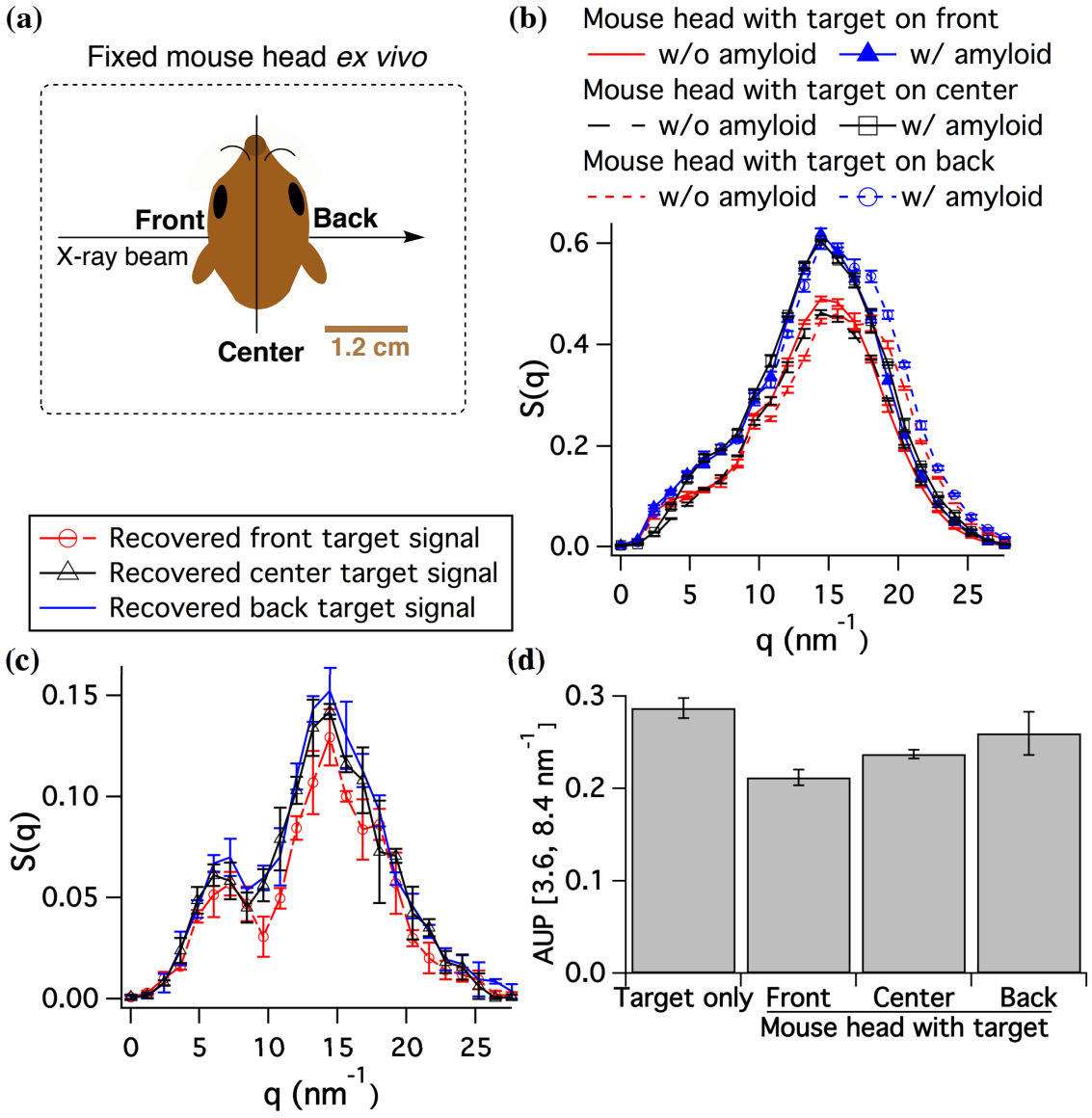


Figure 4.5: Mouse head study with an intact skull. (a) Illustration of a mouse head study ex vivo. A syringe with an amyloid target is placed in the front, center or back of the fixed mouse head with respect to the x-ray beam direction. The measurement was repeated three times at each position to report $S(q)$ as mean $\pm$ standard deviation. (b) $S(q)$ of the mouse head with and without an amyloid target on front, center, and back with 600 s measurement time. (c) Recovered $S(q)$ of the front, center, and back amyloid targets after subtracting the scattering signal contributed by the mouse head. (d) Corresponding AUP values from the recovered signal of the front-, center- and back-configuration in a mouse head in comparison to the target alone in a syringe. Front = Ipsilateral, center = medial, and back = contralateral.

might be due to the background subtraction using measured scattering from the same location of the head without any amyloid target. The mouse head alone has a strong scattering signal that interferes with the 13 peak nm^{-1} from amyloid. We selected AUP from 3.6 to 8.4 nm^{-1} to avoid variability associated with background subtraction affecting the magnitude of the 13-nm^{-1} peak. The results in terms of AUP (Fig. 4.5(d)) are slightly higher for the back target versus the front and center targets. AUPs for the front, center, and back targets are correspondingly 0.74, 0.83, and 0.90 of the reference value from the target only study with syringe. These findings suggest that the signal from amyloid plaques is affected more significantly if the scattered photons from plaques need to pass though the whole head before reaching the detector. The possibility of getting lower than expected AUP values in the mice study should be taken into account while estimating the amyloid load.

It is not possible to know the exact distribution of amyloid plaques in the brain along the x-ray path. One approach to minimize AUP underestimation is to perform the analysis by considering the sample-to-detector distance from the center of the mouse head. In this case, we assume amyloid plaques are concentrated around the center of the brain to estimate an average AUP value. Since the x-ray beam can encounter plaques anywhere in the brain along its path, this also imparts uncertainty in q values of the amyloid signal at each scanned location. For the size of the mouse head, uncertainty in q at high energy can reach up to 1 nm^{-1}. However, our method is somewhat insensitive to this effect since it leverages low-resolution q data and relies on the calculation of AUP within a broad q range to estimate amyloid load.

The results support the feasibility of label-free detection of amyloid signals

in a mouse head using x-ray scattering. We used a high packing density of BSA to prepare our amyloid model and test the proposed method. The coefficient of variation in AUPs with 600 s acquisition time was less than 10%. AUPs from 3.6 to 8.4 nm^{-1} can be used to estimate amyloid load. Future work requires a correlation study between the β-sheet content of the amyloid model and amyloid plaques found in AD brains or a direct age-dependent study of an AD mouse model (e.g., 5XFAD). It is worth mentioning that there are other non-amyloid proteins or structures in the brain that contain beta-sheets. However, the relative concentration of beta-sheets in brains with amyloid plaques is likely significantly higher. Using synchrotron-based Fourier transform infrared micro-spectroscopy, Klementieva et al. have shown an elevated level of beta-sheet content in the AD mouse brains in comparison to wild-type mice [32]. This beta-sheet content steadily increases early on in the 2- to 3-months-old mice with AD, even prior plaque formation [32]. Therefore, the concept of using the x-ray scattering signal from beta-sheets to quantify amyloid load in an intact head remains promising.

Furthermore, we scanned a wild-type mouse head to study the behavior of background signals due to beta-sheet structures present in the normal brain and did not find any strong scattering signal around 6 nm^{-1} (Fig. 4.6). We also found that any background signal (except when taken near the orbital region) can be used for background subtraction to recover the characteristic signal of amyloid plaques associated with beta-sheets. In an *in vivo* experiment, the reference region in a mice head without amyloid plaques can be established for background subtraction to recover the signal from amyloid plaques. This can be similar to an amyloid PET

study, where one of the reference regions is considered to be the cerebellum [171,172]. Alternatively, a comparative scanning study between healthy and AD mice can be done without establishing the reference region.

4.4 Conclusion

In summary, we described a method based on SAXS to potentially estimate brain amyloid in small-animals without using contrast agent. We demonstrated the feasibility of this label-free method by acquiring the SAXS data of an amyloid model and a mouse head *ex vivo* in the 30 to 45 keV energy range. The proposed method allows for using a polychromatic x-ray source in conjunction with a spectroscopic imaging detector in a laboratory setting. Since a pencil beam is used to probe the tissue, our method is more suitable for brain ROI analysis. Scanning the whole brain can be time-consuming and may impart a high radiation dose unless x-ray exposure time is reduced to a few seconds per measurement. This can be done by increasing the x-ray beam size to probe larger tissue volumes and by increasing x-ray flux in the 30–45 keV energy range. The main advantage of our method is that it can be optimized to estimate amyloid load within a few minutes in selected brain regions without any sample preparation. Sample preparation is not required because we directly study thick samples and capture the scattering highly specific to amyloid plaques. We can study both small-animal and human heads as the x-ray energy range can be selected to maximize the elastic scattering signal while minimizing the radiation dose [93,173]. We have already demonstrated the capability of the sSAXS

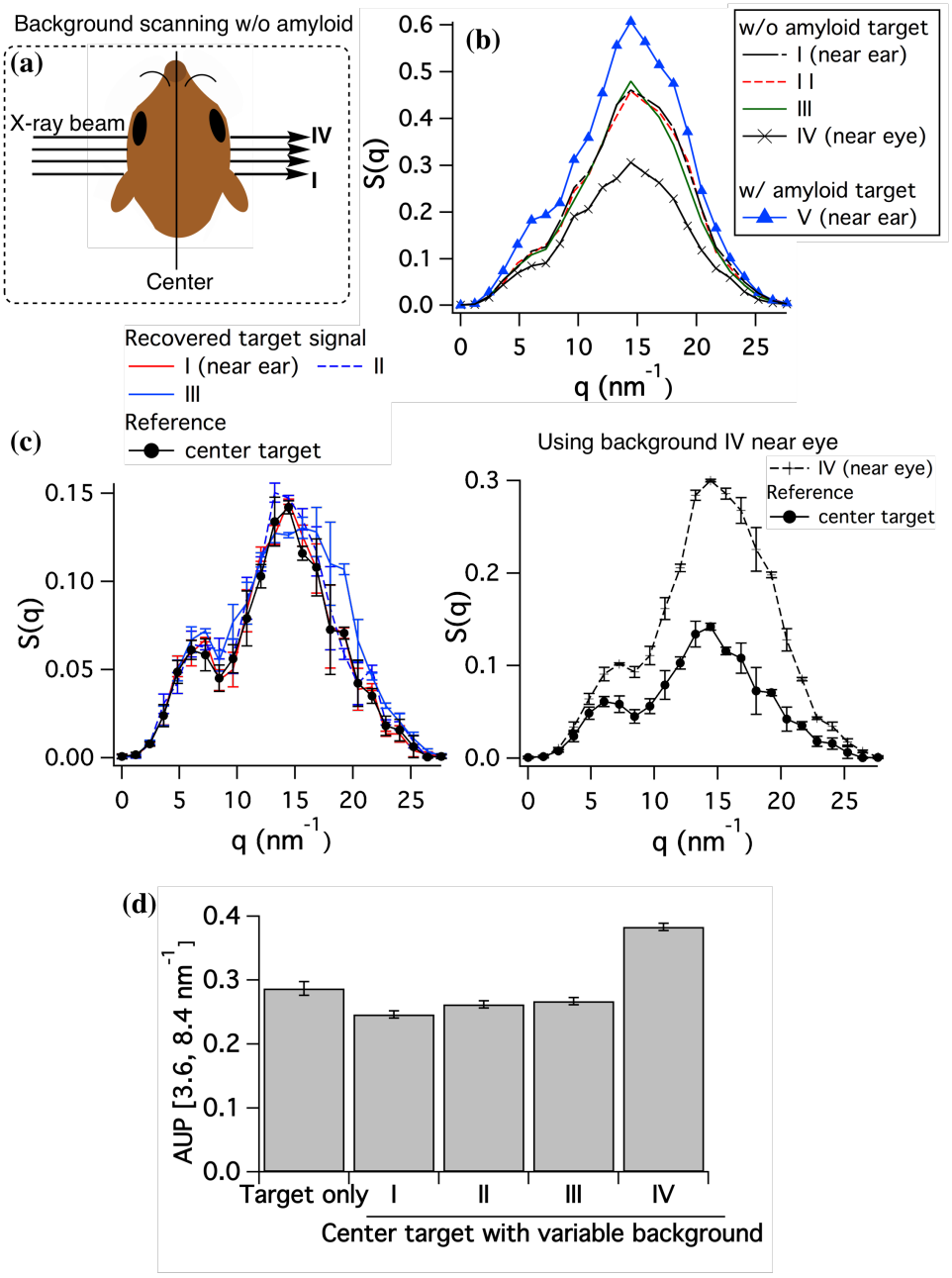


Figure 4.6: (a) Illustration of the scanning study of a wild-type mouse head *ex vivo* without an amyloid target from ear (I) to eye (IV). (b) $S(q)$ of the mouse head at various scanned locations with and without an amyloid target in center. (c) Recovered $S(q)$ of amyloid targets after subtracting the background scattering signal (w/o amyloid) collected from position I to IV. (d) Corresponding AUP values in comparison to the target alone.

method to identify embedded targets in up 5-cm thick objects [165]. A possible disadvantage of our method is the potential for a high radiation dose when multiple brain regions are studied with long measurement times. In future work, we aim to reduce the measurement time to less than 60 seconds through various system design optimizations and to evaluate the method using AD mouse models with biological amyloid plaques. Our method offers an efficient new approach towards quantifying amyloid load without using resource-intensive techniques such as PET or MRI that require the administration of a contrast agent. This proof-of-concept study is the first step towards a practical implementation of this method for small animals.

Acknowledgments

The content of this chapter has been published in the following journal article: Dahal, E., Ghammraoui, B., & Badano, A. Feasibility of a label-free x-ray method to estimate brain amyloid load in small animals. Journal of Neuroscience Methods (2020). B.Ghammraoui helped with experimental setup and data corrections. B. Ghammraoui performed simulation studies to generate Fig. 4.2.

Chapter 5: Label-free estimation of brain amyloid burden in AD mouse model

Amyloid plaque deposits in the brain are indicative of Alzheimer's and other diseases. Measurements of brain amyloid burden in small animals require laborious post-mortem histological analysis or resource-intensive, contrast-enhanced imaging techniques. We describe a label-free method based on spectral small-angle x-ray scattering with a polychromatic beam for *in vivo* estimation of brain amyloid burden. Using a mouse model of Alzheimer's disease (5XFAD), we demonstrate a practical x-ray method to estimate amyloid burden within minutes with no contrast agents. Our findings comparing 5XFAD versus wild-type mice correlate well with histology. This work shows promise for a fast and practical *in vivo* technique and opens new possibilities of conducting more efficient longitudinal mice studies tracking amyloid burden.

5.1 Introduction

The presence of β-sheet rich amyloid plaques in the brain has been associated with a wide range of neurological diseases including Alzheimer's and Parkinson's [35,174]. Amyloid plaques in Alzheimer's disease (AD) are formed by aggrega-

tion of amyloid-β (Aβ) peptides into fibrils and their extracellular deposition in the brain [174]. Measurements of amyloid burden require laborious post-mortem histological analysis or resource-intensive contrast-enhanced imaging techniques. As Aβ plaques accumulate in the brain, *in vivo* estimation of amyloid burden is necessary for understanding AD pathogenesis and progression, and for designing diagnostic and therapeutic approaches. While the histology reagents are relatively inexpensive, it requires days to prepare, stain, and image thin brain slices individually. Positron emission tomography (PET) uses radiolabeled compounds that bind to amyloid fibrils with moderate specificity [175]. While this method is clinically employed, its use has been limited due to cost and availability of PET scanners and by the need to inject a radioactive substance in humans. In small-animal preclinical studies, amyloid PET has provided unconvincing results even for AD mouse models with high amyloid load in part due to non-specific binding [55, 159]. More recently, magnetic resonance imaging (MRI) has shown potential for quantifying amyloid burden *in vivo* in various AD mouse models. However, MRI techniques depend on administering an exogenous contrast agent typically based on gadolinium compounds [67]. The need for readily assessing amyloid burden *in vivo* without using contrast agents has not yet been resolved. We demonstrate a label-free, fast and non-invasive method based on spectral small-angle x-ray scattering (sSAXS) to estimate amyloid burden by studying wild-type and 5XFAD mice with a prototype system and correlating the estimated amyloid burden with histology.

Small-angle x-ray scattering (SAXS) is a well-established technique for identifying molecular structures based on their scattering patterns [92, 176]. SAXS is

limited to the study of thin samples (mm scale) with the use of low-energy monochromatic x rays. In sSAXS, we improve system efficiency by simultaneously collecting SAXS data in angle- and energy-dispersive modes using a polychromatic x-ray beam and a 2D spectroscopic detector. In this approach, elastically scattered x rays at angles below 10° are acquired by the detector with no energy filtering. For each detected quanta, the detector records the energy and location information into an three-dimensional image output. This approach overcomes the sample thickness limit of traditional SAXS and allows the exploration of *in vivo* application with higher energies utilizing all available scattering flux in the energy range of interest. Using Monte Carlo simulations, we have shown that the energy range can be selected to maximize elastic scattering per deposited energy in thick samples [93]. In another study, we have experimentally demonstrated the capability for identifying embedded targets in up to 5-cm-thick objects [165] and in wild-type excised mouse heads [177] with an energy range from 30 to 45 keV.

5.2 Methods

We prepared an amyloid model using bovine serum albumin (BSA) powder (Sigma-Aldrich, St. Louis, MO) with cross β-sheet structures similar to amyloid plaques seen in AD patients [144]. A 6.4 mm diameter plastic syringe was filled with BSA powder to a packing density of 758 ± 54 mg/cm^3. The amyloid model was used to illustrate the data analysis process and show the scattering signal characteristic of β-sheet rich structures.

5.2.1 Animals

All animal experimental procedures and protocols were approved by the Indiana University School of Medicine Institutional Animal Care and Use Committee (IACUC) and performed in accordance with US National Institutes of Health and AAALAC International guidelines and regulations on animal care. The 5XFAD mouse line contains the human amyloid precursor protein and presenilin transgenes with five mutations associated with AD [178]. 5XFAD mice exhibit severe Aβ deposition at an early age. Aβ continues to accumulate until 10-14 months of age. 5XFAD mice (n=3) and nontransgenic wildtype (WT) mice (n=3) on the same background were aged 11 months. Animals were housed at Indiana University School of Medicine Laboratory Animal Resource Center under a 12 h light/dark cycle. Animals had access to food and water *ad libitum*. Mice were transcardially perfused with 1X phosphate buffered saline and formaldehyde. Heads were removed from the body and shipped to our lab to be used in the study (Fig. 5.1). Two sets of AD and WT mouse heads were used for the sSAXS study followed by the histological analysis. A separate set of AD and WT mouse heads were used for initial testing in the sSAXS study to scan and locate the region of interest.

5.2.2 Experimental prototype

We built a sSAXS system by assembling a polychromatic x-ray source (tungsten anode, MXR-160/22, COMET) and a 2D spectroscopic detector made from 1-mm thick cadmium telluride (HEXITEC, Quantum Detectors Ltd, Oxfordshire,



Figure 5.1: AD and WT mouse head samples used in the sSAXS study.

UK). The system is described in detail elsewhere [165]. Briefly, polychromatic x rays were generated using a 50-kVp tube voltage and 2-mA current. The beam is collimated to irradiate the mouse head using two lead pinholes of 2.5 and 1.0 mm diameter respectively. The two pinholes were 160 mm apart and the sample to detector distance (SDD) was 214 mm. The detector (80×80 250-μm pixels) recorded scattered photons with energies between 6 and 50 keV using a bias voltage of -400 V, a 5-keV energy threshold and 1-keV energy bins. The image acquisition time was 300 s. A beamstop in front of the detector was used to block the primary rays to avoid pulse pile-up while recording the scattered photons. An energy-dependent transmission correction factor was calculated using spectroscopic measurements of the primary beam with and without the sample present, without the beam stop and

using a 0.2-mA tube current, and a 27-keV energy threshold [165].

5.2.3 Data analysis

Similarly to traditional SAXS, sSAXS analyzes scattering data in terms of momentum transfer q [165]. The scattered photons recorded at each pixel have a known scattering angle (2θ) and energy (E). The momentum transfer is given by

$$q = \frac{4\pi E \sin\theta}{hc}, \tag{5.1}$$

where $hc = 1.24$ keV.nm. The q range analyzed in our sSAXS setup was from 1.3 to 28 nm^{-1} with E from 30 to 45 keV. Let $N_s(i, j, E)$ be the detector data corresponding to scattered photon counts in each pixel within an energy bin, where (i, j) denotes the pixel index. If T is the sample thickness along the x-ray path, $N_s(i, j, E)$ can be written as

$$N_s(i, j, E) = N_t(i, j, E) \int_0^T S(x, \theta_{ij}, E)dx, \tag{5.2}$$

where $N_t(i, j, E)$ is the photon counts of primary (unscattered) quanta after transmitting through the sample and $S(x, \theta_{ij}, E)$ is the angular and energy scattering cross-section. $N_s(i, j, E)$ was divided by $N_t(i, j, E)$ to account for energy-dependent transmission and detector response [132,165]. Eq. 5.1 represents the scattering cross-section data as a function of q per energy bin. Finally, $S(q)$ was summed for all energy bins (30 to 45 keV). The bin size in q was 1.2 nm^{-1}. We then calculate the

area under the peak (AUP) from 3.6 to 8.4 nm^{-1}. ΔAUP represents the amyloid burden per location (i) calculated as

$$\Delta AUP = \frac{AUP_i - \overline{AUP}_{WT}}{\overline{AUP}_{WT}}, \tag{5.3}$$

where AUP_i is the AUP in each location under investigation and $\overline{AUP}_{WT}$ is the mean of all ROIs in the WT mouse (n=2). All locations in AD and WT mice were location-matched for comparison. ΔAUP represents a relative measurement of amyloid burden compared to WT measurements. The theoretical minimum value for ΔAUP is 0 and corresponds to a level seen in WT indicative of non-disease. However, its maximum value can be greater than 1. In order to scale ΔAUP from 0 to 1, one could use an age-dependent mice study with appropriate sample size to find minimum and maximum population-based AUP values, similarly to the recently proposed Centiloid metric for standardizing amyloid PET data [62].

5.2.4 Histology.

Histological analysis was performed using a Thioflavin-S staining protocol [179]. The skull was removed from the mouse head to slice the brain into 50 μm sagittal sections using a vibrating microtome. Two slices from each hemisphere of the brain (total four slices per brain) at lateral distances of 1 and 2 mm were stained with 0.1% Thioflavin-S solution. The slices were then mounted onto glass slides and imaged using a fluorescence microscope (Axio Observer, Zeiss). ImageJ software (https://imagej.nih.gov/ij/) was used to calculate the amyloid load as per-

cent area (percent number of pixels in the image) covered by the plaques in the ROI [180]. Three locations were selected for analysis based on the sSAXS study. ROI was defined to be a 1 mm circle matching the size of the x-ray beam. The Allen Mouse Brain Atlas [7] was used to identify the brain regions. Images were background subtracted to match average pixel values of WT and AD brain slices in regions without amyloid plaques, and thresholding was applied to highlight any Thioflavin-S positive plaques. The percent area of plaques in the circular ROI was calculated. For each 5XFAD mouse, the average of four slices was reported as the amyloid load for each location.

5.3 Results and discussions

Fig. 5.2a shows a schematic of the experimental sSAXS setup. A dual-pinhole collimated beam of polychromatic x rays is directed at the mouse head in selected locations in a sagittal plane between eye and ear. The x-ray beam path is normal to the sagittal plane. The sSAXS data processing steps are illustrated using data collected for an amyloid model in Fig. 5.2b. First, the detector data in the energy range from 30 to 45 keV is transmission corrected and converted to scattering cross section, $S(q)$, per energy bin. The $S(q)$ is then summed for all energy bins. Using these processing steps (see Methods section for details), we see two characteristic peaks for the amyloid model at 6.04 and 13.24 nm^{-1} due to its cross-β structure [35, 144]. X-ray diffraction methods have identified the same two peaks when characterizing amyloid-rich thin tissue sections of mouse and human brain [5, 35]. Since the signal

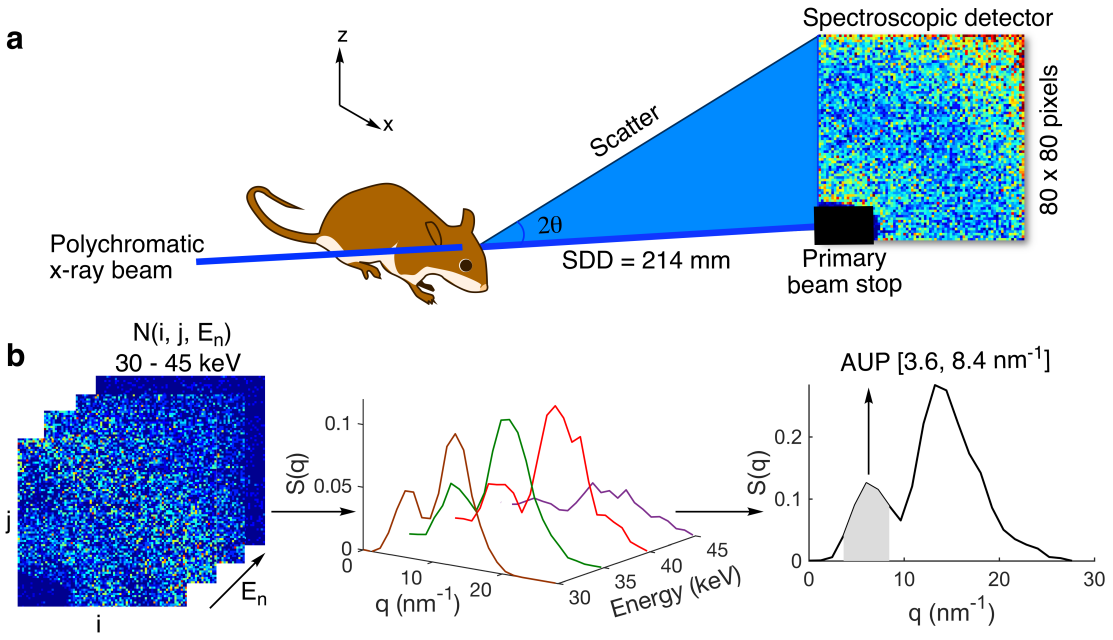


Figure 5.2: Schematic of the experimental sSAXS setup and data processing steps. (a) The mouse head is irradiated at select locations with a collimated beam of polychromatic x rays of 1 mm diameter. A 2D spectroscopic detector (CdTe) is used to collect SAXS data simultaneously in angle- and energy-dispersive modes for each location. The sample to detector distance (SDD) was 214 mm (b) sSAXS data processing steps in 30 to 45 keV energy range are illustrated using an amyloid model from BSA with two Bragg peaks at 6.04 and 13.24 nm^{-1}. The 2D detector data (left) showing counts in each pixel per energy bin is converted to scattering cross section, $S(q)$, per energy bin (middle) after applying a transmission correction. The $S(q)$ is then summed ($\Delta q = 1.2$ nm^{-1}) from 30 to 45 keV to combine scattering information in all energy bins and to calculate the area under the peak (AUP) from 3.6 to 8.4 nm^{-1} (right).

increases with amyloid plaque density [177], we used the area under the peak (AUP) from 3.6 to 8.4 nm^{-1} to estimate the amyloid burden. We chose not to use the broad peak at 13.24 nm^{-1} because of significant overlap with the scattering signal from the lipid content of brain tissues [126].

To non-invasively locate the selected region-of-interest (ROI) in the mouse heads, we acquire a scout scan for a set of AD and WT mouse heads between eye and ear (sagittal plane, $\Delta x = 2$ mm) at different axial heights ($\Delta z = 1$ mm) with a

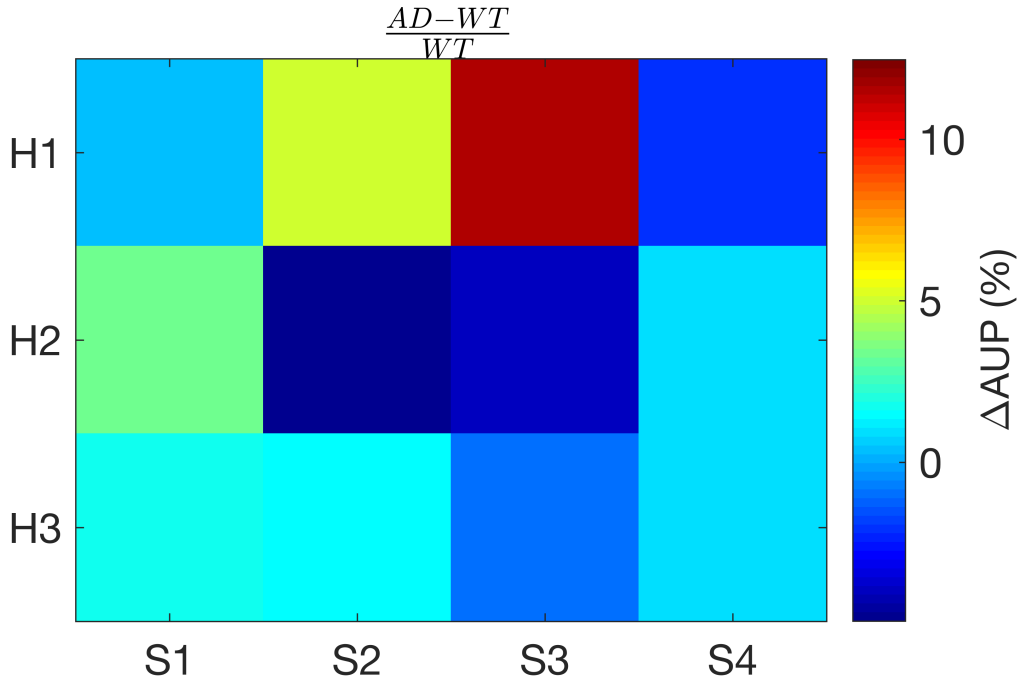


Figure 5.3: Initial AD and WT mouse head scanning results with a 0.5 mm polychromatic x-ray beam. Each mouse head was scanned between eye and ear (S1-S4, sagittal plane, $\Delta x = 2$ mm) at different heights (H1-H3,$\Delta z = 1$ mm)

0.5 mm x-ray beam. H1S2 and H1S3 showed a strong signal from amyloid plaques, whereas H3S4 showed weak or no signal (Fig. 5.3). We chose three ROIs (H1S2, H1S3, H3S4) for a detailed study with a 1-mm x-ray beam based on this scout scan. The mouse heads were then cut into halves to find the approximate ROI locations using an anatomic atlas as visual reference (Fig. 5.4a). H1S2 corresponds to the isocortex's somatomotor and somatosensory regions, H1S3 corresponds to the isocortex's visual, posterior parietal association and somatosensory regions as well as to the hippocampus (hippocampal and retrohippocampal regions), and H3S4 to midbrain and pons regions.

ΔAUP (represented as fraction) relative to the WT mice was used to estimate amyloid burden in each location (see Methods section). For comparison, histological

analysis was performed to estimate amyloid load (%) after completing the sSAXS study. First, the skull was removed and the brain was sliced into 50-μm sagittal sections. Two slices from each hemisphere of the brain at lateral distances of 1 and 2 mm were stained with 0.1% Thioflavin-S solution. The average of four brain slices $\pm$ standard deviation was used to report amyloid load for each location (see Methods).

We found a strong correlation (Pearson $r = 0.94$, $P < 0.001$) between the ΔAUP calculated with our sSAXS method and the amyloid load estimates derived from histology (Fig. 5.4b). Tabulated data are provided in Table 5.1. Fig. 5.4c shows $S(q)$ of AD and WT mice used for ΔAUP calculation, where the AUP is taken from 3.6 to 8.4 nm^{-1}. Consistent with histology, the maximum ΔAUP (0.15 $\pm$ 0.03) was observed in H1S3 of the first 5XFAD mouse (AD I) corresponding to the isocortex and hippocampus regions. ΔAUP for the second 5XFAD mouse (AD II) in H1S3 and H1S2 also showed high amyloid burden. Typical of 11 months old 5XFAD mice [178], amyloid plaques were concentrated in the subiculum corresponding to H1S3 and distributed in the inner layers of the cortex as seen in H1S2 ((Fig. 5.4d). We found ΔAUP in H1S2 of AD I to be slightly lower than that measured by histology likely due to a mismatch in the studied location within the isocortex while placing the mouse head in the x-ray beam. We observed a ΔAUP of -0.02 $\pm$ -0.05 in H3S4 of AD I corresponding to the midbrain and pons regions. A zero or negative ΔAUP indicates no significant presence of amyloid plaques. In H3S4 of AD I, the histological amyloid load was 1.4 $\pm$ 1.5%. We saw a positive ΔAUP value on average for H3S4 of AD II. The average histological amyloid load in this case was

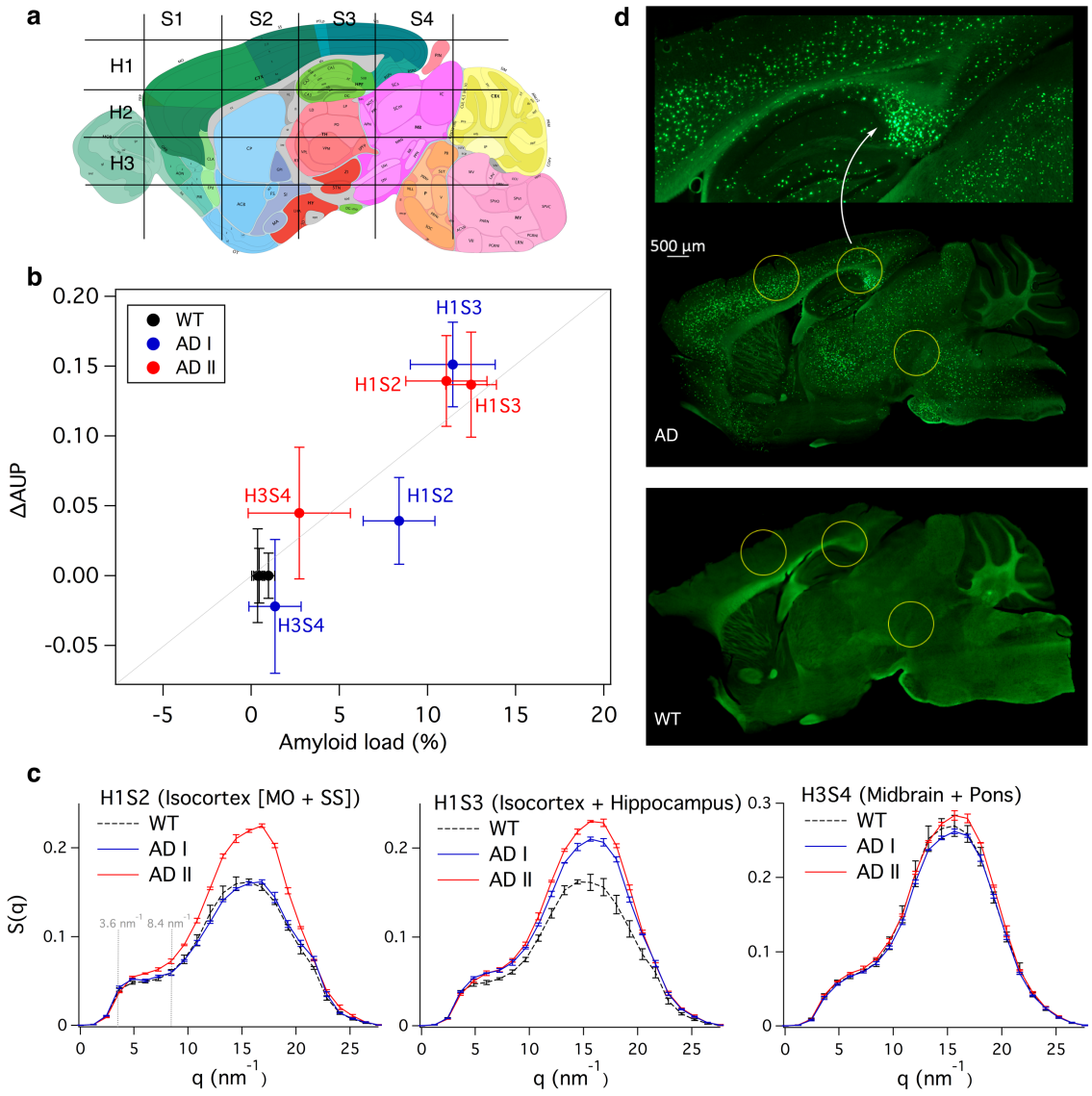


Figure 5.4: Amyloid burden estimations in intact heads corresponding to 5XFAD mice and WT controls. (a) Approximate studied locations in the mouse brain in comparison to an anatomic reference image from the Allen Mouse Brain Atlas containing major brain regions in a sagittal plane [7]. (b) Correlation between the ΔAUP calculated from the sSAXS method and the amyloid load estimates derived from histology for three locations (Pearson $r = 0.94$, $P < 0.001$). (c) Corresponding S(q) of AD and WT mice used for ΔAUP calculation after studying their heads with an intact skull in each location for 300 s. Error bars represent ± standard deviation from three measurements for each location. (d) Representative histology images of AD and WT brain slices using Thioflavin S. The zoomed image (top) is focused on the hippocampus of AD brain slice.

about twice that seen in AD I. Our sSAXS method was sensitive enough to detect a 2.7 ± 2.9% amyloid load reported by histology. The primary source of variability in AUP is due to location uncertainty while repositioning the mouse head for three consecutive measurements in the 1-mm x-ray beam. The variability contributed by the instrument alone is less than 10% [165]. Our sSAXS method can be improved by decreasing location uncertainty. A two-dimensional scout x-ray image taken with the same detector in transmission mode could allow more accurate target localization prior to the start of the sSAXS acquisition. A three-dimensional scout image using a fast (under-sampled) accessory computed tomography setup could provide additional location accuracy.

	H1S2 (isocortex [MO + SS])		H1S3 (isocortex + hippocampus)		H3S4 (midbrain + pons)	
	ΔAUP	Amyloid load (%)	ΔAUP	Amyloid load (%)	ΔAUP	Amyloid load (%)
WT	0.00 ± 0.02	0.5 ± 0.3	0.00 ± 0.02	0.9 ± 0.4	0.00 ± 0.03	0.4 ± 0.3
AD I	0.04 ± 0.03	8.4 ± 2.0	0.15 ± 0.03	11.4 ± 2.4	-0.02 ± -0.05	1.4 ± 1.5
AD II	0.14 ± 0.03	11.1 ± 2.3	0.14 ± 0.04	12.5 ± 1.4	0.04 ± 0.05	2.7 ± 2.9

Table 5.1: Tabulated data of ΔAUP (fraction) and amyloid load (%).

We chose a 1-mm x-ray beam to improve signal-to-noise ratio while curtailing smearing (Fig. 5.5). Radiation levels might limit *in vivo* applications if long exposure times are required to study multiple brain locations. Exposure time can be reduced by increasing photon counts in the energy range of interest (30 to 45 keV) through various system optimizations. In addition, X rays with energy below 30 keV can be filtered out from the beam before irradiating the sample to reduce absorbed dose.

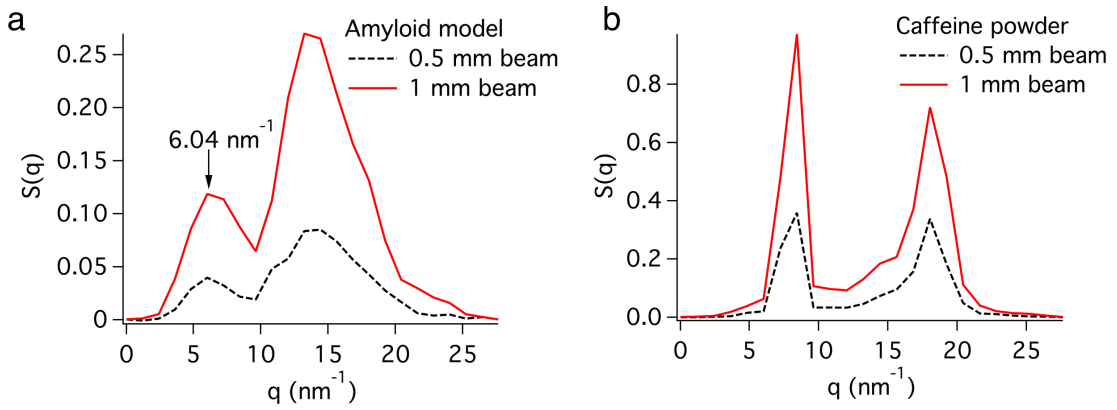


Figure 5.5: S(q) of amyloid model (a) and caffeine (b) using 1 mm vs. 0.5 mm x-ray beam spot size.

5.4 Conclusion

We studied 5XFAD mice and demonstrated the capability of a novel sSAXS method to estimate brain amyloid burden in mice without contrast agents and in a non-invasive manner. The sSAXS method enables the *in vivo* estimation of amyloid burden by integrating a polychromatic x-ray source with a 2D spectroscopic detector. The method is relatively fast (a few minutes) and convenient for the analysis of amyloid burden in small animals within a preclinical setting.

Acknowledgments

The content of this chapter will be published in the journal article as: Dahal, E., Ghammraoui, B., Ye M., Smith J.,& Badano, A. Label-free x-ray estimation of brain amyloid burden. (under review). B. Ghammraoui helped with sSAXS instrumentation and data corrections for the spectroscopic detector; M. Ye prepared brain slices; M. Ye together with E.Dahal performed the histological analysis.

Chapter 6: Future Directions

In this final chapter, we summarize the overall contribution of this thesis and explore future directions for small animals and human studies. The work presented in this thesis experimentally demonstrates a promising new method based on sSAXS to estimate amyloid burden in the brain of small animals. To do this, we successfully designed and built an sSAXS prototype capable of probing thick samples in the cm-scale. The prototype was created by assembling a polychromatic x-ray source and a 2D spectroscopic detector in a two-pinhole collimation setup. We efficiently measured the elastically scattered x rays below 10° without collimating the scattered rays or filtering the energy spectrum. We first validated the prototype in a general setting by acquiring the known and easy to detect Bragg peaks of caffeine at 8.44 and 18.64 nm^{-1} in 30 to 45 keV energy range. In particular, we analyzed caffeine as a target material embedded in 1 to 5 cm PMMA slabs to demonstrate the capability of sSAXS technique to identify caffeine targets in all cases within 600 s. This type of study is not possible in traditional SAXS because of the sample thickness limit in the mm-scale. Additionally, using caffeine data as an example, we presented the sSAXS data analysis workflow to convert angle- and energy-dispersive raw detector data to 1D scattering signal with background and attenuation correc-

tions. The accuracy of transmission measurement for attenuation correction was within 10%. Furthermore, by performing area-under-the-peak (AUP) analysis, we show the impact of PMMA thickness and target position on estimating the caffeine amount from the recovered signal. We found that AUPs were slightly overestimated ($< 11\%$) due to signal contamination by PMMA when the scattered photons from the caffeine target traverse through 1 to 3 cm PMMA slabs.

Next, we presented a scalable method to prepare an amyloid model for phantom studies. Amyloid detection is based on the distinct scattering signals from amyloid plaques due to its β-sheet structure. Phantom studies using amyloid models are needed to test the feasibility of using sSAXS prototype for amyloid detection in thick samples without using expensive $A\beta$ peptides. Therefore, we used readily available plasma protein (BSA) to successfully prepare an amyloid model with cross β-sheet structures similar to amyloid plaques seen in AD brains. An amyloid model was prepared with and without using the heat-induced aggregation process. We consistently found distinct scattering peaks around 6 and 13 nm^{-1} associated with β-sheet structure from our amyloid model without heating, similar to amyloid plaques when characterizing samples in brain tissues and PMMA phantoms. The unheated amyloid model providing consistent signal was used to make amyloid-like targets in a mouse head study with skull. The amyloid-like target of high packing density was placed at various locations in a fixed head of WT mouse, and the characteristic scattering signal from the target was recovered for all locations using sSAXS. This was achieved despite the presence of strong scattering from the mouse head around 14 nm^{-1}. The coefficient of variation in the amyloid load estimate

given by AUPs was found to be less than 10%. Since amyloid plaque levels vary in the brain, we also established a linear correlation between the mass fraction of the amyloid target and AUP of the scattering curve. We studied six different syringe samples with the mass fraction of amyloid target varying from 0 to 1. The key benefit of our sSAXS approach is that it can be optimized to estimate amyloid load in selected brain regions of an intact head within minutes and without using an exogenous contrast agent. As we are using a pencil beam to probe the brain tissue, our method is best suited for brain ROI analysis. We used a high packing density of BSA to prepare our amyloid model and test the proposed method. Our method is, however, still relevant for detecting realistic levels of amyloid plaques in small animals. The scattering intensity can be improved by optimizing x-ray flux, beam size, and acquisition time. To locally detect the realistic level of amyloid plaques, we can 1) increase x-ray flux in 30 to 45 keV energy range by adjusting the tube current and voltage, 2) use 1 to 2 mm x-ray beam size by using larger pinholes and accounting for smearing effect, and 3) optimize measurement time considering the trade-off between radiation dose and signal-to-noise ratio. The major technical limitation we foresee is the radiation dose associated with long x-ray exposure time required to scan multiple sections of the brain or to scan a single animal several times over a short period of time for longitudinal studies. Since we are efficiently measuring x-ray scattering in angle- and energy-dispersive modes using a spectroscopic detector, we may be able to reduce the x-ray exposure time down to 60 seconds per irradiated location in the future.

Finally, we studied a transgenic mouse model of AD to unambiguously show

the applicability of our sSAXS method to detect amyloid plaques in small animals. The goal was to acquire the scattering signal specific to amyloid plaques for estimating amyloid burden within minutes with no contrast agents. We studied intact heads (excised) of 11 months old 5XFAD and WT mice and compared the results with the gold standard technique (histology) for validation. For sSAXS measurements in 30 to 45 keV energy range, we increased x-ray flux (2-mA tube current) and beam size (1 mm pinhole diameter) to reduce our measurement time to 300 s per irradiated location. Three locations covering isocortex and midbrain were studied in detail. We reported a strong correlation (Pearson $r = 0.94$, $P < 0.001$) between the ΔAUP calculated using our sSAXS method and the histology-derived amyloid load estimates. Our sSAXS method was sensitive enough to detect amyloid burden corresponding to an amyloid load as low as 3% based on histological analysis. By combining a polychromatic x-ray source with a 2D spectroscopic detector in a laboratory setting, the sSAXS approach enables amyloid burden estimation in an intact head of small animals. The method is relatively fast (a few minutes) to potentially be a convenient tool for the analysis of amyloid burden in small animals *in vivo*. We will now discuss the key challenges and opportunities for future investigations.

6.1 Developing a small-animal scanner

In the long term, a dedicated small-animal scanner can be developed as a preclinical research tool to readily estimate amyloid burden in the regions of in-

terest without contrast agents and non-invasively. The core technology will be based on using the sSAXS method that we specifically developed for an amyloid burden estimation application. We see this as a startup opportunity in a small-animal imaging market. Despite significant research investment in AD, there is no commercially available product that can quickly and accurately assess amyloid burden in live animals. Until now, measurements of amyloid burden in small animals require time-consuming postmortem histological analysis or resource-intensive imaging techniques such as PET. Transgenic animal models are used to understand disease progression better and test various diagnostics and therapeutic approaches. To track disease trajectory using histology, mice must be sacrificed at different stages of development, making longitudinal studies on individual animals impossible. PET remains challenging in mice due to non-specific binding of radioactive tracers and low sample throughput, not to mention the high operational cost to use it frequently. Therefore, to be a valuable research tool, our label-free method needs to provide consistent estimates of amyloid burden without sacrificing the animal in a few minutes per brain region. Having a short measurement time is necessary to reduce x-ray radiation, especially if we intend to scan the whole head with a pencil beam to map the amyloid burden. To build a small-animal scanner prototype beyond proof-of-concept, it is necessary to explore design options for a compact, table-top system and customize its capability depending on researcher needs and price points. One schematic design of a table-top scanner prototype is shown in Fig. 6.1. Possible customization options include types of the x-ray source and detector use, one-shot or scanning mode for amyloid mapping, acquisition speed and

data resolution for high-throughput analysis, and visualization of amyloid metrics. We also anticipate developing a user-friendly data analysis and reporting software for the scanner to be used by experts and non-experts alike. Our data analysis program for the proof-of-concept study was written in MATLAB. We expect to develop a graphical user interface using a open source software to intuitively follow the data analysis workflow and report amyloid burden metrics within a few clicks.

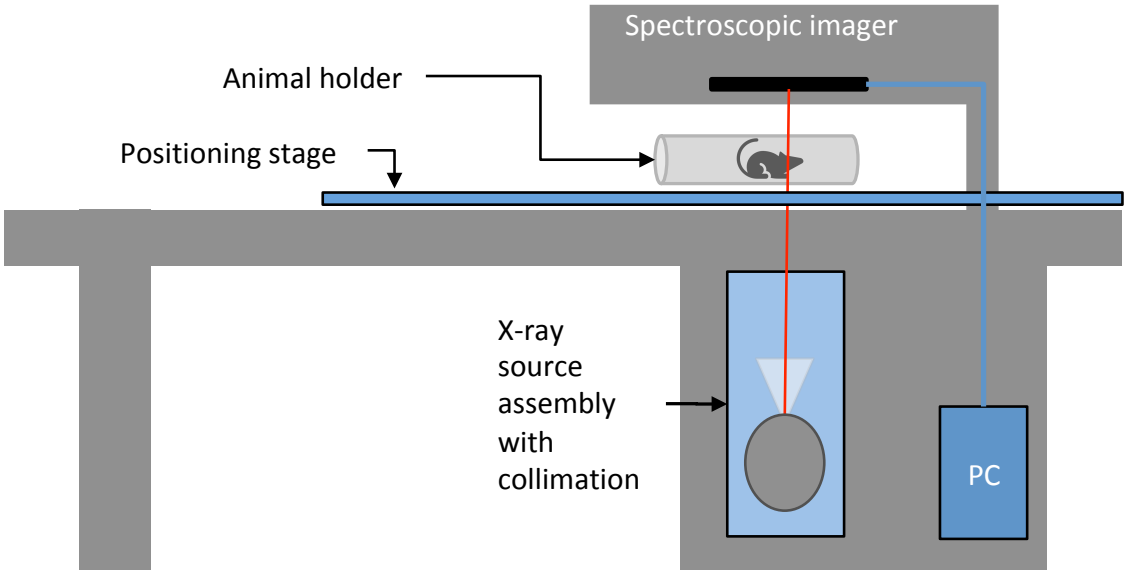


Figure 6.1: Schematic of one potential design of a small-animal scanner prototype that can be commercially developed.

A standardized metric should be able to tell amyloid negative or amyloid positive with high certainty and give the amyloid burden estimation on a scale of 0 to 1. ΔAUP represents the amyloid burden per location in our sSAXS method, where AUP is an area under the peak of the scattering profile from 3.6 to 8.4 nm^{-1}. We can scale this ΔAUP from 0 to 1 as

$$\Delta AUP_{standard} = \frac{AUP_i - \overline{AUP}_{WT}}{\overline{AUP}_{AD_{late}} - \overline{AUP}_{WT}}, \tag{6.1}$$

where AUP_i is the AUP in each location under investigation, $\overline{AUP}_{WT}$ is the mean of all ROIs in the WT mouse with no amyloid plaques, and $\overline{AUP}_{AD_{late}}$ is the mean of all ROIs in the 15 months or older AD mouse with high amyloid plaques. The concept here is to find minimum and maximum population-based AUP values, similar to the Centiloid metric used for standardizing amyloid PET data [62]. In our current work, we only studied excised mice heads with high amyloid load, and the sample size was small. Therefore, it is necessary to do age-dependent mice studies with a large sample size for both AD and WT mice. The measurement needs to be repeated at least three times per irradiated location at different time points. It is the only way to reliably develop a standardized metric for amyloid burden in sSAXS and thoroughly validate the prototype system for a wide range of amyloid plaque levels in the brain. Towards this effort, it may be useful to have a multi-year research collaboration with a lab that works on various mouse models of AD and provides us with mice samples.

We can perform an *in vivo* study by anesthetizing mice and positioning their head in a sample holder. The main cause of variability in AUP estimation will be the uncertainty in target localization when placing the mouse head in the x-ray beam. We can decrease the location uncertainty by taking a 2D or 3D scout image with the same detector in transmission mode before the sSAXS measurement. However, as with any x-ray technique, the radiation dose can be a limiting factor if long measurement time is used and if the dose is not optimized beforehand. The absorbed dose can be reduced by filtering low energy x-rays below 30 keV and using 60 seconds or less of exposure time. This needs to be done while maximizing elastic

scattering per absorbed dose if we want to get detectable scattering signals. The exposure time can be reduced in future studies by optimizing the system collimation and increasing photon counts in the 30 to 45 keV energy range. Due to the use of a spectroscopic detector, a polychromatic x-ray source with tunable voltage and current is adequate for increasing photon counts. We can use the generated x-ray flux in the energy range of interest without pre-filtering the energy spectrum. The low radiation dose in mice study is assumed to be 100 mGy or below [181]. In comparison, the upper limit for clinical head CT is about 60 to 80 mGy [182]. Since the energy range of x-rays can be tuned to probe thick samples, there is also an opportunity to use sSAXS to identify amyloid plaques in the human head.

6.2 Applications in humans

The x-ray energy range can be selected to maximize the elastic scattering signal per deposited energy with sample thickness [93]. Several Monte Carlo simulation studies have reported the feasibility of using higher energy x-rays between 50 to 120 keV to identify amyloid plaques in the human head [98, 173, 183]. Monte Carlo simulation was carried out using a publicly available MC-GPU, a GPU-accelerated x-ray transport simulation tool developed by our group [95,96]. This code simulates the transport of x-rays from source to detector and utilizes user-provided material cross-sections to describe x-ray interaction in a voxelized sample. In a recent simulation study, Ghammraoui et al. have used polychromatic x-rays from tungsten anode at 60 kV and a 2D energy-resolved photon-counting detector to detect the

large sized plaques (3 to 5 mm) in the 15 cm human brain phantom with 5 mm skull thickness [173]. As before, the amyloid specific scattering peaks around 6 and 13 nm^{-1} were used for amyloid plaques detection. By studying 3 to 5 mm plaque size, they also found a linear correlation between the recovered scattering intensity and the size of amyloid plaques. Therefore, detecting plaques and estimating its amount in an intact human head may be feasible using the sSAXS approach.

Nevertheless, the experimental study of the human head is more challenging than the mice study. This is mainly due to the size of the human head and the need to use high x-ray energies above 50 keV to get detectable scattering signal. The same laboratory prototype used for the mice study is not optimal for the human head phantom. The sample to detector distance needs to be increased to accommodate the head size and to cover the low q-regions with an increase in energy range. We may also need to increase the beam size up to 5 mm to probe large tissue volume and to decrease the measurement time. In a planar scanning setup, it is not feasible to know the location of plaques inside the brain along the x-ray path. To tackle location uncertainty, one useful approach could be to assume all plaques to be concentrated around the center of the brain and perform the analysis. This approach is similar to our WT mouse head study with an amyloid target embedded in the center. We found AUP for the center target to be 0.83 of the reference value. This underestimation issue may be more pronounced for the human head because of the increase in sample thickness by a factor of 10. For around 15 cm x-ray path length through the human head, uncertainty in q can easily be above 1 nm^{-1}. Thus, we need to carefully calibrate and correct the measured q-data with sample thickness

and target location. It is necessary to use a broad q-range for the estimation task instead of one peak position at a fixed q. In terms of sample, we are initially limited to phantom or cadaver studies for method demonstration. The amyloid model that we have developed for phantom studies will play a critical role to explore human application. In phantom studies, one can select ROIs in the brain to insert amyloid targets following Thal [30] or Braak [31] staging schemes.

6.3 Other applications

It is worth mentioning that amyloid plaques in the brain are present in a wide range of diseases and conditions [8,174,184], including Prion [185], Parkinson's [35], and traumatic brain injury [186]. Therefore, we can quickly diversify the application of our method in the future by using the same detection mechanism focusing on the scattering signal from β-sheet structures that locally increases in amyloid plaques [32]. Moreover, instead of studying only the brain, we may develop more accessible blood or cerebrospinal fluid (CSF) based biomarker of amyloids. The challenge is, however, to detect low concentration of biomarkers in fluids. For example, in AD, there is picogram per ml changes of Aβ levels in CSF [187]. Aβ42 presence in CSF is known to decrease with an increase in brain amyloid burden [187, 188]. As Aβ42 aggregates to form plaques in the brain, fewer Aβ42 peptides are left to diffuse into the CSF. The CSF samples are collected by lumbar puncture and usually analyzed using highly sensitive immunoassays. If sSAXS can detect any amyloid-specific signal from fluid analysis, we may be able to develop a non-invasive test of

spinal CSF without lumbar puncture. This will be a breakthrough for increasing patient comfort and compliance, and enabling repeated *in vivo* CSF analysis in a longitudinal study.

It is also worthwhile to expand the application of sSAXS beyond amyloid plaques. One significant research endeavor would be to detect neurofibrillary tau tangles in AD. Tangles are hyperphosphorylated tau protein aggregates that are formed later than amyloid plaques and cause neuronal degeneration [24, 25, 189]. They are strongly associated with cognitive decline in the late stage of AD progression. Tau has six isoforms with different conformations [190]. To detect tau tangle, we need to capture its distinct scattering signal in the accessible q-range. As with amyloid plaques, this scattering signal is usually the Bragg peaks associated with the periodic structure in the nanometer scale. Whether it is also the cross-β sheets in Tau aggregates [191] or any other molecular structure with well-defined d-spacing (d), we expect to see the scattering peak at q=2π/d. To experimentally identify amyloid plaques and tau tangles separately, we can study an AD mouse model such as 3xTg that forms plaques and tangles in an age-dependent manner [192]. In this work, I used 5XFAD model that rapidly develops amyloid pathology without tau aggregation to detect and quantify amyloid plaques only. Since it is possible to explore multiple applications covering small animals and humans beyond amyloid plaques, the outlook of the method that I have developed in my doctoral work looks promising.

Bibliography

[1] Geneviève Chêne, Alexa Beiser, Rhoda Au, Sarah R Preis, Philip A Wolf, Carole Dufouil, and Sudha Seshadri. Gender and incidence of dementia in the Framingham Heart Study from mid-adult life. *Alzheimer's & Dementia*, 11(3):310–320, 2015.

[2] Clifford R Jack Jr, David S Knopman, William J Jagust, Leslie M Shaw, Paul S Aisen, Michael W Weiner, Ronald C Petersen, and John Q Trojanowski. Hypothetical model of dynamic biomarkers of the Alzheimer's pathological cascade. *The Lancet Neurology*, 9(1):119–128, 2010.

[3] JH Hubbell and SM Seltzer. X-ray mass attenuation coefficients; NIST Standard Reference Database 126, 2004. DOI: `https://dx.doi.org/10.18434/T4D01F`.

[4] Daniel Franke and Dmitri I Svergun. DAMMIF, a program for rapid ab-initio shape determination in small-angle scattering. *Journal of Applied Crystallography*, 42(2):342–346, 2009.

[5] Jiliang Liu, Isabel Costantino, Nagarajan Venugopalan, Robert F Fischetti, Bradley T Hyman, Matthew P Frosch, Teresa Gomez-Isla, and Lee Makowski. Amyloid structure exhibits polymorphism on multiple length scales in human brain tissue. *Scientific Reports*, 6:33079, 2016.

[6] Lothar Gremer, Daniel Schölzel, Carla Schenk, Elke Reinartz, Jörg Labahn, Raimond BG Ravelli, Markus Tusche, Carmen Lopez-Iglesias, Wolfgang Hoyer, Henrike Heise, et al. Fibril structure of amyloid-β (1–42) by cryo–electron microscopy. *Science*, 358(6359):116–119, 2017.

[7] Allen Institute for Brain Science. Allen Adult Mouse Brain Atlas. *Online only*, 2020.

[8] Matthew G Iadanza, Matthew P Jackson, Eric W Hewitt, Neil A Ranson, and Sheena E Radford. A new era for understanding amyloid structures and disease. *Nature Reviews Molecular Cell Biology*, 19(12):755–773, 2018.

[9] Christopher A Ross and Michelle A Poirier. Protein aggregation and neurodegenerative disease. *Nature Medicine*, 10(7):S10–S17, 2004.

[10] 2020 Alzheimer's disease facts and figures. *Alzheimer's & Dementia*, 16(3):391–460, 2020.

[11] Liesi E Hebert, Jennifer Weuve, Paul A Scherr, and Denis A Evans. Alzheimer disease in the United States (2010–2050) estimated using the 2010 census. *Neurology*, 80(19):1778–1783, 2013.

[12] Jungsu Kim, Jacob M Basak, and David M Holtzman. The role of apolipoprotein E in Alzheimer's disease. *Neuron*, 63(3):287–303, 2009.

[13] Elizabeth H Corder, Ann M Saunders, Waren J Strittmatter, Donald E Schmechel, P Craig Gaskell, GWet Small, AD Roses, JL Haines, and Margaret A Pericak-Vance. Gene dose of apolipoprotein E type 4 allele and the risk of Alzheimer's disease in late onset families. *Science*, 261(5123):921–923, 1993.

[14] Xu-Qiao Chen and William C Mobley. Alzheimer disease pathogenesis: insights from molecular and cellular biology studies of oligomeric Aβ and tau species. *Frontiers in Neuroscience*, 13, 2019.

[15] Hanns Hippius and Gabriele Neundörfer. The discovery of Alzheimer's disease. *Dialogues in Clinical Neuroscience*, 5(1):101, 2003.

[16] Randall J Bateman, Chengjie Xiong, Tammie LS Benzinger, Anne M Fagan, Alison Goate, Nick C Fox, Daniel S Marcus, Nigel J Cairns, Xianyun Xie, Tyler M Blazey, et al. Clinical and biomarker changes in dominantly inherited Alzheimer's disease. *New England Journal of Medicine*, 367(9):795–804, 2012.

[17] Victor L Villemagne, Samantha Burnham, Pierrick Bourgeat, Belinda Brown, Kathryn A Ellis, Olivier Salvado, Cassandra Szoeke, S Lance Macaulay, Ralph Martins, Paul Maruff, et al. Amyloid β deposition, neurodegeneration, and cognitive decline in sporadic Alzheimer's disease: a prospective cohort study. *The Lancet Neurology*, 12(4):357–367, 2013.

[18] Ron Brookmeyer, Maria M Corrada, Frank C Curriero, and Claudia Kawas. Survival following a diagnosis of Alzheimer disease. *Archives of Neurology*, 59(11):1764–1767, 2002.

[19] Reisa A Sperling, Paul S Aisen, Laurel A Beckett, David A Bennett, Suzanne Craft, Anne M Fagan, Takeshi Iwatsubo, Clifford R Jack Jr, Jeffrey Kaye, Thomas J Montine, et al. Toward defining the preclinical stages of Alzheimer's disease: Recommendations from the National Institute on Aging-Alzheimer's Association workgroups on diagnostic guidelines for Alzheimer's disease. *Alzheimer's & Dementia*, 7(3):280–292, 2011.

[20] John Hardy and Dennis J Selkoe. The amyloid hypothesis of Alzheimer's disease: progress and problems on the road to therapeutics. *Science*, 297(5580):353–356, 2002.

[21] Marilyn S Albert, Steven T DeKosky, Dennis Dickson, Bruno Dubois, Howard H Feldman, Nick C Fox, Anthony Gamst, David M Holtzman, William J Jagust, Ronald C Petersen, et al. The diagnosis of mild cognitive impairment due to Alzheimer's disease: recommendations from the National Institute on Aging-Alzheimer's Association workgroups on diagnostic guidelines for Alzheimer's disease. *Alzheimer's & Dementia*, 7(3):270–279, 2011.

[22] Tian Qiu, Qian Liu, Yong-Xiang Chen, Yu-Fen Zhao, and Yan-Mei Li. Aβ42 and Aβ40: similarities and differences. *Journal of Peptide Science*, 21(7):522–529, 2015.

[23] W Henry, HW Querfurth, and FM LaFerla. Mechanisms of disease Alzheimer's disease. *New Engl J Med*, 362:329–44, 2010.

[24] Bernard J Hanseeuw, Rebecca A Betensky, Heidi IL Jacobs, Aaron P Schultz, Jorge Sepulcre, J Alex Becker, Danielle M Orozco Cosio, Michelle Farrell, Yakeel T Quiroz, Elizabeth C Mormino, et al. Association of amyloid and tau with cognition in preclinical Alzheimer disease: a longitudinal study. *JAMA Neurology*, 76(8):915–924, 2019.

[25] Chihiro Sato, Nicolas R Barthélemy, Kwasi G Mawuenyega, Bruce W Patterson, Brian A Gordon, Jennifer Jockel-Balsarotti, Melissa Sullivan, Matthew J Crisp, Tom Kasten, Kristopher M Kirmess, et al. Tau kinetics in neurons and the human central nervous system. *Neuron*, 97(6):1284–1298, 2018.

[26] Jan Näslund, Vahram Haroutunian, Richard Mohs, Kenneth L Davis, Peter Davies, Paul Greengard, and Joseph D Buxbaum. Correlation between elevated levels of amyloid β-peptide in the brain and cognitive decline. *JAMA*, 283(12):1571–1577, 2000.

[27] Panteleimon Giannakopoulos, FR Herrmann, Thierry Bussière, Constantin Bouras, Enikö Kövari, DP Perl, JH Morrison, Gabriel Gold, and PR Hof. Tangle and neuron numbers, but not amyloid load, predict cognitive status in Alzheimer's disease. *Neurology*, 60(9):1495–1500, 2003.

[28] Paulina V Arriagada, John H Growdon, E Tessa Hedley-Whyte, and Bradley T Hyman. Neurofibrillary tangles but not senile plaques parallel duration and severity of Alzheimer's disease. *Neurology*, 42(3):631–631, 1992.

[29] Heiko Braak and Eva Braak. Frequency of stages of Alzheimer-related lesions in different age categories. *Neurobiology of Aging*, 18(4):351–357, 1997.

[30] Dietmar R Thal, Udo Rüb, Mario Orantes, and Heiko Braak. Phases of Aβ-deposition in the human brain and its relevance for the development of AD. *Neurology*, 58(12):1791–1800, 2002.

[31] Heiko Braak and Eva Braak. Neuropathological stageing of Alzheimer-related changes. *Acta Neuropathologica*, 82(4):239–259, 1991.

[32] O Klementieva, K Willén, I Martinsson, B Israelsson, A Engdahl, J Cladera, P Uvdal, and GK Gouras. Pre-plaque conformational changes in Alzheimer's disease-linked Aβ and APP. *Nature Communications*, 8:14726, 2017.

[33] ED Eanes and George G Glenner. X-ray diffraction studies on amyloid filaments. *Journal of Histochemistry & Cytochemistry*, 16(11):673–677, 1968.

[34] Margaret Sunde and Colin CF Blake. From the globular to the fibrous state: protein structure and structural conversion in amyloid formation. *Quarterly Reviews of Biophysics*, 31(1):1–39, 1998.

[35] Katsuya Araki, Naoto Yagi, Koki Aoyama, Chi-Jing Choong, Hideki Hayakawa, Harutoshi Fujimura, Yoshitaka Nagai, Yuji Goto, and Hideki Mochizuki. Parkinson's disease is a type of amyloidosis featuring accumulation of amyloid fibrils of α-synuclein. *Proceedings of the National Academy of Sciences*, 116(36):17963–17969, 2019.

[36] Catherine R Liao, Margaret Rak, Jillian Lund, Miriam Unger, Eric Platt, Benedict C Albensi, Carol J Hirschmugl, and Kathleen M Gough. Synchrotron FTIR reveals lipid around and within amyloid plaques in transgenic mice and Alzheimer's disease brain. *Analyst*, 138(14):3991–3997, 2013.

[37] Lin-P'ing Choo, David L Wetzel, William C Halliday, Michael Jackson, Steven M LeVine, and Henry H Mantsch. In situ characterization of beta-amyloid in Alzheimer's diseased tissue by synchrotron Fourier transform infrared microspectroscopy. *Biophysical Journal*, 71(4):1672–1679, 1996.

[38] Lisa M Miller, Qi Wang, Tejas P Telivala, Randy J Smith, Antonio Lanzirotti, and Judit Miklossy. Synchrotron-based infrared and x-ray imaging shows focalized accumulation of Cu and Zn co-localized with β-amyloid deposits in Alzheimer's disease. *Journal of Structural Biology*, 155(1):30–37, 2006.

[39] Alberto Serrano-Pozo, Matthew L Mielke, Alona Muzitansky, Teresa Gómez-Isla, John H Growdon, Brian J Bacskai, Rebecca A Betensky, Matthew P Frosch, and Bradley T Hyman. Stable size distribution of amyloid plaques over the course of Alzheimer disease. *Journal of Neuropathology & Experimental Neurology*, 71(8):694–701, 2012.

[40] Thomas Liebmann, Nicolas Renier, Karima Bettayeb, Paul Greengard, Marc Tessier-Lavigne, and Marc Flajolet. Three-dimensional study of Alzheimer's disease hallmarks using the iDISCO clearing method. *Cell Reports*, 16(4):1138–1152, 2016.

[41] Shu Wang, Bingbing Lin, Guimin Lin, Caihong Sun, Ruolan Lin, Jia Huang, Jing Tao, Xingfu Wang, Yunkun Wu, Lidian Chen, et al. Label-free multiphoton imaging of β-amyloid plaques in Alzheimer's disease mouse models. *Neurophotonics*, 6(4):045008, 2019.

[42] Jinghui Dong, Raquel Revilla-Sanchez, Stephen Moss, and Philip G Haydon. Multiphoton in vivo imaging of amyloid in animal models of Alzheimer's disease. *Neuropharmacology*, 59(4-5):268–275, 2010.

[43] William E Klunk, Brian J Bacskai, Chester A Mathis, Stephen T Kajdasz, Megan E McLellan, Matthew P Frosch, Manik L Debnath, Daniel P Holt, Yanming Wang, and Bradley T Hyman. Imaging Aβ plaques in living transgenic mice with multiphoton microscopy and methoxy-x04, a systemically administered Congo red derivative. *Journal of Neuropathology & Experimental Neurology*, 61(9):797–805, 2002.

[44] Sabine Liebscher and Melanie Meyer-Luehmann. A peephole into the brain: neuropathological features of Alzheimer's disease revealed by in vivo two-photon imaging. *Frontiers in Psychiatry*, 3:26, 2012.

[45] Melanie Meyer-Luehmann, Tara L Spires-Jones, Claudia Prada, Monica Garcia-Alloza, Alix De Calignon, Anete Rozkalne, Jessica Koenigsknecht-Talboo, David M Holtzman, Brian J Bacskai, and Bradley T Hyman. Rapid appearance and local toxicity of amyloid-β plaques in a mouse model of Alzheimer's disease. *Nature*, 451(7179):720–724, 2008.

[46] Hiroki R Ueda, Ali Ertürk, Kwanghun Chung, Viviana Gradinaru, Alain Chédotal, Pavel Tomancak, and Philipp J Keller. Tissue clearing and its applications in neuroscience. *Nature Reviews Neuroscience*, pages 1–19, 2020.

[47] Hameetha B Rajamohamedsait and Einar M Sigurdsson. Histological staining of amyloid and pre-amyloid peptides and proteins in mouse tissue. In *Amyloid Proteins*, pages 411–424. Springer, 2012.

[48] Christopher C Rowe and Victor L Villemagne. Brain amyloid imaging. *Journal of Nuclear Medicine Technology*, 41(1):11–18, 2013.

[49] Elizabeth Morris, Anastasia Chalkidou, Alexander Hammers, Janet Peacock, Jennifer Summers, and Stephen Keevil. Diagnostic accuracy of ^{18}F amyloid PET tracers for the diagnosis of Alzheimer's disease: a systematic review and meta-analysis. *European Journal of Nuclear Medicine and Molecular Imaging*, 43(2):374–385, 2016.

[50] Tamara F Lundeen, John P Seibyl, Matthew F Covington, Naghmehossadat Eshghi, and Phillip H Kuo. Signs and artifacts in amyloid PET. *Radiographics*, 38(7):2123–2133, 2018.

[51] Louise Rice and Sotirios Bisdas. The diagnostic value of FDG and amyloid PET in Alzheimer's disease—A systematic review. *European Journal of Radiology*, 94:16–24, 2017.

[52] Matthias Brendel, Anna Jaworska, Eric Grießinger, Christina Rötzer, Steffen Burgold, Franz-Josef Gildehaus, Janette Carlsen, Paul Cumming, Karlheinz Baumann, Christian Haass, et al. Cross-sectional comparison of small animal [18F]-florbetaben amyloid-PET between transgenic AD mouse models. *PloS One*, 10(2), 2015.

[53] Anniina Snellman, Francisco R López-Picón, Johanna Rokka, Mario Salmona, Gianluigi Forloni, Mika Scheinin, Olof Solin, Juha O Rinne, and Merja Haaparanta-Solin. Longitudinal amyloid imaging in mouse brain with 11C-PIB: comparison of APP23, Tg2576, and APPswe-PS1dE9 mouse models of Alzheimer disease. *Journal of Nuclear Medicine*, 54(8):1434–1441, 2013.

[54] Hiroshi Toyama, Daniel Ye, Masanori Ichise, Jeih-San Liow, Lisheng Cai, David Jacobowitz, John L Musachio, Jinsoo Hong, Mathew Crescenzo, Dnyanesh Tipre, et al. Pet imaging of brain with the β-amyloid probe,[11 C] 6-OH-BTA-1, in a transgenic mouse model of Alzheimer's disease. *European Journal of Nuclear Medicine and Molecular Imaging*, 32(5):593–600, 2005.

[55] William E Klunk, Brian J Lopresti, Milos D Ikonomovic, Iliya M Lefterov, Radosveta P Koldamova, Eric E Abrahamson, Manik L Debnath, Daniel P Holt, Guo-feng Huang, Li Shao, et al. Binding of the positron emission tomography tracer Pittsburgh compound-B reflects the amount of amyloid-β in Alzheimer's disease brain but not in transgenic mouse brain. *Journal of Neuroscience*, 25(46):10598–10606, 2005.

[56] William E Klunk, Henry Engler, Agneta Nordberg, Yanming Wang, Gunnar Blomqvist, Daniel P Holt, Mats Bergström, Irina Savitcheva, Guo-Feng Huang, Sergio Estrada, et al. Imaging brain amyloid in Alzheimer's disease with Pittsburgh Compound-B. *Annals of Neurology*, 55(3):306–319, 2004.

[57] MA Mintun, GN Larossa, YI Sheline, CS Dence, S Yoon Lee, RH Mach, WE Klunk, CA Mathis, ST DeKosky, and JC Morris. [^{11}C] PIB in a nondemented population potential antecedent marker of Alzheimer disease. *Neurology*, 67(3):446–452, 2006.

[58] John C Morris, Catherine M Roe, Elizabeth A Grant, Denise Head, Martha Storandt, Alison M Goate, Anne M Fagan, David M Holtzman, and Mark A Mintun. Pittsburgh compound B imaging and prediction of progression from cognitive normality to symptomatic Alzheimer disease. *Archives of Neurology*, 66(12):1469–1475, 2009.

[59] Christopher C Rowe, Pierrick Bourgeat, Kathryn A Ellis, Belinda Brown, Yen Ying Lim, Rachel Mulligan, Gareth Jones, Paul Maruff, Michael Woodward, Roger Price, et al. Predicting Alzheimer disease with β-amyloid imaging: Results from the Australian imaging, biomarkers, and lifestyle study of ageing. *Annals of Neurology*, 74(6):905–913, 2013.

[60] Christopher C Rowe, Uwe Ackerman, William Browne, Rachel Mulligan, Kerryn L Pike, Graeme O'Keefe, Henry Tochon-Danguy, Gordon Chan, Salvatore U Berlangieri, Gareth Jones, et al. Imaging of amyloid β in alzheimer's disease with ^{18}F-bay94-9172, a novel PET tracer: proof of mechanism. *The Lancet Neurology*, 7(2):129–135, 2008.

[61] Craig Curtis, Jose E Gamez, Upinder Singh, Carl H Sadowsky, Teresa Villena, Marwan N Sabbagh, Thomas G Beach, Ranjan Duara, Adam S Fleisher, Kirk A Frey, et al. Phase 3 trial of flutemetamol labeled with radioactive fluorine 18 imaging and neuritic plaque density. *JAMA Neurology*, 72(3):287–294, 2015.

[62] William E Klunk, Robert A Koeppe, Julie C Price, Tammie L Benzinger, Michael D Devous Sr, William J Jagust, Keith A Johnson, Chester A Mathis, Davneet Minhas, Michael J Pontecorvo, et al. The Centiloid Project: standardizing quantitative amyloid plaque estimation by PET. *Alzheimer's & Dementia*, 11(1):1–15, 2015.

[63] Clifford R Jack Jr, Michael Garwood, Thomas M Wengenack, Bret Borowski, Geoffrey L Curran, Joseph Lin, Gregor Adriany, Olli HJ Gröhn, Roger Grimm, and Joseph F Poduslo. In vivo visualization of Alzheimer's amyloid plaques by magnetic resonance imaging in transgenic mice without a contrast agent. *Magnetic Resonance in Medicine: An Official Journal of the International Society for Magnetic Resonance in Medicine*, 52(6):1263–1271, 2004.

[64] Helene Benveniste, Gillian Einstein, Katie R Kim, Christine Hulette, and G Allan Johnson. Detection of neuritic plaques in alzheimer's disease by magnetic resonance microscopy. *Proceedings of the National Academy of Sciences*, 96(24):14079–14084, 1999.

[65] Marc Dhenain, Nicolas Privat, Charles Duyckaerts, and Russell E Jacobs. Senile plaques do not induce susceptibility effects in T2*-weighted MR microscopic images. *NMR in Biomedicine: An International Journal Devoted to the Development and Application of Magnetic Resonance In Vivo*, 15(3):197–203, 2002.

[66] Youssef Zaim Wadghiri, Einar M Sigurdsson, Marcin Sadowski, James I Elliott, Yongsheng Li, Henrieta Scholtzova, Cheuk Ying Tang, Gilbert Aguinaldo, Miguel Pappolla, Karen Duff, et al. Detection of Alzheimer's amyloid in transgenic mice using magnetic resonance microimaging. *Magnetic Resonance in Medicine: An Official Journal of the International Society for Magnetic Resonance in Medicine*, 50(2):293–302, 2003.

[67] Clémence Dudeffant, Matthias Vandesquille, Kelly Herbert, Clément M Garin, Sandro Alves, Véronique Blanchard, Emmanuel E Comoy, Fanny Petit, and Marc Dhenain. Contrast-enhanced MR microscopy of amyloid plaques in five mouse models of amyloidosis and in human Alzheimer's disease brains. *Scientific Reports*, 7(1):4955, 2017.

[68] K Noda-Saita, A Yoneyama, Y Shitaka, Y Hirai, K Terai, J Wu, T Takeda, K Hyodo, N Osakabe, T Yamaguchi, et al. Quantitative analysis of amyloid plaques in a mouse model of Alzheimer's disease by phase-contrast x-ray computed tomography. *Neuroscience*, 138(4):1205–1213, 2006.

[69] BR Pinzer, M Cacquevel, Peter Modregger, SA McDonald, JC Bensadoun, T Thuering, P Aebischer, and Marco Stampanoni. Imaging brain amyloid deposition using grating-based differential phase contrast tomography. *Neuroimage*, 61(4):1336–1346, 2012.

[70] Alberto Astolfo, Aurélien Lathuiliere, Vanessa Laversenne, Bernard Schneider, and Marco Stampanoni. Amyloid-β plaque deposition measured using propagation-based x-ray phase contrast CT imaging. *Journal of Synchrotron Radiation*, 23(3):813–819, 2016.

[71] Mareike Töpperwien, Franziska van der Meer, Christine Stadelmann, and Tim Salditt. Correlative x-ray phase-contrast tomography and histology of human brain tissue affected by Alzheimer's disease. *NeuroImage*, page 116523, 2020.

[72] Linda CP Croton, Kaye S Morgan, David M Paganin, Lauren T Kerr, Megan J Wallace, Kelly J Crossley, Suzanne L Miller, Naoto Yagi, Kentaro Uesugi, Stuart B Hooper, et al. In situ phase contrast x-ray brain CT. *Scientific Reports*, 8(1):1–12, 2018.

[73] Eshan Dahal, Andreu Badal, Ahmed Zidan, Alaadin Alayoubi, Tomoe Hagio, Stephen Glick, Aldo Badano, and Bahaa Ghammraoui. Stable gelatin-based phantom materials with tunable x-ray attenuation properties and 3D printability for x-ray imaging. *Physics in Medicine & Biology*, 2018.

[74] JH Hubbell, Wm J Veigele, EA Briggs, RT Brown, DT Cromer, and d RJ Howerton. Atomic form factors, incoherent scattering functions, and photon scattering cross sections. *Journal of physical and chemical reference data*, 4(3):471–538, 1975.

[75] William J Veigele, Philip T Tracy, and E Michael Henry. Compton effect and electron binding. *American Journal of Physics*, 34(12):1116–1121, 1966.

[76] Otto Glatter and Otto Kratky. *Small angle X-ray scattering*. Academic press, 1982.

[77] Tao Li, Andrew J. Senesi, and Byeongdu Lee. Small angle x-ray scattering for nanoparticle research. *Chemical Reviews*, 116(18):11128–11180, 2016.

[78] Dmitri I Svergun and Michel HJ Koch. Small-angle scattering studies of biological macromolecules in solution. *Reports on Progress in Physics*, 66(10):1735, 2003.

[79] Cristiano Luis Pinto Oliveira. Investigating macromolecular complexes in solution by small angle x-ray scattering. In *Current Trends in X-Ray Crystallography*, chapter 16. IntechOpen, 2011.

[80] OTTO Glatter. A new method for the evaluation of small-angle scattering data. *Journal of Applied Crystallography*, 10(5):415–421, 1977.

[81] P Kraft, A Bergamaschi, Ch Broennimann, R Dinapoli, EF Eikenberry, B Henrich, I Johnson, A Mozzanica, CM Schlepütz, PR Willmott, et al. Performance of single-photon-counting PILATUS detector modules. *Journal of Synchrotron Radiation*, 16(3):368–375, 2009.

[82] Tobias W Gräwert and Dmitri I Svergun. Structural modeling using solution small-angle x-ray scattering (SAXS). *Journal of Molecular Biology*, 2020.

[83] Andreas Förster, Stefan Brandstetter, and Clemens Schulze-Briese. Transforming x-ray detection with hybrid photon counting detectors. *Philosophical Transactions of the Royal Society A*, 377(2147):20180241, 2019.

[84] Doris Orthaber, Alexander Bergmann, and Otto Glatter. SAXS experiments on absolute scale with kratky systems using water as a secondary standard. *Journal of Applied Crystallography*, 33(2):218–225, 2000.

[85] Fan Zhang, Jan Ilavsky, Gabrielle G Long, John PG Quintana, Andrew J Allen, and Pete R Jemian. Glassy carbon as an absolute intensity calibration standard for small-angle scattering. *Metallurgical and Materials Transactions A*, 41(5):1151–1158, 2010.

[86] O Bunk, M Bech, TH Jensen, R Feidenhans, T Binderup, A Menzel, and F Pfeiffer. Multimodal x-ray scatter imaging. *New Journal of Physics*, 11(12):123016, 2009.

[87] Marianne Liebi, Marios Georgiadis, Andreas Menzel, Philipp Schneider, Joachim Kohlbrecher, Oliver Bunk, and Manuel Guizar-Sicairos. Nanostructure surveys of macroscopic specimens by small-angle scattering tensor tomography. *Nature*, 527(7578):349, 2015.

[88] Florian Schaff, Martin Bech, Paul Zaslansky, Christoph Jud, Marianne Liebi, Manuel Guizar-Sicairos, and Franz Pfeiffer. Six-dimensional real and reciprocal space small-angle x-ray scattering tomography. *Nature*, 527(7578):353, 2015.

[89] Torben H Jensen, Martin Bech, Oliver Bunk, Andreas Menzel, Audrey Bouchet, Geraldine Le Duc, Robert Feidenhans, and Franz Pfeiffer. Molecular

x-ray computed tomography of myelin in a rat brain. *NeuroImage*, 57(1):124–129, 2011.

[90] Nicholas Allec, Mina Choi, Nikhil Yesupriya, Brian Szychowski, Michael R White, Maricel G Kann, Elsa D Garcin, Marie-Christine Daniel, and Aldo Badano. Small-angle x-ray scattering method to characterize molecular interactions: Proof of concept. *Scientific Reports*, 5:12085, 2015.

[91] Nadia Alam, Mina Choi, Bahaa Ghammraoui, Eshan Dahal, and Aldo Badano. Small-angle x-ray scattering cross-section measurements of imaging materials. *Biomedical Physics & Engineering Express*, 3(2):025023, 2017.

[92] M Choi and A Badano. Planar small-angle x-ray scattering imaging of phantoms and biological samples. *Applied Physics Letters*, 110(15):153106, 2017.

[93] Mina Choi, Bahaa Ghammraoui, Andreu Badal, and Aldo Badano. Monte Carlo x-ray transport simulation of small-angle x-ray scattering instruments using measured sample cross sections. *Journal of Applied Crystallography*, 49(1):188–194, 2016.

[94] Mina Choi, Bahaa Ghammraoui, and Aldo Badano. Small-angle x-ray scattering characteristics of mouse brain: Planar imaging measurements and tomographic imaging simulations. *PloS One*, 12(10):e0186451, 2017.

[95] Andreu Badal and Aldo Badano. Accelerating Monte Carlo simulations of photon transport in a voxelized geometry using a massively parallel graphics processing unit. *Medical Physics*, 36(11):4878–4880, 2009.

[96] Bahaa Ghammraoui and Andreu Badal. Monte Carlo simulation of novel breast imaging modalities based on coherent x-ray scattering. *Physics in Medicine & Biology*, 59(13):3501, 2014.

[97] Mina Choi. *Feasibility of in Vivo SAXS Imaging for Detection of Alzheimer's Disease*. PhD thesis, University of Maryland, College Park, 2017.

[98] Mina Choi, Eshan Dahal, and Aldo Badano. Feasibility of imaging amyloid in the brain using small-angle x-ray scattering. *Biomedical Physics & Engineering Express*, 2019.

[99] JM Schultz and TC Long. Energy-scanning small-angle x-ray scattering: polyethylene. *Journal of Materials Science*, 10(4):567–570, 1975.

[100] J Bordas, IH Munro, and AM Glazer. Small-angle scattering experiments on biological materials using synchrotron radiation. *Nature*, 262(5569):541–545, 1976.

[101] Kuan-Li Yu, Chih-Hao Lee, Ching-Shiang Hwang, Huan-Chi Tseng, Poh-Kun Tseng, Tsang-Lang Lin, Szu-Li Chang, Rong-Jiun Sheu, and Sow-Hsin Chen. Study of the capability of energy dispersive small angle x-ray scattering with

synchrotron radiation. *Review of Scientific Instruments*, 70(8):3233–3238, 1999.

[102] Giuseppe Portale, Alessandro Longo, Lucio D'Ilario, Andrea Martinelli, and Ruggero Caminiti. Energy-dispersive small-angle x-ray scattering for investigating polymer morphology: Static and time-resolved experiments. *Applied Physics Letters*, 85(20):4798–4800, 2004.

[103] Giuseppe Portale, Alessandro Longo, Lucio D'Ilario, Andrea Martinelli, Ruggero Caminiti, and Valerio Rossi Albertini. Small-angle energy-dispersive x-ray scattering using a laboratory-based diffractometer with a conventional source. *Journal of Applied Crystallography*, 40(2):218–231, 2007.

[104] Fangzuo Li, Zhiguo Liu, and Tianxi Sun. Energy-dispersive small-angle x-ray scattering with cone collimation using x-ray capillary optics. *Review of Scientific Instruments*, 87(9):093106, 2016.

[105] Paul Seller, S Bell, RJ Cernik, C Christodoulou, CK Egan, JA Gaskin, S Jacques, S Pani, BD Ramsey, C Reid, et al. Pixellated Cd (Zn) Te high-energy x-ray instrument. *Journal of Instrumentation*, 6(12):C12009, 2011.

[106] MC Veale, P Seller, M Wilson, and E Liotti. HEXITEC: a high-energy x-ray spectroscopic imaging detector for synchrotron applications. *Synchrotron Radiation News*, 31(6):28–32, 2018.

[107] MD Wilson, L Dummott, Diana D Duarte, FH Green, Silvia Pani, Andreas Schneider, JW Scuffham, Paul Seller, and MC Veale. A 10 cm× 10 cm CdTe spectroscopic imaging detector based on the HEXITEC ASIC. *Journal of Instrumentation*, 10(10):P10011, 2015.

[108] D O'Flynn, CB Reid, C Christodoulou, MD Wilson, MC Veale, P Seller, D Hills, H Desai, B Wong, and R Speller. Explosive detection using pixellated x-ray diffraction (PixD). *Journal of Instrumentation*, 8(03):P03007, 2013.

[109] Robert Moss, Chiaki Crews, Matthew Wilson, and Robert Speller. miniPixD: a compact sample analysis system which combines x-ray imaging and diffraction. *Journal of Instrumentation*, 12(02):P02001, 2017.

[110] Robert M Moss, Amany S Amin, Chiaki Crews, Colin A Purdie, Lee B Jordan, Francesco Iacoviello, Andrew Evans, Robert D Speller, and Sarah J Vinnicombe. Correlation of x-ray diffraction signatures of breast tissue and their histopathological classification. *Scientific Reports*, 7(1):1–9, 2017.

[111] JR Rhodes. Radioisotope x-ray spectrometry. a review. *Analyst*, 91(1088):683–699, 1966.

[112] Tadayuki Takahashi and Shin Watanabe. Recent progress in CdTe and CdZnTe detectors. *IEEE Transactions on Nuclear Science*, 48(4):950–959, 2001.

[113] Liqiang Ren, Bin Zheng, and Hong Liu. Tutorial on x-ray photon counting detector characterization. *Journal of X-ray Science and Technology*, 26(1):1–28, 2018.

[114] SL Bugby, KA Koch-Mehrin, MC Veale, MD Wilson, and JE Lees. Energy-loss correction in charge sharing events for improved performance of pixellated compound semiconductors. *Nuclear Instruments and Methods in Physics Research Section A: Accelerators, Spectrometers, Detectors and Associated Equipment*, 940:142–151, 2019.

[115] L Abbene, G Gerardi, and F Principato. Digital performance improvements of a CdTe pixel detector for high flux energy-resolved x-ray imaging. *Nuclear Instruments and Methods in Physics Research Section A: Accelerators, Spectrometers, Detectors and Associated Equipment*, 777:54–62, 2015.

[116] Stefano Del Sordo, Leonardo Abbene, Ezio Caroli, Anna Maria Mancini, Andrea Zappettini, and Pietro Ubertini. Progress in the development of CdTe and CdZnTe semiconductor radiation detectors for astrophysical and medical applications. *Sensors*, 9(5):3491–3526, 2009.

[117] Zhong He. Review of the Shockley–Ramo theorem and its application in semiconductor gamma-ray detectors. *Nuclear Instruments and Methods in Physics Research Section A: Accelerators, Spectrometers, Detectors and Associated Equipment*, 463(1-2):250–267, 2001.

[118] Lawrence Jones, Paul Seller, Matthew Wilson, and Alec Hardie. HEXITEC ASIC—a pixellated readout chip for CZT detectors. *Nuclear Instruments and Methods in Physics Research Section A: Accelerators, Spectrometers, Detectors and Associated Equipment*, 604(1-2):34–37, 2009.

[119] Matthew David Wilson, Robert Cernik, Henry Chen, Conny Hansson, Kris Iniewski, Lawrence L Jones, Paul Seller, and Matthew C Veale. Small pixel CZT detector for hard x-ray spectroscopy. *Nuclear Instruments and Methods in Physics Research Section A: Accelerators, Spectrometers, Detectors and Associated Equipment*, 652(1):158–161, 2011.

[120] Katsuyuki Taguchi and Jan S Iwanczyk. Vision 20/20: Single photon counting x-ray detectors in medical imaging. *Medical Physics*, 40(10), 2013.

[121] Katsuyuki Taguchi. Energy-sensitive photon counting detector-based x-ray computed tomography. *Radiological Physics and Technology*, 10(1):8–22, 2017.

[122] Yuan Fang, Cheng Xu, Yuan Yao, Norbert Pelc, Mats Danielsson, and Aldo Badano. Modeling charge transport in photon-counting detectors. *Nuclear Instruments and Methods in Physics Research Section A: Accelerators, Spectrometers, Detectors and Associated Equipment*, 899:115–121, 2018.

[123] MC Veale, SJ Bell, DD Duarte, A Schneider, P Seller, MD Wilson, and K Iniewski. Measurements of charge sharing in small pixel CdTe detectors. *Nuclear Instruments and Methods in Physics Research Section A: Accelerators, Spectrometers, Detectors and Associated Equipment*, 767:218–226, 2014.

[124] MC Veale, SJ Bell, P Seller, MD Wilson, and V Kachkanov. X-ray microbeam characterization of a small pixel spectroscopic CdTe detector. *Journal of Instrumentation*, 7(07):P07017, 2012.

[125] Katsuyuki Taguchi, Christoph Polster, Okkyun Lee, Karl Stierstorfer, and Steffen Kappler. Spatio-energetic cross talk in photon counting detectors: Detector model and correlated poisson data generator. *Medical Physics*, 43(12):6386–6404, 2016.

[126] M De Felici, R Felici, C Ferrero, A Tartari, M Gambaccini, and S Finet. Structural characterization of the human cerebral myelin sheath by small angle x-ray scattering. *Physics in Medicine & Biology*, 53(20):5675, 2008.

[127] Marios Georgiadis, Manuel Guizar-Sicairos, Alexander Zwahlen, Andreas J Trüssel, Oliver Bunk, Ralph Müller, and Philipp Schneider. 3D scanning SAXS: a novel method for the assessment of bone ultrastructure orientation. *Bone*, 71:42–52, 2015.

[128] D O'Flynn, C Crews, I Drakos, C Christodoulou, MD Wilson, MC Veale, P Seller, and RD Speller. Materials identification using a small-scale pixellated x-ray diffraction system. *Journal of Physics D: Applied Physics*, 49(17):175304, 2016.

[129] Grethe Vestergaard Jensen and John George Barker. Effects of multiple scattering encountered for various small-angle scattering model functions. *Journal of Applied Crystallography*, 51(5), 2018.

[130] CG Schroer, M Kuhlmann, SV Roth, R Gehrke, N Stribeck, A Almendarez-Camarillo, and B Lengeler. Mapping the local nanostructure inside a specimen by tomographic small-angle x-ray scattering. *Applied Physics Letters*, 88(16):164102, 2006.

[131] S Pani, EJ Cook, JA Horrocks, JL Jones, and RD Speller. Characterization of breast tissue using energy-dispersive x-ray diffraction computed tomography. *Applied Radiation and Isotopes*, 68(10):1980–1987, 2010.

[132] Bahaa Ghammraoui and Lucretiu M Popescu. Non-invasive classification of breast microcalcifications using x-ray coherent scatter computed tomography. *Physics in Medicine & Biology*, 62(3):1192, 2017.

[133] James A Silas and Eric W Kaler. Effect of multiple scattering on SANS spectra from bicontinuous microemulsions. *Journal of Colloid and Interface Science*, 257(2):291–298, 2003.

[134] Agostino Tartari, Ernesto Casnati, Claudio Bonifazzi, and Claudio Baraldi. Molecular differential cross sections for x-ray coherent scattering in fat and polymethyl methacrylate. *Physics in Medicine & Biology*, 42(12):2551, 1997.

[135] Mahiuddin Ahmed, Judianne Davis, Darryl Aucoin, Takeshi Sato, Shivani Ahuja, Saburo Aimoto, James I Elliott, William E Van Nostrand, and Steven O Smith. Structural conversion of neurotoxic amyloid-β 1–42 oligomers to fibrils. *Nature Structural and Molecular Biology*, 17(5):561, 2010.

[136] Lukasz Goldschmidt, Poh K Teng, Roland Riek, and David Eisenberg. Identifying the amylome, proteins capable of forming amyloid-like fibrils. *Proceedings of the National Academy of Sciences*, 107(8):3487–3492, 2010.

[137] Koichi Murayama and Mihoko Tomida. Heat-induced secondary structure and conformation change of bovine serum albumin investigated by Fourier transform infrared spectroscopy. *Biochemistry*, 43(36):11526–11532, 2004.

[138] Nikolaj K Holm, Stine K Jespersen, Lise V Thomassen, Tine Y Wolff, Pankaj Sehgal, Line A Thomsen, Gunna Christiansen, Christian Beyschau Andersen, Anders D Knudsen, and Daniel E Otzen. Aggregation and fibrillation of bovine serum albumin. *Biochimica et Biophysica Acta (BBA)-Proteins and Proteomics*, 1774(9):1128–1138, 2007.

[139] Mily Bhattacharya, Neha Jain, and Samrat Mukhopadhyay. Insights into the mechanism of aggregation and fibril formation from bovine serum albumin. *The Journal of Physical Chemistry B*, 115(14):4195–4205, 2011.

[140] F Grant Pearce, Sarah H Mackintosh, and Juliet A Gerrard. Formation of amyloid-like fibrils by ovalbumin and related proteins under conditions relevant to food processing. *Journal of Agricultural and Food Chemistry*, 55(2):318–322, 2007.

[141] Nikolaj K Holm, Stine K Jespersen, Lise V Thomassen, Tine Y Wolff, Pankaj Sehgal, Line A Thomsen, Gunna Christiansen, Christian Beyschau Andersen, Anders D Knudsen, and Daniel E Otzen. Aggregation and fibrillation of bovine serum albumin. *Biochimica et Biophysica Acta (BBA) - Proteins and Proteomics*, 1774(9):1128 – 1138, 2007.

[142] Fajun Zhang, Maximilian WA Skoda, Robert MJ Jacobs, Richard A Martin, Christopher M Martin, and Frank Schreiber. Protein interactions studied by SAXS: effect of ionic strength and protein concentration for BSA in aqueous solutions. *The Journal of Physical Chemistry B*, 111(1):251–259, 2007.

[143] Maxim V Petoukhov, Daniel Franke, Alexander V Shkumatov, Giancarlo Tria, Alexey G Kikhney, Michal Gajda, Christian Gorba, Haydyn DT Mertens, Petr V Konarev, and Dmitri I Svergun. New developments in the ATSAS program package for small-angle scattering data analysis. *Journal of Applied Crystallography*, 45(2):342–350, 2012.

[144] Sophya Breedlove, Jasson Crentsil, Eshan Dahal, and Aldo Badano. Small-angle x-ray scattering characterization of a β-amyloid model in phantoms. *BMC Research Notes*, 13(1):1–5, 2020.

[145] Petrea Frid, Sergey V Anisimov, and Natalija Popovic. Congo red and protein aggregation in neurodegenerative diseases. *Brain Research Reviews*, 53(1):135–160, 2007.

[146] Charles H Vannoy and Roger M Leblanc. Effects of DHLA-capped CdSe/ZnS quantum dots on the fibrillation of human serum albumin. *The Journal of Physical Chemistry B*, 114(33):10881–10888, 2010.

[147] William E Klunk, Robert F Jacob, and R Preston Mason. Quantifying amyloid β-peptide (Aβ) aggregation using the Congo Red-Aβ (CR–Aβ) spectrophotometric assay. *Analytical Biochemistry*, 266(1):66–76, 1999.

[148] Chun Wu, Zhixiang Wang, Hongxing Lei, Wei Zhang, and Yong Duan. Dual binding modes of congo red to amyloid protofibril surface observed in molecular dynamics simulations. *Journal of the American Chemical Society*, 129(5):1225–1232, 2007.

[149] Sean A Hudson, Heath Ecroyd, Tak W Kee, and John A Carver. The thioflavin T fluorescence assay for amyloid fibril detection can be biased by the presence of exogenous compounds. *The FEBS Journal*, 276(20):5960–5972, 2009.

[150] William E Klunk, Robert F Jacob, and R Preston Mason. [19] Quantifying amyloid by congo red spectral shift assay. In *Methods in Enzymology*, volume 309, pages 285–305. Elsevier, 1999.

[151] Michel HJ Koch, Patrice Vachette, and Dmitri I Svergun. Small-angle scattering: a view on the properties, structures and structural changes of biological macromolecules in solution. *Quarterly Reviews of Biophysics*, 36(2):147–227, 2003.

[152] Gregory V Barnett, Wei Qi, Samiul Amin, E Neil Lewis, Vladimir I Razinkov, Bruce A Kerwin, Yun Liu, and Christopher J Roberts. Structural changes and aggregation mechanisms for anti-streptavidin igg1 at elevated concentration. *The Journal of Physical Chemistry B*, 119(49):15150–15163, 2015.

[153] Karolina A Majorek, Przemyslaw J Porebski, Arjun Dayal, Matthew D Zimmerman, Kamila Jablonska, Alan J Stewart, Maksymilian Chruszcz, and Wladek Minor. Structural and immunologic characterization of bovine, horse, and rabbit serum albumins. *Molecular Immunology*, 52(3-4):174–182, 2012.

[154] Lok Kumar Shrestha, Rekha Goswami Shrestha, Kenji Aramaki, Genki Yoshikawa, and Katsuhiko Ariga. Demonstration of solvent-induced one-dimensional nonionic reverse micelle growth. *The Journal of Physical Chemistry Letters*, 4(15):2585–2590, 2013.

[155] KV Abrosimova, OV Shulenina, and SV Paston. FTIR study of secondary structure of bovine serum albumin and ovalbumin. In *Journal of Physics: Conference Series*, volume 769, page 012016. IOP Publishing, 2016.

[156] Dennis J Selkoe and John Hardy. The amyloid hypothesis of Alzheimer's disease at 25 years. *EMBO molecular medicine*, 8(6):595–608, 2016.

[157] Roma N Rambaran and Louise C Serpell. Amyloid fibrils: Abnormal protein assembly. *Prion*, 2(3):112–117, 2008. PMID: 19158505.

[158] Atul Mallik, Alex Drzezga, and Satoshi Minoshima. Clinical amyloid imaging. In *Seminars in Nuclear Medicine*, volume 47, pages 31–43. Elsevier, 2017.

[159] Claudia Kuntner, Adam L Kesner, Martin Bauer, Robert Kremslehner, Thomas Wanek, Markus Mandler, Rudolf Karch, Johann Stanek, Tanja Wolf, Markus Müller, et al. Limitations of small animal PET imaging with [18 F] FDDNP and FDG for quantitative studies in a transgenic mouse model of Alzheimer's disease. *Molecular Imaging and Biology*, 11(4):236–240, 2009.

[160] Mathieu D Santin, Thomas Debeir, S Lori Bridal, Thomas Rooney, and Marc Dhenain. Fast in vivo imaging of amyloid plaques using μ-MRI Gd-staining combined with ultrasound-induced blood–brain barrier opening. *NeuroImage*, 79:288–294, 2013.

[161] Manuel Fernández, J Keyriläinen, R Serimaa, M Torkkeli, ML Karjalainen-Lindsberg, M Tenhunen, W Thomlinson, V Urban, and P Suortti. Small-angle x-ray scattering studies of human breast tissue samples. *Physics in Medicine & Biology*, 47(4):577, 2002.

[162] M Bernhardt, JD Nicolas, M Eckermann, B Eltzner, F Rehfeldt, and T Salditt. Anisotropic x-ray scattering and orientation fields in cardiac tissue cells. *New Journal of Physics*, 19(1):013012, 2017.

[163] JH Kinney, JA Pople, GW Marshall, and SJ Marshall. Collagen orientation and crystallite size in human dentin: a small angle x-ray scattering study. *Calcified Tissue International*, 69(1), 2001.

[164] Ellen Wachtel and Stephen Weiner. Small-angle x-ray scattering study of dispersed crystals from bone and tendon. *Journal of Bone and Mineral Research*, 9(10):1651–1655, 1994.

[165] Eshan Dahal, Bahaa Ghammraoui, and Aldo Badano. Characterization of materials embedded in thick objects using spectral small-angle x-ray scattering. *Journal of Physics D: Applied Physics*, 2020.

[166] Eshan Dahal, Mina Choi, Nadia Alam, Ashwinkumar A Bhirde, Serge L Beaucage, and Aldo Badano. Structural evaluation of an amyloid fibril model using small-angle x-ray scattering. *Physical Biology*, 14(4):046001, 2017.

[167] Rebecca Gail Canter, Wen-Chin Huang, Heejin Choi, Jun Wang, Lauren Ashley Watson, Christine G Yao, Fatema Abdurrob, Stephanie M Bousleiman, Jennie Z Young, David A Bennett, et al. 3D mapping reveals network-specific amyloid progression and subcortical susceptibility in mice. *Communications Biology*, 2(1):1–12, 2019.

[168] Oskar Paris, Chenghao Li, Stefan Siegel, Gundolf Weseloh, Franziska Emmerling, Heinrich Riesemeier, Alexei Erko, and Peter Fratzl. A new experimental station for simultaneous x-ray microbeam scanning for small-and wide-angle scattering and fluorescence at BESSY II. *Journal of Applied Crystallography*, 40(s1):s466–s470, 2007.

[169] Johan Bergenholtz, Jeanette Ulama, and Malin Zackrisson Oskolkova. Analysis of small-angle x-ray scattering data in the presence of significant instrumental smearing. *Journal of Applied Crystallography*, 49(1):47–54, 2016.

[170] Eshan Dahal, Andreu Badal, Ahmed Zidan, Alaadin Alayoubi, Tomoe Hagio, Stephen Glick, Aldo Badano, and Bahaa Ghammraoui. Stable gelatin-based phantom materials with tunable x-ray attenuation properties and 3D printability for x-ray imaging. *Physics in Medicine & Biology*, 63(9):09NT01, 2018.

[171] Susan M Landau, Allison Fero, Suzanne L Baker, Robert Koeppe, Mark Mintun, Kewei Chen, Eric M Reiman, and William J Jagust. Measurement of longitudinal β-amyloid change with 18F-florbetapir PET and standardized uptake value ratios. *Journal of Nuclear Medicine*, 56(4):567–574, 2015.

[172] P Murali Doraiswamy, Reisa A Sperling, R Edward Coleman, Keith A Johnson, Eric M Reiman, Mat D Davis, Michael Grundman, Marwan N Sabbagh, Carl H Sadowsky, Adam S Fleisher, et al. Amyloid-β assessed by florbetapir F 18 PET and 18-month cognitive decline: a multicenter study. *Neurology*, 79(16):1636–1644, 2012.

[173] Bahaa Ghammraoui and Aldo Badano. Identification of amyloid plaques in the brain using an x-ray photon-counting strip detector. *Plos One*, 15(2):e0228720, 2020.

[174] Adriano Aguzzi and Tracy O'connor. Protein aggregation diseases: pathogenicity and therapeutic perspectives. *Nature Reviews Drug Discovery*, 9(3):237–248, 2010.

[175] Susan M Landau, Christopher Breault, Abhinay D Joshi, Michael Pontecorvo, Chester A Mathis, William J Jagust, and Mark A Mintun. Amyloid-β imaging with Pittsburgh compound B and florbetapir: comparing radiotracers and quantification methods. *Journal of Nuclear Medicine*, 54(1):70–77, 2013.

[176] Marios Georgiadis, Aileen Schroeter, Zirui Gao, Manuel Guizar-Sicairos, Dmitry S Novikov, Els Fieremans, and Markus Rudin. Retrieving neuronal

orientations using 3D scanning SAXS and comparison with diffusion MRI. *NeuroImage*, 204:116214, 2020.

[177] Eshan Dahal, Bahaa Ghammraoui, and Aldo Badano. Feasibility of a label-free x-ray method to estimate brain amyloid load in small animals. *Journal of Neuroscience Methods*, 2020.

[178] Holly Oakley, Sarah L Cole, Sreemathi Logan, Erika Maus, Pei Shao, Jeffery Craft, Angela Guillozet-Bongaarts, Masuo Ohno, John Disterhoft, Linda Van Eldik, et al. Intraneuronal β-amyloid aggregates, neurodegeneration, and neuron loss in transgenic mice with five familial Alzheimer's disease mutations: potential factors in amyloid plaque formation. *Journal of Neuroscience*, 26(40):10129–10140, 2006.

[179] Panchanan Maiti, Tia C Hall, Leela Paladugu, Nivya Kolli, Cameron Learman, Julien Rossignol, and Gary L Dunbar. A comparative study of dietary curcumin, nanocurcumin, and other classical amyloid-binding dyes for labeling and imaging of amyloid plaques in brain tissue of 5×-familial Alzheimer's disease mice. *Histochemistry and Cell Biology*, 146(5):609–625, 2016.

[180] Adam W Bero, Ping Yan, Jee Hoon Roh, John R Cirrito, Floy R Stewart, Marcus E Raichle, Jin-Moo Lee, and David M Holtzman. Neuronal activity regulates the regional vulnerability to amyloid-β deposition. *Nature Neuroscience*, 14(6):750, 2011.

[181] Arianna Casciati, Katalin Dobos, Francesca Antonelli, Anett Benedek, Stefan J Kempf, Montserrat Bellés, Andrea Balogh, Mirella Tanori, Luis Heredia, Michael J Atkinson, et al. Age-related effects of x-ray irradiation on mouse hippocampus. *Oncotarget*, 7(19):28040, 2016.

[182] Cynthia McCollough, Theresa Branham, Vince Herlihy, Mythreyi Bhargavan, Lavonne Robbins, Krista Bush, Michael McNitt-Gray, J Thomas Payne, Tom Ruckdeschel, Doug Pfeiffer, et al. Diagnostic reference levels from the ACR CT accreditation program. *Journal of the American College of Radiology*, 8(11):795–803, 2011.

[183] Eshan Dahal, Mina Choi, Bahaa Ghammraoui, and Aldo Badano. SAXS imaging of amyloid aggregates in humans without contrast agent. *Alzheimer's and Dementia*, 14(7, Supplement):834 – 835, 2018.

[184] David Eisenberg and Mathias Jucker. The amyloid state of proteins in human diseases. *Cell*, 148(6):1188–1203, 2012.

[185] Robert Tycko and Reed B Wickner. Molecular structures of amyloid and prion fibrils: consensus versus controversy. *Accounts of Chemical Research*, 46(7):1487–1496, 2013.

[186] Victoria E Johnson, William Stewart, and Douglas H Smith. Traumatic brain injury and amyloid-β pathology: a link to alzheimer's disease? *Nature Reviews Neuroscience*, 11(5):361–370, 2010.

[187] Tero Tapiola, Irina Alafuzoff, Sanna-Kaisa Herukka, Laura Parkkinen, Päivi Hartikainen, Hilkka Soininen, and Tuula Pirttilä. Cerebrospinal fluid β-amyloid 42 and tau proteins as biomarkers of Alzheimer-type pathologic changes in the brain. *Archives of Neurology*, 66(3):382–389, 2009.

[188] Jinny Claire Lee, Soo Jung Kim, Seungpyo Hong, and YoungSoo Kim. Diagnosis of Alzheimer's disease utilizing amyloid and tau as fluid biomarkers. *Experimental & Molecular Medicine*, 51(5):1–10, 2019.

[189] Niklas Mattsson-Carlgren, Emelie Andersson, Shorena Janelidze, Rik Ossenkoppele, Philip Insel, Olof Strandberg, Henrik Zetterberg, Howard J Rosen, Gil Rabinovici, Xiyun Chai, et al. Aβ deposition is associated with increases in soluble and phosphorylated tau that precede a positive Tau PET in Alzheimer's disease. *Science Advances*, 6(16):eaaz2387, 2020.

[190] Victor L Villemagne, Michelle T Fodero-Tavoletti, Colin L Masters, and Christopher C Rowe. Tau imaging: early progress and future directions. *The Lancet Neurology*, 14(1):114–124, 2015.

[191] Martin Von Bergen, Stefan Barghorn, Jacek Biernat, Eva-Maria Mandelkow, and Eckhard Mandelkow. Tau aggregation is driven by a transition from random coil to beta sheet structure. *Biochimica et Biophysica Acta (BBA)-Molecular Basis of Disease*, 1739(2-3):158–166, 2005.

[192] Salvatore Oddo, Antonella Caccamo, Jason D Shepherd, M Paul Murphy, Todd E Golde, Rakez Kayed, Raju Metherate, Mark P Mattson, Yama Akbari, and Frank M LaFerla. Triple-transgenic model of Alzheimer's disease with plaques and tangles: intracellular Aβ and synaptic dysfunction. *Neuron*, 39(3):409–421, 2003.